North Carolina Agricultural and Technical State University
Aggie Digital Collections and Scholarship

Dissertations | Electronic Theses and Dissertations

2013

Study Of N Incorporation In Insb On Gaas By Molecular Beam Epitaxy For Long Wavelength Infrared Devices

Nimai Chand Patra
North Carolina Agricultural and Technical State University

Follow this and additional works at: https://digital.library.ncat.edu/dissertations

Part of the Electromagnetics and Photonics Commons, and the Electronic Devices and Semiconductor Manufacturing Commons

Recommended Citation

Patra, Nimai Chand, "Study Of N Incorporation In Insb On Gaas By Molecular Beam Epitaxy For Long Wavelength Infrared Devices" (2013). *Dissertations*. 125.
https://digital.library.ncat.edu/dissertations/125

This Dissertation is brought to you for free and open access by the Electronic Theses and Dissertations at Aggie Digital Collections and Scholarship. It has been accepted for inclusion in Dissertations by an authorized administrator of Aggie Digital Collections and Scholarship. For more information, please contact iyanna@ncat.edu.

Study of N Incorporation in InSb on GaAs by Molecular Beam Epitaxy for Long Wavelength Infrared Devices

Nimai Chand Patra

North Carolina A&T State University

A dissertation submitted to the graduate faculty

in partial fulfillment of the requirements for the degree of

DOCTOR OF PHILOSOPHY

Department: Electrical and Computer Engineering

Major: Electrical Engineering

Major Professor: Dr. Shanthi Iyer

Greensboro, North Carolina

2013

School of Graduate Studies
North Carolina Agricultural and Technical State University
This is to certify that the Doctoral Dissertation of

Nimai Chand Patra

has met the dissertation requirements of
North Carolina Agricultural and Technical State University

Greensboro, North Carolina
2013

Approved by:

Dr. Shanthi Iyer Major Professor	Dr. Ward Collis Committee Member
Dr. Clinton Lee Committee Member	Dr. Jung H Kim Committee Member
Dr. John Kelly Department Chair	Dr. John Kelly Committee Member

Dr. Sanjiv Sarin
Dean, The Graduate School

© Copyright by

Nimai Chand Patra

2013

Biographical Sketch

Nimai Chand Patra was born in Orissa, India. He received his Master of Science degree in Physics with electronics specialization from Sri Sathya Sai Institute of Higher Learning in 2008. He is passionate about working in the ever challenging area of novel semiconductor materials and devices.

Dedication

To my constant inspiration and mentor, Bhagawan Sri Sathya Sai Baba.

Acknowledgements

First and foremost, I would like to express my sincere gratitude to my research advisor Professor Shanthi Iyer for her support and guidance throughout this research work. Especially her patience, tolerance and considerate demeanor towards my mistakes have allowed me room for improvement. She definitely taught me the attitude of 'never give up' and 'work hard' which fueled me with zeal to stay focused in this project. Her knowledge, expertise, and wisdom in subjects such as molecular beam epitaxy, semiconductor materials, characterization techniques and effective research methodology helped me to grow intellectually as a researcher and to complete this work successfully.

I would also like to thank the members of my dissertation committee, Dr. Ward Collis, Dr. Clinton Lee, Dr. John Kelly and Dr. Jung Kim from the Department of Electrical and Computer Engineering as well as my research observer Dr. Shyam Aravamudhan from the Department of Nanoengineering at North Carolina A&T State University. Their feedback and suggestions were valuable in further exploration and gave a proper direction to my research.

It was an honor and a pleasure to work with former and current research associates of Dr. Iyer's Lab, whom I would like to thank individually. Dr. Jia Li for teaching me various instruments' hands on skills and Dr. Sudhakar Bharatan for helping me learn the nuances of MBE lab and various other semiconductor characterization techniques. All the long distance driving, late night (along with many night outs) working in the MBE lab and brain storming sessions with my running buddy Adam Bowen definitely paid off, as I grew up as a person in this process. Special thanks to other stalwarts of the research group: Dr. Tanina Bradley, Robert Alston, Shereen Farhana, Jon Poe and Sai Krishna Ojha for their constant support throughout this

research. All the intellectual/moral discussions which happened 'unofficially' in the lab will definitely be a long cherished memory as they added a lot of value to my research work.

I am greatly indebted to my father, mother and brother for their constant help and unlimited support even though they were physically far from me. I would like to thank all the individuals and families of our community in Greensboro who have now become part of my extended family. I heartily express my gratitude for their constant help, timely support and unconditional love which made me feel at home even though I am away from home.

I would fail in my duty of appreciating people if I do not acknowledge all those researchers and techies who worked hard in developing various materials concepts and instrumentations which helped carry out research work without re-inventing the wheel. Although I have referenced many such works in this dissertation, still there are many others I would like to acknowledge who have helped me understand the fundamental concepts and some Dos and Don'ts. I would like to extend my gratitude to all the giants behind developing some of the software tools like Microsoft Office, EndNote and Origin for making my life easy for research documentation/ presentation, bibliography management and plotting data for analysis.

A special mention goes to Dr. Mark Walters and the staff of Shared Materials Instrumentation Facility (SMIF) at Duke University for all the technical training and assistance for micro-Raman, x-ray photoelectron spectroscopy (XPS), triple axis high-resolution x-ray diffraction (HRXRD), reciprocal space mapping (RSM) and rapid thermal annealing (RTA). Other characterizations such as secondary ion-mass spectroscopy (SIMS) and nuclear reaction analysis (NRA) for Rutherford backscattering spectroscopy (RBS) performed by Evans Analytical Group was very helpful to determine nitrogen incorporation, a critical part of the research. Sincere thanks to Dr. Lew Reynolds Jr. from the department of Material Science and

Engineering at North Carolina State University for allowing us to use the Fourier transform infrared (FTIR) spectrometer at his lab, to study the optical absorption property which happened to be a bottle neck in the research initially. In order to do that, we drove around 180 miles every day just to get the absorption spectra! The instrumentation facility at Joint School of Nanoscience and Nanoengineering (JSNN) came to rescue when we were given an unlimited access to use the FTIR spectrometer in the analytical lab. A heartfelt gratitude to Dr. James Ryan, Founding Dean of JSNN and Dr. Marinella Sandros for providing a timely support which not only saved gasoline but also time and energy to drive for getting the must needed absorption data. Further, a sense of appreciation goes to all the technical people from various companies who shared their wisdom over several teleconference sessions during time of need.

In addition, I would like to thank the Electrical and Computer Engineering department for giving me the opportunity to serve as a teaching assistant in the department which not only supported my living expenses but also made teaching/learning a memorable experience both for myself and other students. Finally, I would like to acknowledge the financial support of the U.S. Army Research Office (Grant # W911NF-07-1-0577) under the technical monitor Michael Gerhold.

Table of Contents

List of Figures xii

List of Tables xvii

List of Symbols xviii

Abstract 2

CHAPTER 1 Introduction 3

1.1 A Brief History of Infrared Technology 6

1.2 Motivation 9

1.3 Challenges 10

1.4 Objective 12

1.5 Outline of the Dissertation 14

CHAPTER 2 Literature Review 17

2.1 Why InSb 17

2.2 Growth of InSb on GaAs 18

2.3 Bandgap Reduction in III-V-N Materials 21

2.4 Band Anticrossing in InSbN 21

2.5 Growth and Characterization of $InSb_{1-x}N_x$ 22

2.6 Study of Defects in InSbN 24

2.7 Effect of Annealing on InSbN 25

2.8 Bandgap Determination of InSbN 26

2.9 Devices Based on InSbN 28

2.10 Conclusion 30

CHAPTER 3 MBE Growth and Characterization Techniques 31

3.1 MBE Overview 31

3.2 MBE Elemental Sources and Components 31

3.3 Growth of InSb on GaAs 33

3.4 Growth of InSbN on GaAs 34

3.5 Post Growth Processing: Annealing 35

3.6 Characterization Techniques 36

3.6.1 RHEED. 36

3.6.2 HRXRD. 37

3.6.3 RSM. 39

3.6.4 Micro-Raman spectroscopy. 40

3.6.5 Absorption spectroscopy. 41

3.6.6 Hall measurements. 47

3.6.7 AFM. 47

3.6.8 XPS. 47

3.6.9 SIMS. 50

3.6.10 NRA. 51

3.7 Conclusion 53

CHAPTER 4 Growth and Characterization of InSb Epilayers Grown on GaAs (001) Substrates..54

4.1 Introduction 54

4.2 Sb/In BEP Ratio and Growth Temperature Optimization 55

4.3 Results and Discussion 57

4.4 Conclusion 62

CHAPTER 5 Growth and Characterization of InSbN Heterostructures on GaAs (001) Substrates....63

5.1 Introduction....63

5.2 Experimental Details....63

5.3 Results and Discussion....64

5.3.1 N BEP variation....65

5.3.2 Growth temperature variation....70

5.4 Conclusion....74

CHAPTER 6 Study of N Incorporation in InSbN with Variation in Growth Temperature....75

6.1 Introduction....75

6.2 Experimental Details....75

6.3 Results....75

6.3.1 RHEED....75

6.3.2 HRXRD....76

6.3.3 Micro-Raman spectroscopy....77

6.3.4 XPS....78

6.3.5 AFM....80

6.3.6 Hall measurement....80

6.3.7 FTIR....82

6.4 Discussion....82

6.5 Conclusion....88

CHAPTER 7 Effect of Annealing on InSbN....90

7.1 Introduction 90

7.2 *Ex-situ* Annealing 91

7.3 *In-situ* Annealing 93

7.4 Comparative Study of *Ex-situ* and *In-situ* Annealing 96

7.4.1 HRXRD. 96

7.4.2 Micro-Raman spectroscopy. 99

7.4.3 Hall measurement. 101

7.4.4 FTIR. 103

7.5 Conclusion 105

CHAPTER 8 Study of Defects in InSbN Heterostructures 106

8.1 Introduction 106

8.2 Experimental Details 106

8.3 Results 107

8.4 Discussion 117

8.5 Conclusion 120

CHAPTER 9 Conclusion 121

References 125

Appendix A 144

List of Figures

Figure 1.1. Atmospheric transmission window along with corresponding applications.[1] 4

Figure 1.2. Transmission of the atmosphere for a 6,000 feet horizontal path at sea level.[2]............5

Figure 1.3. Block diagram of a typical infrared device application..6

Figure 1.4. Challenges involved in the growth of InSbN epilayer. 10

Figure 2.1. Diagram showing various RHEED patterns observed on (001) InSb surface.[53] 19

Figure 2.2. (a) the calculated band structure as a function of nitrogen composition, (b) the band gap variation over the mid to long wavelength IR range for $InSb_{1-x}N_x$.[21] 21

Figure 3.1. The EPI 930 MBE system along with electronic control rack in the clean room facility...32

Figure 3.2. A screenshot of the (004) HRXRD simulation of InSbN/InSb/GaAs heterostructure performed by RADS mercury software. 38

Figure 3.3. A screenshot of the individual layers and corresponding parameters used in the software for the simulated data in Figure 3.2. 39

Figure 3.4. FTIR RT transmission spectrum of two InSbN heterostructures..............................42

Figure 3.5. RT FTIR transmission spectra of InSb heterostructure grown on single sided polished GaAs substrate. 43

Figure 3.6. RT FTIR transmission spectra of InSb heterostructure grown on double sided polished GaAs substrate. 44

Figure 3.7. Estimation of optical absorption edge from FTIR absorption spectra. 46

Figure 3.8. XPS survey scan spectra performed on the surface of InSb heterostructure. 48

Figure 3.9. XPS N 1s spectra of InSbN sample pre and post sputter cleaning............................50

Figure 3.10. SIMS depth profile of 0.4 µm InSbN/ 1.4 µm InSb/GaAs heterostructure. 51

Figure 3.11. NRA Rutherford backscattered spectra of InSbN heterostructure grown at 290 °C. 53

Figure 4.1. Sequence of RHEED patterns observed during growth of InSb on GaAs buffer along (110) azimuth. 55

Figure 4.2. RHEED patterns on epitaxial InSb grown on (001) surface of GaAs.[30] 56

Figure 4.3. (004) HRXRD scan of 0.6 µm InSb epilayer grown on GaAs substrate. 57

Figure 4.4. InSb grown on GaAs Sb/In BEP ratio vs HRXRD FWHM. 58

Figure 4.5. RT micro-Raman spectra comparison of 1.4 µm InSb grown at different growth conditions. 59

Figure 4.6. SIMS depth profile of 0.6 µm InSb/GaAs heterostructure. 60

Figure 4.7. The Nomarski optical microscope image of InSb grown at 380 °C on GaAs substrate under Sb:In BEP ratio of (a) 1.5 and (b) 3.3. 61

Figure 4.8. AFM surface image of InSb grown at T_C with best surface roughness of 0.28 nm. 62

Figure 5.1. RHEED patterns observed during the growth of InSbN epilayers. 64

Figure 5.2. A combination of spots and streaks in the RHEED pattern observed during InSbN growth. 65

Figure 5.3. HRXRD (004) scan of InSbN epilayers grown under different N BEP at Ts 380 °C. 66

Figure 5.4. RT micro-Raman spectra of InSbN heterostructures grown under different N BEP at Ts 380 °C. 67

Figure 5.5. AFM images of InSbN epilayers grown under different growth conditions. 68

Figure 5.6. RT FTIR absorption spectra of InSbN epilayers grown at various N plasma BEP, compared with the reference InSb. 69

Figure 5.7. (004) HRXRD scan of InSbN epilayers grown at various temperatures along with the reference InSb sample. 71

Figure 5.8. RT micro-Raman spectra of InSbN heterostructures grown at different temperatures. 71

Figure 5.9. RT FTIR transmission spectra of the InSbN epilyaers grown at different Ts. 73

Figure 5.10. RT absorption spectra of InSbN epilayers grown at different Ts with InSb reference. 73

Figure 6.1. RHEED patterns showing a c(1 x 3) reconstruction during the growth of InSbN epilayers.[30] 76

Figure 6.2. HRXRD (004) scan of InSbN epilayers grown at different Ts with InSb reference.[30] 76

Figure 6.3. (a) Comparison of RT micro-Raman spectra of the InSb reference epilayer with InSbN alloys grown at different temperatures, (b) Lorentzian fit for Raman spectra in first order TO and LO phonon ranges of all the epilayers represented in Figure (a).[30] 78

Figure 6.4. N 1s spectrum of InSbN epilayers grown at different temperatures. 79

Figure 6.5. AFM images of InSbN epilayers grown at (a) 290, (b) 330 and (c) 380 °C.[30] 80

Figure 6.6. RT and 77 K Hall n and μ measured at 5.8 kG for InSbN epilayers grown at different growth temperatures.[30] 80

Figure 6.7. RT Hall carrier concentration (n) and mobilities (μ) measured at 0.5 and 5.8 kG magnetic.[30] 81

Figure 6.8. α vs energy plots for InSbN epilayers grown at different temperatures compared with InSb reference.[30] 82

Figure 7.1. HRXRD spectra of InSbN N2 before and after ex-situ annealing. 92

Figure 7.2. RT absorption spectra of InSbN N2 before and after ex-situ annealing compared with InSb reference heterostructure. 92

Figure 7.3. RT optical absorption edge for InSbN heterostructure annealed at 450 °C. 93

Figure 7.4. (004) HRXRD scan of in-situ annealed InSbN heterostructures annealed at 430 ºC. 94

Figure 7.5. RT absorption spectra of in-situ annealed InSbN heterostructures. 95

Figure 7.6. Plot of (004) HRXRD scan for the InSb reference, as-grown, ex-situ and in-situ annealed InSbN epilayers.[134] 96

Figure 7.7. SIMS depth profile of as-grown, ex-situ and in-situ annealed InSbN heterostructures grown at 290 °C. 98

Figure 7.8. (a) The RT micro-Raman spectra of as-grown, ex-situ and in-situ annealed InSbN epilayers compared with the InSb reference and (b) Lorentzian fit for the RT micro-Raman spectra in the 1st order InSb TO and LO for the spectra illustrated in (a). [134] 99

Figure 7.9. The RT absorption coefficient (α) vs energy (eV) plot for as-grown, ex-situ and in-situ annealed InSbN epilayers along with the InSb reference. The inset shows the first order derivative of α vs eV for the ex-situ annealed InSbN epilayer.[134] 103

Figure 8.1. (004) HRXRD of four different InSbN heterostructures along with InSb reference. 107

Figure 8.2. (115) HRXRD plot of four different InSbN heterostructures. 108

Figure 8.3. (115) reciprocal space map of heterostructure S1 along with GaAs peak. 110

Figure 8.4. (a) (004) and (b) (115) reciprocal space maps of the heterostructure S1. 111

Figure 8.5. (115) reciprocal space map of the heterostructure S2. 112

Figure 8.6. (a) (004) and (b) (115) reciprocal space maps of the heterostructure S3. 112

Figure 8.7. (a) (004) and (b) (115) reciprocal space maps of the heterostructure S4. 113

Figure 8.8. (115) reciprocal space map of the heterostructure S2 after ex-situ anneal at 450 °C...114

Figure 8.9. (a) (004) and (b) (115) reciprocal space maps of the heterostructure S4 after in-situ anneal at 430 ºC. 115

Figure 8.10. (004) reciprocal space map of the heterostructure S4 after ex-situ anneal at 430 ºC...115

Figure 8.11. The comparison of RT n and μ for different InSbN heterostructures measured at low and high magnetic fields. 116

Figure 9.1. InSbN heterostructure for dual color (MWIR and LWIR) applications..................124

List of Tables

Table 2.1 Table to summarize the growth and E_g reported for InSbN by various research groups 29

Table 3.1 NRA measured channeling parameters 53

Table 5.1 Comparison of AFM measured R_{rms} and Hall data of InSbN epilayers grown at different N BEP 68

Table 5.2 Comparison of AFM measured surface roughness and Hall data of InSbN epilayers grown at different growth temperatures. 72

Table 6.1 Comparison of N_{Sb} (%) from HRXRD, N 1s XPS peak compositions along with I_{TO}/I_{LO} ratio from micro-Raman and electrical properties measured at 0.5 kG of InSbN epilayers grown at different temperatures. 77

Table 7.1 SIMS N %, Raman I_{LO}/I_{TO}, RT and 77 K carrier concentration (n) and mobility (μ) data for the *as-grown*, *ex-situ* and *in-situ* annealed InSbN epilayers. 100

Table 8.1 (004) and (115) HRXRD FWHM of different InSbN heterostructures. 109

List of Symbols

α	Absorption coefficient
λ	Wavelength
μ	Mobility
2D	Two dimensional
3D	Three dimensional
AFM	Atomic Force Microscopy
at. %	Atomic percent
As	Arsenic
B	Billion
BAC	Band Anticrossing
BE	Binding Energy
BEP	Beam Equivalent Pressure
CB	Conduction band
CBM	Conduction band minimum
cps	Counts per second
D	Dislocation Density
E_C	Conduction band energy
E_g	Band gap energy
E_V	Valence band energy
ECR	Electron cyclotron resonance
et al	Et al "and others"

FTIR	Fourier Transform Infrared
FWHM	Full width half maxima
Ga	Gallium
GaAs	Gallium Arsenide
HREELS	High-resolution electron loss spectroscopy
HRXRD	High Resolution X-Ray Diffraction
In	Indium
InSb	Indium antimonide
InSbN	Indium antimonide nitride
I_{LO}	Intensity of LO phonon mode
I_{TO}	Intensity of TO phonon mode
IR	Infrared
LED	Light Emitting Diode
LO	Longitudinal Optical
LWIR	Long wavelength infrared
MBE	Molecular Beam Epitaxy
MOCVD	Metalorganic Chemical Vapor Deposition
MOVPE	Metalorganic Vapor Phase Epitaxy
MWIR	Mid wavelength infrared
N	Nitrogen
n	Carrier concentration
NRA	Nuclear Reaction Analysis
N_{Sb}	Nitrogen atom substituted Sb at Sb site in InSb structure

PL	Photoluminescence
QW	Quantum Well
QWIP	Quantum well infrared photodetector
RHEED	Reflection High Energy Electron Diffraction
RBS	Rutherford Back Scattering
rf	Radio frequency
RGA	Residual gas analyzer
RLP	Reciprocal Lattice Point
Rms	Root mean square
R_{rms}	Surface roughness RMS
RSM	Reciprocal Space Map
RTA	Rapid Thermal Annealing
Sb	Antimony
SLS	Strained layer superlattice
SIMS	Secondary Ion Mass Spectroscopy
SL	Superlattice
T (%)	Transmission (%)
Tc	Transition temperature
TO	Transverse Optical
Ts	Substrate temperature
UHV	Ultra high vacuum
VBM	Valence Band Maximum
VOx	Vanadium Oxide

Abstract

The distinguishing features of dilute nitride III-V semiconductors lie in the large simultaneous reduction in the band gap and lattice parameter when N is incorporated in small amounts in an otherwise wide band gap III-V material. In particular, N incorporation in InSb is attracting great attention due to its potential applications in the long wavelength infrared (LWIR) applications. However, the relatively small atomic size of N with respect to Sb makes the growth of good quality InSbN layers challenging with effective N incorporation. In this dissertation we present a correlation of the molecular beam epitaxial growth parameters on the type of N-bonding in the InSbN epilayers. Lower growth temperatures of ~290 °C were observed to favor formation of more substitutional N (In−N) and less interstitial N (Sb−N, N−N and In−N−Sb) in the InSbN epilayers. The types of N-bonding were observed to have dominant effect on the structural, vibrational, electrical and optical properties of these dilute nitride epilayers grown on GaAs substrates. *As-grown* epilayers with high N incorporation of 2.6 % were observed to exhibit a blue shift in the absorption edge to 0.132 eV due to Moss-Burstein effect. Both *ex-situ* and *in-situ* annealing at 430 °C improved the quality of the layers as attested to by the micro-Raman spectra, reduced the carrier concentration to ~10^{16} cm^{-3}, increased the mobility (μ) to ~13,000 cm^2/V-s and red shift the absorption edge to ~10 µm at room temperature (RT). Amongst the heterostructures examined, consisting of different combination of thickness of InSb and InSbN layers, the growth of a relatively thick (~1.4 µm) InSb buffer layer was found to prevent the propagation of rotational and threading dislocations into the subsequent InSbN epilayers. Thus, high RT μ exceeding 40,000 cm^2/Vs and an optical absorption edge at ~12 µm in the LWIR range have been achieved for 450 °C *ex-situ* annealed 0.4 µm InSbN/ 1.4 µm InSb/ GaAs heterostructure.

CHAPTER 1

Introduction

The optical vision range of human eye limits only to a small wavelength window in the entire electromagnetic spectrum. Whereas, there are many other species on this planet believed to have the ability to view beyond this range of human optical vision. Today, with the progress in various types of electromagnetic detection technologies mainly in the area of semiconductors, we are able to leverage the entire electromagnetic spectrum for various applications. The potential of applications and opportunity for development of technologies around the electromagnetic spectrum is limitless. Figure 1.1 depicts the atmospheric transmission window for the entire electromagnetic spectrum and corresponding applications. Only a certain range of wavelengths can be used for applications such as atmospheric wireless communications, depending on our atmosphere being transparent only to those wavelengths in the entire spectrum. The transparency in the visible range of spectrum has been taken an advantage of design and development of various lighting technology not only for day to day use but also for various targeted applications. These applications include highly sophisticated medical surgeries with the help of lasers to simple and colorful lights to decorate a Christmas tree. Further, these technologies have shown a path for accomplishing innumerable tasks to make our life comfortable with various commercially successful products starting from a household appliance to a bar code scanning system to a security system and so on.

Another such highly potential spectrum of wavelengths, where the atmospheric losses are minimal, is infrared region. Although this infrared region remains invisible to the human eye, this portion of the electromagnetic spectrum has caught attention of many from centuries especially for military and extraterrestrial applications because of its unique properties.

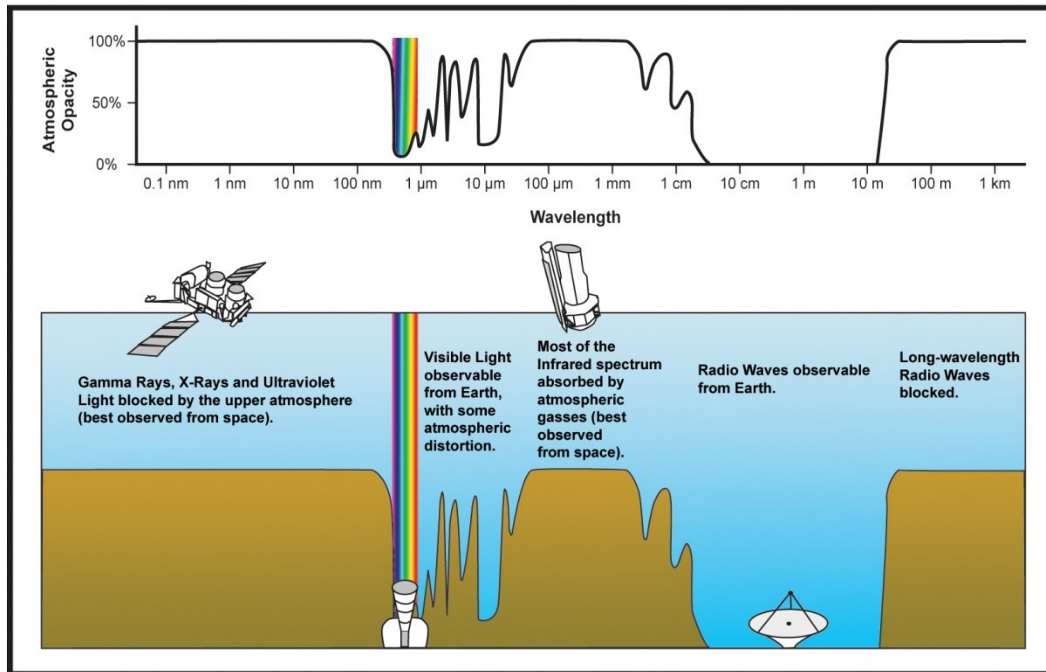

Figure 1.1. Atmospheric transmission window along with corresponding applications.[1]

Based on the transmission property of the atmosphere in this infrared (IR) spectrum, the IR region has been further divided into different regions. They are, (a) near-infrared (NIR: 0.75−1.4 µm), (b) short-wavelength infrared (SWIR: 1.4−3 µm), (c) mid-wavelength infrared (MWIR: 3−8 µm), (d) long-wavelength infrared (LWIR: 8−14 µm), (e) far infrared (FIR: 14−1000 µm). Figure 1.2 shows the atmospheric transmission property of a selective infrared range (0-15 µm) and corresponding absorbing molecules. Various types of application prototypes such as proximity sensors, gas detectors, fire alarms, wireless remote control systems can be designed within a certain wavelength range depending on the transmission/absorption behavior of the selected wavelength range in the atmosphere. The wavelength range from 8 to 14 µm is the longest wavelength range, known as long-wavelength infrared range (LWIR), exhibits high atmospheric transparency in comparison to other wavelength window in this entire IR spectral regime. This region has been extensively used for applications such as atmospheric wireless communications and has been used as the basis of research and development for an

application which targets for a solution to the problem in real time operation for various wireless technologies. This infrared window is also found to be a very useful window of operation for many other applications, such as night vision, surveillance, and non-invasive medical imaging.

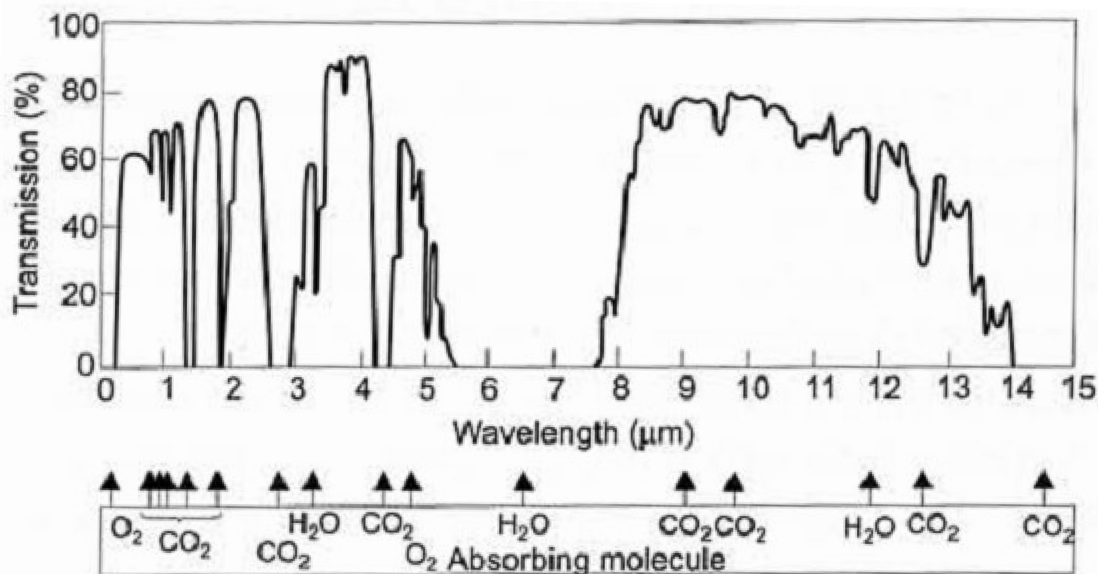

Figure 1.2. Transmission of the atmosphere for a 6,000 feet horizontal path at sea level.[2]

Most of these applications in LWIR can be summarized in a simple block diagram as shown in Figure 1.3. Typically these involve three important basic components, a source of radiation which can be called as transmitter/emitter, the medium of transmission and a receiver/detector. For example, in case of a communication system an electromagnetic spectrum can be generated using a semiconducting device and transmitted by a transmitter. The medium of transmission can either be an optical fiber or a copper wire or as simple as our atmosphere. Once the signal reaches the destination, the information can be received using a receiver which can also be a semiconducting detector. Similarly, this methodology can be applied to imaging. In this case, the object to be imaged can be considered as an emitter/ transmitter, transmitting radiations (signal) through atmosphere, which can be detected/ captured using a charge coupled device or a photoconductive device as an imaging element.

Figure 1.3. Block diagram of a typical infrared device application.

In a commercially available detector, every imaging element (also known as a pixel) is connected to a two-terminal readout integrated circuit. Every photon absorbed by the pixel generates an electronic signal which can be detected, recorded and stored as information. Various material properties of the pixel/ imaging element such as, band gap, optical absorption index, defects, compositional stability, play an important role in this entire process of signal detection. Hence, research and development of a suitable material is important to improve the performance with concurrent reduction in the level of complexity to make it cost effective.

1.1 A Brief History of Infrared Technology

The detection of infrared goes way back in 1800 when Frederick William Herschel discovered the temperature of solar spectrum slightly beyond red was higher than the visible light.[3] Initially, the detection of infrared was developed based on thermal detection principles such as thermometers, thermocouples and bolometers. Although, these responded to the entire infrared range they suffered low sensitivity and high response time. Later in 1920s, another kind of infrared detectors were developed based on the principle of photon detection after the discovery of photoconductivity and photovoltaic effects.[4] The period between World Wars I and II marked the development of photon detectors and image converters in a highly secretive manner as it enabled military operations to see enemy in dark.[4] This was the beginning of an aggressive material research study for high infrared optical absorption and fast detector response. This led to the emergence of various novel materials like Tl_2S, PbS, PbSe, Ge:X, InSb, HgCdTe, PbSnTe, Si:X, PtSi, InGaAs for the IR applications. However, these materials needed to be

cooled during the operation for a high signal to noise ratio unlike thermal detectors. In early 1960s, some of the narrow bandgap materials attracted more attention due to their high optical absorption coefficient, high electron mobility and low thermal generation rate along with the compatibility to bandgap engineering. Eventually, mercury cadmium telluride (MCT) HgCdTe, emerged as the most attractive material for infrared detection due to its bandgap energy tunability[5] in the entire infrared wavelength range. The recent advancement in the photolithography has shifted the focus towards integration of maximum detectors (pixels) in a readout integrated circuit (ROIC) leading to an increased interest towards focal plan array (FPA) capability of these infrared detector materials. Rogalski[4] has reported a detailed history of all the infrared technology and its development with progress of time and has forecasted MCT to lead the market for the next 10-15 years, when it comes to infrared detection. In the category of IR FPAs, currently MCT with 4096x4096 pixels fabricated by Teledyne Imaging Sensors[4] holds the record of the highest number of detection elements with pixel size 10x10 (µm) each. However, MCT suffers from material degradation at high temperature hence limited to low temperature operations and requires extra cooling system integrated to it for an efficient operation.

Among the category of uncooled IR detectors, FPAs of 2048x1536 vanadium oxide (VO_x) microbolometers with 17µm pixel pitch fabricated by Raytheon marked as the highest number of pixels in the array format detectors. Currently, these microbolometers are produced in larger volumes than all other IR array technologies combined, due to their drastic cost drop (~15% per year). In terms of the economic impact, it is expected to be used in commercial applications namely, surveillance, automotive, thermography and military applications such as, weapon sight, portable goggles, and vehicle vision enhancement with an estimated $3.4 B market by 2014.[4] Several other reviews by Razeghi et al[2] and Rogalski et al[4-10] clearly indicate this

multi-decade research focused on various other challenges involved in the development of these infrared technologies. Although, intrinsic semiconductors such as $Hg_{1-x}Cd_xTe$ and $Pb_{1-x}Sn_xTe$ have wide applications in which the energy gap can be controlled by varying x, these low band gap materials are characterized by weak bonding and low melting points, and are more difficult to grow and process than large band gap semiconductors such as GaAs.[11] Further, MCTs device performance is limited due to high Auger recombination rates, compositional non-uniformity in addition to the metallurgical challenges during growth and material instability at higher temperatures cited above.[5, 12] Hence, to overcome these challenges various III-V alloys, namely GaAsSb,[13] GaAsSbN,[14] GaSbN,[15] InGaAsSb,[16, 17] InGaAsSbN,[18] InAsSb,[19] InAsSbN,[20] InSbN,[21] and related heterostructures such as, strained layer superlattice (SLS),[22] quantum well infrared photodetectors (QWIP),[23] quantum dot photodetectors (QDIP),[23, 24] and dot in the well (DWELL)[25] device detectors are actively being researched in the last couple of decades. The current progress in the research and development of infrared detectors[4] indicate the focus of research and development is not only for the identification of suitable materials with improved quality for infrared detection at higher temperatures but also for an increased focal plane array functionality.

Amongst all these alloys and complex structures, InSb based photovoltaic FPAs fabricated on GaAs and Si substrates is based on a simple III-V binary alloy, which is reported[11] to exhibit excellent capabilities in MWIR range with applications including IR thermal imaging, environmental gas monitoring, and free space communications. Based on the success of InSb based photoconductive and photovoltaic IR detectors, the focus of research extended onto the other alloys with InSb as host material to extend the optical absorption cutoff into higher wavelength range. Alloys of $InAs_xSb_{1-x}$ observed to have absorption cutoff wavelength up to 14

μm operated at near RT (200-300 K).[26] Another potential material in the LWIR range $In_{1-x}Tl_xSb$ have been also demonstrated to exhibit RT cut off wavelength of about 11 μm.[27] Further, recently incorporation of Bi and N into InSb has been shown/ predicted to result in rapid bandgap reduction of 36 meV/ % Bi[2, 11] and 100 meV/ % N[21], respectively. These are other prospective material for LWIR detection. $InSb_{1-x}N_x$ alloys have been the material of interest for LWIR applications more than a decade now. A maximum photodetection limit up to 10 μm at 77 K was reported for the *in-situ* annealed InSbN heterostructures.[28] Hence, there is a lot of potential and further space for optimization in the development of InSbN material system for LWIR applications.

1.2 Motivation

Devices operating in the LWIR region of the electromagnetic spectrum has always been of great importance, due to its diverse applications, such as surveillance within the atmosphere, medical imaging, imaging through smoke and dust, infrared spectroscopy, wireless communication and detection of certain chemicals and gasses (Ozone, O_3) with unique absorption signatures in this range. Although, currently MCT is the mature technology in this wavelength range, it suffers from material instability and non-uniformity problems over large areas due to high Hg vapor pressure during the material growth. Additionally there are many other challenges with this material as discussed earlier. Hence, there has been a lot of interest in the use of heteroepitaxially grown Sb-based alloys, its strained layer superlattices and GaAs-based quantum wells as an alternative to MCT. Amongst all the other material systems discussed above, Sb based superlattice and type II superlattice (T2SL) devices[29] are believed to replace MCT for LWIR range operations with better performance, lower dark current and a high material robustness.[8, 9] Although theoretically T2SL is predicted to exhibit lower dark current, recent

progress indicates the need for complex barrier schemes to reduce the dark current.[29] Further, only certain devices like MCT photodiodes, QWIP, QDIPs has been used for fabricating devices with multicolor/ multispectral capability in MWIR and LWIR range, which provide an advantage of capturing more information in one image.[4, 25] InSbN[28, 30-32] appears to be another promising material due to its ability to control the band gap bowing by varying N incorporation, which in conjunction with InSb allows the fabrication of highly tunable devices suitable for dual color (both MWIR and LWIR range) photodetection.

1.3 Challenges

Although a small incorporation of N in InSb leads to giant band gap reduction, the N incorporation poses a challenge due to various following reasons. Firstly, the large disparity in the atomic size of the N and Sb leads to large miscibility gap and N incorporation beyond a few percent becomes a problem. Figure 1.4 shows schematically the associated challenges although, the atomic size of the individual atoms are not in appropriate scale. The smaller atomic size of N as compared to Sb atoms lend N into the interstitial sites rather than the substitutional site.

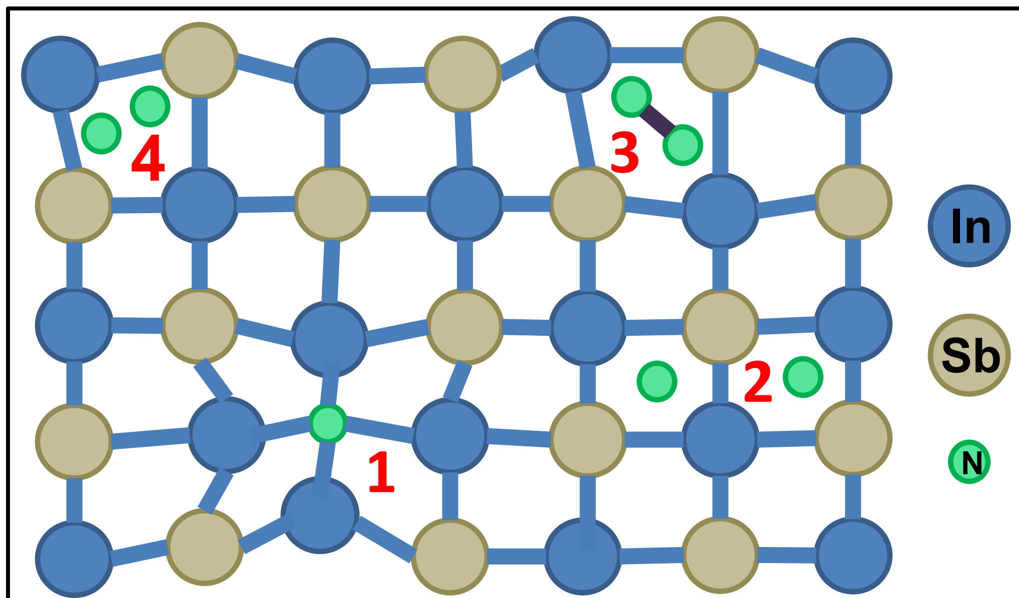

Figure 1.4. Challenges involved in the growth of InSbN epilayer.

In Figure 1.4 it can be seen that N atoms and even N_2 molecules (identified by numerals 2, 3 and 4) can interstitially fit inside the lattice. These interstitial atoms tend to distort the lattice structure in addition to the distortion created by the substitutional N atom (N atoms sitting in Sb site: N_{Sb}; marked by number 1 in Figure 1.4). The presence of N in the interstitial site results in high background n due to the donor nature of N atoms. Further, with increase in N incorporation in the substitutional sites (N_{Sb}), the crystal lattice ordering in the epilayers reduce due to the difference in bond lengths of In−N and In−Sb (as shown in Figure 1.4 at number 1). Hence, with increasing N incorporation the crystalline quality of the InSbN epilayers deteriorates and one has to trade-off between these two to arrive at the optimized characteristics.

Second, the use of InSb substrate for the growth of these InSbN layers has several drawbacks and limitations. The InSb substrates are limited in size because the quality of the substrate becomes inferior with the increase in the wafer diameter. Further, InSb substrates are expensive, non-semi-insulating (normally n-type), and are of lower quality than GaAs or Si. In order to conduct optical and electrical studies of the grown InSbN epilayers, semi-insulating substrate materials are required.

InSb being n-type in nature, for device operations in particular for FPAs, thinning of the InSb substrates to ~10 μm is required in order to minimize the absorption in the substrate. Hence semi-insulating GaAs (001) is more appropriate and was chosen for the substrate material in this study. However, the high lattice mismatch of ~14.6 % between GaAs and InSb provides complexity due to the presence of dislocations in the resulting hetero-junction, causing degradation in the InSbN layers grown subsequently. Based on all the above discussed challenges, various objectives and methodologies to overcome those obstacles were framed for this research work and are detailed in the next section.

1.4 Objective

The overall objective of the research is to develop high quality InSbN epilayers on GaAs substrate with N incorporation sufficient enough for photodetection in the entire LWIR (8 to 12 μm) range. In order to accomplish this, the challenges discussed above were addressed by the growth of high quality InSb buffer layer, study of N incorporation, correlation with N-bonding, reduction of *n* and overall heterostructure optimization with reduced defects.

The above specific objectives of the research and the approach adapted are detailed below:

► Establishment of the growth of high quality InSb buffer layer: This was accomplished by developing simple, reproducible and less defective InSb layer growth process on GaAs substrate by optimizing the MBE growth scheme. The growth parameters, such as Sb/In BEP ratio, growth temperature and InSb epilayer thickness, were varied one at a time. The choice of these growth parameters were based on a detailed literature study.

► Optimization of MBE growth parameters for effective N incorporation: The effect of various MBE growth parameters, such as N BEP, N plasma power, Sb/In BEP ratio and growth temperature, were studied independently for a good quality InSbN epilayer growth with increased N incorporation. The MBE grown InSbN epilayers were then characterized and an optimized growth scheme was established after their systematic correlation. Thus the effect of each of these parameters on the epilayer was identified individually.

► N-bonding study: A study in the variation of N bonding composition in conjunction with varying growth parameter and material property was carried out. The influence of various types of N bonding on the crystalline quality of the material was established by correlating different N- bonding with disorder observed in the InSbN epilayers with varying growth

temperature. The growth temperature is an important parameter which affects the N bonding in the material, a crucial part of the band gap and the quality of the material. This study will not only provide a better understanding of the effect of N on the alloy property but also on the observed differences between the quality of the layers grown under similar conditions by different researchers. Therefore a systematic study was conducted on the effect of N incorporation as a function of growth temperature, correlating the structural, bonding, electrical and optical properties of InSbN epilayers grown on GaAs substrate using various semiconductor material characterization techniques. This helped establish guidelines for further fine-tuning of the growth optimization.

► Reduction of carrier concentration: A systematic annealing study was carried out to reduce the most common problem of high *n* in the *as-grown* InSbN layers. The annealing studies of InSbN reported in the literature clearly indicated the improved quality of InSbN epilayers, however the data is scattered. Hence, *ex-situ* annealing by RTA was performed at various temperatures in order to establish an optimized annealing temperature which was also correlated with results published by some of the other research groups. After establishing the annealing temperature, *in-situ* annealing was attempted as this technique was already established by our research group to be more efficient. Furthermore, a comparison of the structural, vibrational, electrical and optical properties of *as-grown* and annealed (both *ex-situ* and *in-situ*) InSbN epilayers was also carried out. A relatively thick InSb buffer layer was observed to mask the electrical and optical properties of the InSbN epilayers. In order to minimize the interference of the InSb buffer in the study of InSbN epilayer properties, relatively thin buffers were grown.

► Heterostructure optimization: In order to optimize the InSbN heterostructure a systematic study was carried out to understand the variation of both InSb buffer layer thickness

and InSbN epilayer thickness on the quality of the InSbN epilayer. For this study different InSbN heterostructures were grown at the same growth condition. This clearly helped in distinguishing the defects in the InSbN epilayer that arise due to heteroepitaxy and N− related bondings along with their relative impact on the overall electrical property. Finally, using a combination of symmetric and asymmetric HRXRD and RSM scans the overall defects in the heterostructure were studied. The individual layer thicknesses were optimized in order to get the best InSbN heterostructure by using a correlation with N incorporation and Raman indicated defects.

1.5 Outline of the Dissertation

The dissertation consists of nine chapters. Below is a chapter wise outline of the research work presented in this dissertation.

Chapter 1 discusses about the division of infrared radiation into various spectral windows and related potential applications. This includes a brief history of the overall infrared technology and its development. Then the motivation behind this research work has been outlined. Subsequently, the challenges involved in the development of the InSbN material system were identified and the specific objectives of the present research are listed along with corresponding methodologies used to overcome those challenges.

Chapter 2 presents a focused review of the MBE growth of InSb on GaAs, band anticrossing in InSbN, various growth techniques of InSbN and its material characteristics reported to date. This is followed by a literature review of the defects in InSbN and its correlation with different N−bonding and different growth parameters are presented. Then the effect of annealing on the structural, electrical and optical absorption edge of the InSbN epilayers including different methods of band gap determination and InSbN based devices reported by different research teams are outlined.

In Chapter 3, a brief description of the MBE methodology and the MBE system used in our lab for the synthesis of all the test samples are presented. Various characterization techniques used to obtain a better understanding of the material behavior of InSb and InSbN are also documented and brief description of related physical principle is also included.

Chapter 4 presents a systematic study of InSb growth and its characterization, since a very large lattice mismatch between InSbN and GaAs necessitates the growth of an InSb buffer in these heterostructures for obtaining good quality epitaxial layers. This also includes the Sb/In BEP optimization, InSb growth temperature optimization and growth of highly crystalline InSb with high mobility and low carrier concentration. The results and discussion of this Chapter have been published[30] partially in a peer reviewed journal.

Chapter 5 discusses extensively the growth and characterization of InSbN heterostructures. First, a systematic study of variation of N plasma BEP within a narrow window of Sb/In BEP ratio (selected from the best results of InSb growth on GaAs) has been presented. Followed by the identification of stable and suitable N plasma BEP and finally, a brief systematic study on the effect of growth temperature on the N incorporation are reported.

Chapter 6 discusses about the understanding of the underlying principles for the formation of the N− bondings and their effect on structural, compositional, electrical and optical properties of InSbN. This also includes a discussion about the growth temperature dependent study, the influence of different N− bonding on the property of InSbN epilayers, and a comparison with the existing published results. All the results and discussion in this Chapter have been published[30] in a peer reviewed journal.

Chapter 7 presents a systematic study of various annealing processes performed on InSbN heterostructures in order to reduce high background *n* and defects in the epilayer. In order

to obtain an optimized annealing condition, multiple InSbN heterostructures were grown and *ex-situ* annealed at different temperatures. After observing a significant effect of annealing on the test heterostructures, a systematic study with variation in annealing temperatures and types of annealing were attempted. Subsequently, the effect of *ex-situ*, *in-situ* annealing on InSbN epilayers followed by a comparative study of both annealing processes were discussed. The annealing comparative study has been partially published in a peer reviewed[31]journal.

Chapter 8 discusses a systematic study of defects in various InSbN heterostructures. For high quantum efficiency a structure with minimum defect is desirable. In this chapter, various growth and structural aspects such as, thickness of InSb buffer and InSbN epilayer affecting the dislocation density in the overall InSbN heterostructure are also been discussed. And finally an optimized growth scheme of high quality InSbN heterostructure for device application has been suggested.

In conclusion, Chapter 9 discusses about all the major accomplishments and summary of every chapter. Various research efforts that were attempted to overcome the challenges are reported in this concluding chapter with relevant parametric quantitative figures. Finally, a suggestion of future work has been made after highlighting some of the best properties of InSbN material system which were accomplished in this dissertation.

CHAPTER 2

Literature Review

2.1 Why InSb

Among the entire group of III-V binary compound semiconductors, InSb has the distinction of exhibiting the smallest band gap of 0.18 eV with an absorption cutoff at 7.3 μm at 300 K.[31] This unique material property resulted in the selection of InSb for MWIR applications as discussed earlier. Further, a very high RT electron mobility can be taken advantage for a high speed device operation.[32, 33] After a multi-decade intensive research on the material property study for various applications, the production technology have been well developed starting from miniaturized InSb based sensors[34-36] to large format FPAs.[37, 38] Most of these devices are fabricated either on GaAs or Si for various applications with the, growth of InSb on GaAs taking the precedence.

In this chapter a brief review of various growth techniques is reported till date for both InSb and InSbN. Specific details of MBE growth parameters necessary for a high quality InSb layer growth on GaAs substrate are highlighted. The mechanism responsible for the band gap reduction in InSb with N incorporation has been discussed. A detailed review of various growth techniques used for InSbN and its correlation to the material properties as reported by other research groups has been attempted. A correlation of various N- bondings in InSbN with the defects reported by other research groups has been presented. A brief literature survey of the annealing effect on the property of InSbN has been included. Various types of annealing methods performed on InSbN grown by different growth techniques are also reported. A concise list of various techniques used to estimate the band gap of InSbN and related devices fabricated using different techniques by all the research groups reported till date has been tabulated.

2.2 Growth of InSb on GaAs

The growth of InSb on GaAs has been an important study for almost more than 40 years.[39, 40] Various techniques of growth like liquid phase epitaxy (LPE),[41, 42] metalorganic vapor phase epitaxy (MOVPE),[43] atomic layer epitaxy (ALE),[44] metalorganic chemical vapor deposition (MOCVD),[45-47] metalorganic magnetron sputtering,[48, 49] magnetron sputter epitaxy (MSE),[50] and molecular beam epitaxy (MBE)[37, 39, 40, 51, 52] have been studied. Brief literature review of InSb growth on GaAs by MBE technique will be presented here.

The focus of material research on the heteroepitaxial growth of InSb on GaAs substrates has been mostly on the improvement of the material quality with good electrical and optical characteristics for device applications. The heteroepitaxial growth of InSb on GaAs is plagued by the presence of high dislocation density due to the large mismatch of 14.6 % existing between the two binary systems. Hence, various MBE growth parameters namely, Sb/In flux ratio, substrate growth temperature and epilayer thickness become critical and strongly influences the overall quality of the epilayer. Noreika et al[53] first established various growth phases of InSb at different substrate temperatures and Sb/In flux ratios. Figure 2.1shows the different RHEED patterns observed during the MBE growth of (001) InSb with change in growth temperature and Sb/In flux ratio. This can be used as a guideline for the calibration of both the growth temperature and the Sb/In flux ratio for reproducible results. Further, the technique of growth temperature measurement using a standard pyrometer becomes erroneous at lower temperatures, particularly below 400 °C. Hence, observation of RHEED patterns of the growth surface dynamically during the growth process helps verify both the growth temperature and Sb/In flux ratio and can be considered as a feedback mechanism to correct both the parameters when needed. The RHEED observations indicated that the heteroepitaxial growth process includes: (a)

an initial nucleation 3D phase (spot pattern), (b) coalescence state between 500 and 3000 Å (streaky pattern formation), and (c) a sustained 2D surface demonstrated by various characteristic patterns mentioned in Figure 2.1.[53, 54] A thickness dependence of the Hall mobility and x-ray rocking curve full width half maxima (FWHM) of InSb epilayers studied for thickness variation1 to 35 µm thick, grown at 390 °C indicate improved structural quality with increasing thickness and a bulk-like behavior beyond 30 µm.[54]

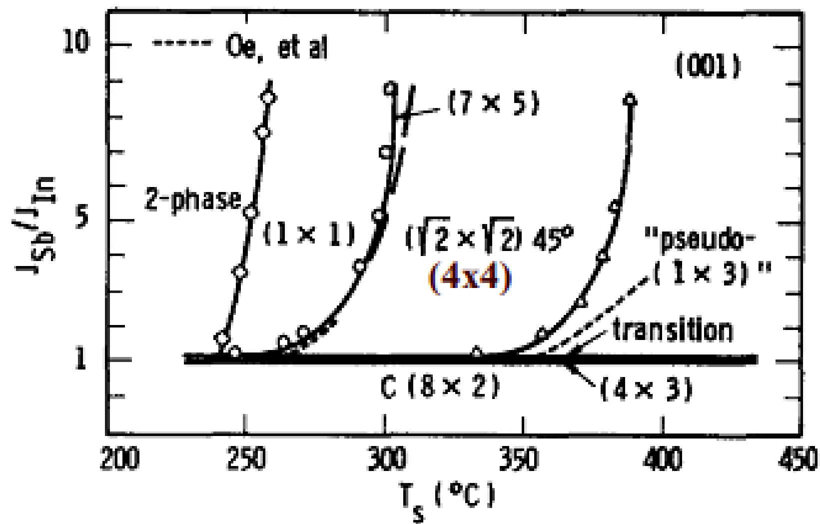

Figure 2.1. Diagram showing various RHEED patterns observed on (001) InSb surface.[53]

Eventually, various other growth techniques were suggested to improve the structural quality and Hall mobility such as, Davis et al[55] reported the growth of a 300 Å InSb interface layer at 300 °C prior to the growth of InSb active layer at 380 °C with rocking curve width ~ 100 arcsec for 10 µm thick layers. Further, a higher mobility of 55,100 and 38,300 cm^2/V-sec observed at 300 and 77 K, respectively in the 5.5 µm thick InSb layer indicated relatively less defects due to the presence of the interface layer.[44, 55] The interfacial study from TEM[56-58] and RHEED[58] study of initial stages of the heteroepitaxial growth of InSb on GaAs indicated a reduction in dislocation density with increase in layer thickness and away from the interface with values ranging from $\sim 10^{11}$ to 10^6 cm^{-2} for thickness varying from 0.2 to 10 µm thick InSb layer.

Apart from the incorporation of an InSb buffer layer, Li et al[59] reported the incorporation of a 3000 Å AlSb buffer layer in a 3 μm InSb on GaAs to improve the rocking curve width to 199 arcsec with RT Hall mobility at 55,000 cm^2/Vs and good absorption characteristics in the IR spectral range. Michel et al[60] reported a more careful growth technique by optimizing the growth temperature and Sb/In flux ratio by using static and dynamic RHEED with a controlled InSb nucleation process. The calibration of flux using this technique was reported to be more accurate than the standard beam equivalent pressure (BEP) measurements as the latter was dependent on the history of the ion-gauge but not the kinetics at the surface during the growth. This technique was observed to yield a much better quality of InSb heterostructures than the earlier reported techniques of additional incorporation of low temperature thin atomic layer epitaxially grown InSb or an AlSb buffer layer. A 3.3 μm thick InSb layer grown at 395 °C and an Sb/In flux ratio of 1.2 calibrated using RHEED, observed to exhibit a x-ray FWHM of 193 arcsec, with 300 and 77 K Hall mobilities of 59,400 and 81,500 cm^2/Vs, respectively.[60]

A characteristic temperature dependent study of the mobility with a peak at 80 K indicated the bulk like behavior of the InSb epilayer with n-type background. Further, a thickness dependent study carried out on a 4.8 μm InSb layer grown under an optimum condition described by Michel et al[60] clearly indicated both 300 and 77 K mobilities limited by dislocation scattering for thickness below 1.5 μm. The 4.8 μm thick sample was reported to exhibit a Hall mobility of 62,300 and 92,300 cm^2/Vs at 300 and 77 K, respectively with an x-ray FWHM of 158 arcsec.[60] Further, our work[30] on the MBE growth of InSb on GaAs indicated, the use of RHEED for growth optimization not only resulted in a high quality InSb epilayer on a GaAs substrate but also provided reproducible results due to its dynamic nature. Hence, this technique was used for the growth of InSb buffer layer in all the heterostructures reported in this study.

2.3 Bandgap Reduction in III-V-N Materials

The phenomena of band gap reduction with N incorporation in group III-V semiconductors started attracting attention in the 1990s. When a dilute amount of nitrogen replaces the group V atoms in the host material, the fundamental band gap was observed to be affected due to variation in atomic size and electronegativity. Although there are many theories that explain this band gap reduction, band anticrossing (BAC) model is the most widely used due to its simplicity.[61-65] A comprehensive summary of various dilute nitride materials can be found in the doctoral dissertations of Dr. Kalyan Nunna,[66] Dr. Liangin Wu,[67] Dr. Sudhakar Bharatan[68] and Dr. Homan Yuen[69].

2.4 Band Anticrossing in InSbN

The band gap reduction in InSb with dilute amount of N incorporation was first reported by Murdin et al[70] and was explained by using a modified k.p Hamiltonian previously[71] developed for GaN_xAs_{1-x}. Figure 2.2 (a) shows the band structure calculated as a function of N composition and (b) gives the details of band gap variation over mid to long wavelength range with change in N content.[21]

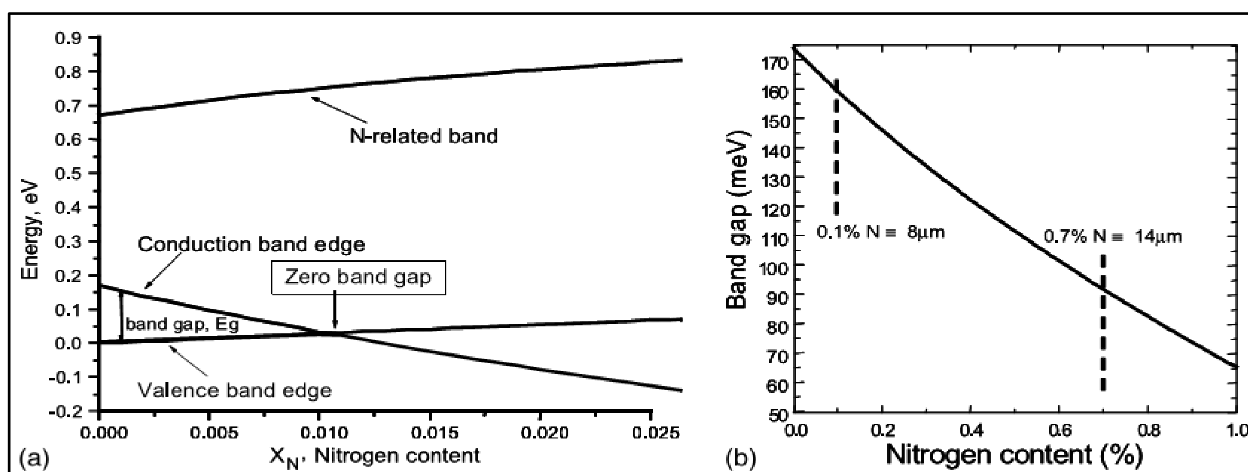

Figure 2.2. (a) the calculated band structure as a function of nitrogen composition, (b) the band gap variation over the mid to long wavelength IR range for $InSb_{1-x}N_x$.[21]

Eventually, Lindsay et al[72, 73] reported the need of a two-level BAC model to explain the band dispersion near the conduction band minimum (CBM) in InSbN. In this model the CBM dispersion was calculated using a 10 band k.p Hamiltonian and BAC parameters. Bhusal et al[74] reported a 10 band k.p model, similar to one proposed by Tomic et al[75] for GaNAs/GaAs QW to account for the localized nitrogen band interaction with CB and VB in $InSb_{1-x}N_x$. Based on the simulation results a RT cutoff wavelength of 10-25 µm was reported to be possible in InSbN with nitrogen concentrations between 0.5 and 1.3%.[74]

2.5 Growth and Characterization of $InSb_{1-x}N_x$

Johnson et al[76] first reported the growth of InSbN light emitting diodes (LED) grown by MBE. To determine the effect of N on the band gap (E_g) they have reported the growth and fabrication of $InSb/InN_xSb_{1-x}$ superlattice active regions with period ~ 1000 Å for a nitrogen content of x = 0.3 % resulting in the peak emission shift from ~6 to >7 µm at RT.[76] Ashley et al[21] reported a systematic MBE growth of both bulk InSbN and superlattice structures comprising 83 nm InSb/ 33 nm InSbN at 380 °C on a 1 µm InSb buffer using an electron cyclotron resonance (ECR) N plasma source. The TEM and AFM results indicated a significant increase in the epilayer interface visibility and improved surface morphology with application of a bias voltage to the substrate during the growth of nitride layer. Application of a bias voltage is believed to reduce the density of the high energetic ions from the N plasma impinging on the growth surface. Further, a threading dislocation density (~10^8 cm^{-2}) was reported to propagate from the superlattice region to the sample surface. An increase in N incorporation from 2 to 4.6 % with an increase in ECR power from 1 to 100 W was reported to accompany with the morphology degradation. Further, N incorporation was reported to vary by two orders of magnitude with introduction of hydrogen at a pressure of $5x10^{-6}$ mbar. A maximum incorporation of 10 %

nitrogen limited by the pumping capacity of the reactor was reported from the SIMS and XRD results. The InSbN SL device was reported to exhibit a near RT emission peak at ~7 µm with N~ 5.5 % as compared to pure InSb devices with peak at ~ 6 µm. Although, a shift in the emission peak at a higher wavelength was observed, the magnitude of this shift deviated from the theoretical prediction corresponding to the N incorporation. This deviation was reported to be accounted by Moss-Burstein shift due to high background *n* in InSbN layer. RT *n* ranging from 1.9×10^{17} cm^{-3} to 1.3×10^{18} cm^{-3} with RT μ from 6,500 to 3,250 cm^2/V-s, respectively was reported for N concentrations varying from 0.6 to 2 %, respectively. These Hall measurements were reported to be carried out on the bulk $InSb_{1-x}N_x$ samples grown on semi-insulating GaAs substrates to avoid parallel conduction.[21]

With the passage of time as this material system gained attention of other researchers, various growth techniques like low pressure MOVPE,[77] MOCVD,[78] ion implantation,[79, 80] MBE equipped with electron cyclotron resonance (ECR)[21] and MBE equipped with rf N plasma[30, 81-83] were used for the growth of InSbN for long wavelength detection. Mahboob et al[84] reported the determination of substitutional nitrogen content in $InSb_{1-x}N_x$ using the method of high-resolution electron loss spectroscopy (HREELS) and Hall studies using epilayers grown on GaAs substrates by MBE. Estimation of the N content from HRXRD data using simple Vegard's law have been reported to be inconsistent with data from SIMS and XPS for other dilute nitride systems like $GaAs_{1-x}N_x$ grown on GaAs substrates.[85, 86] Hence, a method like HREEL spectra which probes the electronic structure near-surface region of the material by means of low-energy electrons which couple to the electric fields of surface plasmons arising from the free carriers in the CB resulting in the electron energy loss spectra. This was reported to be self-consistent method to derive the substitutional nitrogen (N_{Sb}) purely based on electrical measurements.[84] A correlation

of HREEL spectra with the RT Hall data of $n = 9 \times 10^{18}$ cm^{-3}, $\mu = 1400$ cm^2/Vs and modified k.p model was reported to result in x = 0.0015. And this x value was reported[84] to suggest only 7.5 % of the total nitrogen determined from the SIMS alloy composition, to be in the substitutional position. The remaining nitrogen was speculated to be either in interstitial lattice sites, indium sites or passivated by the atomic hydrogen incorporated during the epilayer growth. The E_g estimated for x = 0.0015 in $InSb_{1-x}N_x$ was reported[84] to be 135 meV, consistent with the LED device output peak[21] fabricated using this material.

Jefferson et al[87] reported a very narrow growth temperature window of 330±5 °C for N incorporation. However, Pham et al,[81] Lim et al[82, 88, 89] and Zhang et al[83] reported growth of InSbN from 270 ~ 420 °C for different rf N plasma powers. The variation in the observation of the growth temperature window for Jefferson et al[87] can be due to the use of Sb_4 from a standard antimony (Sb) effusion cell as against to Pham et al[81] who reported to use a valved cracker cell for Sb operating at 900-1000 °C providing a stable beam of Sb flux[90] comprising more than 90 % Sb_1.

2.6 Study of Defects in InSbN

In recent years, the growth of InSbN by MBE equipped with nitrogen rf plasma source observed to be widely studied.[81, 88] The growth mechanism of InSbN was suggested by Lim et al[88] using an anion exchange model. During the process of nitridation, formation of bonding such as In–N along with In–Sb–N, Sb–N and Sb–Sb (Sb antisite) as a concurrent process was suggested. A systematic defect study of the growth parameters indicate Sb antisite defects (Sb sitting on In site) characterized by A_{1g}Sb peak in the Raman spectra, reported to be dominant at high growth temperature and at a low plasma power.[88] Further, the presence of nitrogen in the interstitial positions in the form of various nitride bonding like N–Sb, $-NH_2$, $-NH_3$, –NO, N–N

was reported by Veal et al[91] from the N 1s x-ray photoelectron spectra (XPS) of the *as-grown* InSbN samples, whereas the substitutional N was in the form of In-N bonding. The presence of these N– related bonds was reported to create lattice compression or expansion in InSbN based on the type of bonding.[81] Interstitial N complexes such as [110]-split interstitial N–N, [100]-split interstitial N–N and substitutional In–N (N_{Sb}) was reported[81] to create lattice contraction (negative lattice mismatch) whereas, the interstitial N–Sb ([100], [110], and [111]) and [111]-split interstitial N–N structures lead to lattice expansion (positive lattice mismatch). These studies were carried out on ~ 0.6 μm InSbN epilayers grown on InSb substrates at various growth temperatures and rf N plasma power. From (115) XRD reciprocal space maps (RSM) study the nitride layers were reported to be strained with the strain value dependent on the growth temperature and plasma power.[81] The nature of N bonding and origin of N− related defects as a function of the growth temperature studied by Pham et al[81] seems to explain the crystal disorder observed in the InSbN material system as reported by Lim et al.[88] Hence, InSbN epilayers not only suffers a structural degradation from the heteroepitaxy but also from various disorders associated with the N– related bonding.

2.7 Effect of Annealing on InSbN

Various annealing methods were studied to observe its effect on the structural, compositional, electrical and optical properties of InSbN layers. Veal et al[91] first reported the effect of annealing at 300 °C performed radiatively using a tungsten filament on the MBE grown InSbN epilayers. The N 1s XPS study of the annealed InSbN layers were reported to exhibit an increase in In-N bonding and reduction in other N– related bonding except Sb–N, after 8 hours of annealing at 300 °C.[91] Buckle et al[92] reported a reduction in RT carrier concentration (n) of 2 μm thick InSbN layers grown on GaAs substrates from ~10^{18} to ~10^{17} cm^{-3} after *ex-situ*

annealing at temperatures higher than 400 °C. Further, an InSb grown under the same condition reported to exhibit RT *n* in the range of ~10^{16} cm^{-3}. The high RT *n* observed in the *as-grown* InSbN epilayers are mostly due to the N–N interstitials and their donor nature.[93] A comparative study of furnace annealing and RTA by Chen et al[94] for ion implanted InSbN alloys, indicates the former technique to be better in elimination of defects while later activated more N. Further, Wang et al[95] reported the accumulation of out-diffused nitrogen on the surface and interstitial dominated diffusion of implanted N into the bulk of InSb substrate after a prolonged furnace annealing at 277 °C for InSbN alloys fabricated by two-step ion implantation. The effect of annealing on the optical absorption edge of the material will be discussed partially in the next section and in a great detail in Chapter 7.

2.8 Bandgap Determination of InSbN

An accurate determination of the E_g far in the MIR or LWIR can be very difficult. A photo-luminescence is usually very weak in narrow gap semiconductors due to low carrier life time. Transmission measurements can also be misleading due to broad peak and spectra being masked by interference patterns. Hence, using a Fourier transform modulated spectroscopy technique,[96] Merrick et al[97] reported a 16 meV (~10 %) redshift in the InSbN at RT with 0.1 % N incorporation. Eventually, as this technique was accepted by many others, its wide use resulted in many commercial products under the domain of Fourier transform infrared (FTIR) spectrometers. Further, a straightforward calculation of the E_g from the absorption edge may not be accurate, when the background carrier concentration is high and causing a blue shift in the absorption edge, commonly known as Moss-Burstein effect. In such cases, the E_g of InSbN is calculated as

$$E_g = E_{abs} - E_{MB} + E_{BGN} \tag{2.1}$$

where, E_{abs} is the optical absorption edge energy from FTIR, E_{MB} the energy shift due to the Moss-Burstein effect and E_{BGN} the band gap narrowing energy.[82, 98] Lim et al[82] reported to observe a blue shift in the cut-off wavelength up to 4.8 μm (0.26 eV) for 2 μm thick InSbN grown at 270 °C exhibiting high n in the order of $\sim 10^{18}$ cm^{-3}. Whereas, the E_g calculated using Equation 2.1 was reported to be 0.1 eV corresponding to 1 % N_{Sb}. Further, InSbN layers grown at 380 °C reported to exhibit longer cutoff wavelength at ~8 μm (0.16 eV) with $n \sim 10^{17}$ cm^{-3}, the calculated E_g (= 0.16 eV) corresponding to 0.2 % N incorporation. This clearly indicates the dominance of Moss-Burstein effect at high carrier concentrations for InSbN layers grown at low temperatures and high N incorporation. Hence, one way to reduce the Moss-Burstein shift by reducing the carrier concentration is by increasing the growth temperature of InSbN epilayer. Another way is by annealing the InSbN layers at temperatures higher than 400 °C. Buckle et al[92] reported to experimentally observe a red shift in the absorption edge of InSbN epilayers after *ex-situ* annealing at 410 °C caused by reduction in n up to $\sim 10^{17}$ cm^{-3} with λ cut off extending to ~ 8.5 μm and 0.3 % N_{Sb}. A similar behavior was reported by Lim et al[93] for InSbN layers *ex-situ* annealed at 430 °C with an observed red shift in absorption edge to 0.15 eV (~8 μm) corresponding to 0.3 % N_{Sb} (BAC predicted) and $n \sim 10^{17}$ cm^{-3}. However, the technique of E_g estimation using FTIR necessitates the InSbN epilayers need to be relatively thick (~2 μm) and grown on semi-insulating substrate for a high absorption only in the epilayer. Further, in order to estimate the band gap, the shift in the absorption edge due to Moss-Burstein effect needs to be accounted for the epilayers with high background carrier concentration.[99, 100]

The photoluminescence (PL) peak energy can also be used to determine the E_g for InSbN alloys. However, in order to obtain a PL peak, highly crystalline InSbN layers need to be grown with reduced defects and hence less non-radiative recombination centers. Jin et al[78] reported the

10 K PL spectra of homoepitaxially grown InSbN epilayers on InSb substrates using MOCVD. A PL peak at ~5.27 µm (0.235 eV) and ~5.4 µm (0.23 eV) observed were reported to be due to InSb and InSbN band to band transitions, respectively. Another peak at 5.87 µm (0.211 eV) observed for almost all the InSbN samples except the InSb substrate was reported to be due to Sb antisites (Sb_{In}). The InSbN E_g estimated from PL was reported to match the photocurrent peak measured at 30 K after accounting for the band gap narrowing effect. Using the 10 band k.p model, the N content was reported to be estimated at 0.07 %. However, a slight discrepancy reported in the mismatch values from the XRD experimental results and theoretical calculations using Vegard's law were not explained.

Another method of determination of E_g is by fabrication of a device with InSbN as active layer which will be discussed in next section. Table 2.1 summarizes the growth of various types of InSbN based devices/epilayers and corresponding band gaps reported in literature.

2.9 Devices Based on InSbN

For any real time application the InSbN material need to be fabricated into a device. The different types of devices fabricated with InSbN as active layers are LED[21] and P-N diode[101, 102] for photo detection. Photoemission peak was reported at 10 K for InSbN/InSb based SL with pump photon energy of 0.26 eV (~4.9 µm), the E_g of the SL at this temperature being 0.124 eV (~10 µm) with a carrier lifetime of 130 ps.[21] P-N junction fabricated by Chen et al[101] using 3 step ion implanted InSbN was reported to exhibit photo current peak around 6.47 µm at 30 K with cut off λ extended to ~ 9.4 µm. The E_g in this case was estimated to be ~191.7 meV. The active layer was annealed at 550 K for 4 hours in order to remove damage caused by implantation and activate the incorporated N which was estimated from XPS to be 0.43%. The p-type doping was accomplished by Mg^+ implantation.[101] Further, p^+-n structure fabricated on GaAs substrate by

Table 2.1

Table to summarize the growth and E_g reported for InSbN by various research groups

Research Group	Device type	Growth technique	E_g (meV)	Method of E_g determination	Estimated N (%)
Ashley et al	InSbN/InSb SL LED	MBE equipped with ECR N plasma	124	Photoemission	10
Chen et al	P-N diode (detector)	3 step ion implantation	196.7	Photocurrent	0.36
Chen et al	P-N diode (detector)	3 step ion implantation	195.5	Photocurrent	0.43
Chen et al	P-N diode (detector)	3 step ion implantation	191.7	Photocurrent	0.36
Buckle et al	InSbN epilayer on GaAs substrate	MBE	180	FTIR α plot	0.2
Jin et al	InSbN epilayer on InSb substrate	MOCVD	221 at 30 K	PL	0.7
Jin et al	InSbN epilayer on InSb substrate	MOCVD	224 at 30 K	Photocurrent	0.7
Lim et al	InSbN epilayer on GaAs substrate	MBE with rf N plasma	150	FTIR α^2 linear interpolation	0.3
Lim et al	p^+-n diode (detector)	MBE with rf N plasma	137 at 20 K	Photocurrent	1

Lim et al[102] reported an extension of 30 K photocurrent upto ~9 μm. These structures consist of annealed InSbN with N_{Sb} ~1 % and n ~10^{16} cm^{-3}. The p^+ layer was reported to be a 50 nm thick C-doped InSbN with doping concentration of ~10^{19} cm^{-3}. The conduction of current reported at small bias attributed to the presence of shallow levels caused by the excess Sb atoms.

2.10 Conclusion

In conclusion, optimization of growth temperature and Sb/In flux ratio along with dynamic RHEED patterns high quality InSb epilayers can be grown on GaAs substrates. The band anticrossing model has been successfully used to explain the band gap reduction in InSbN with increasing N incorporation and predicts extension of the absorption to ~14 μm at ~1.1 % N. Irrespective of different growth techniques used for the synthesis of InSbN epilayers, the defects and electrical properties characteristic of the type of N− bonding present. Annealing studies were reported to reduce the background n due to annihilation of N−N interstitials with absorption cut off extended up to 8 μm at RT. Band gap of InSbN estimated from various methods clearly indicated a reduction from the InSb E_g with increase in N incorporation.

CHAPTER 3

MBE Growth and Characterization Techniques

3.1 MBE Overview

MBE is considered to be one of the state-of-the-art ultra-high vacuum (UHV) non-equilibrium techniques[103] for the growth of highly crystalline epitaxial compound semiconductors. As the MBE technique allows the control of the thickness to an atomic level and abrupt change in the atomic composition with sharp interfaces, the growth technique lends not only for the epitaxial growth of highly quality for nearly lattice matched condition but also for highly lattice mismatched condition using strained layer epitaxy.[104]

In this chapter a brief description of the MBE methodology and the MBE system used in our lab for the synthesis of all the test samples are presented. A step wise growth sequence for the growth of InSb and InSbN epilayers is listed. Various post growth processing and material characterization techniques used for understanding the material behavior of InSb and InSbN are also discussed along with a description of related physical principles.

3.2 MBE Elemental Sources and Components

Figure 3.1 shows the VEECO EPI 930 solid source MBE equipped with rf N plasma, used for the growth of InSb and InSbN heterostructures for this study. The details of all the solid sources, N plasma and other essential MBE components like, RGA, vacuum pumps, ion gauges, RHEED, pyrometer, temperature controllers etc. used in our MBE system are reported in the dissertation of Dr. Liangin Wu,[67] Dr. Kalyan Nunna,[66] and Dr. Sudhakar Bharatan[68] for their research work carried out using this MBE system prior to this work. Hence, in this report the discussion will be limited to only the MBE growth parameters significant to the growth of InSb and InSbN heterostructures on GaAs substrates.

For GaAs buffer layer a dual filament Knudsen cell loaded with 7N purity Ga and an As cell with valved cracker loaded with 7N purity source was used. For both InSb buffer and InSbN epilayers a dual filament Knudsen cell loaded with 7N pure In was used. The Sb was supplied using a valved cracker source loaded with 7N pure Sb. Both As and Sb crackers were maintained at 900 °C during the operation for a continuous supply atomic As and atomic Sb flux at the cracking temperature. The nitrogen was supplied by converting purified N_2 gas into plasma using a rf controlled plasma source. The N plasma was fired only after setting the growth conditions for InSbN growth to prevent N incorporation in any other grown layers.

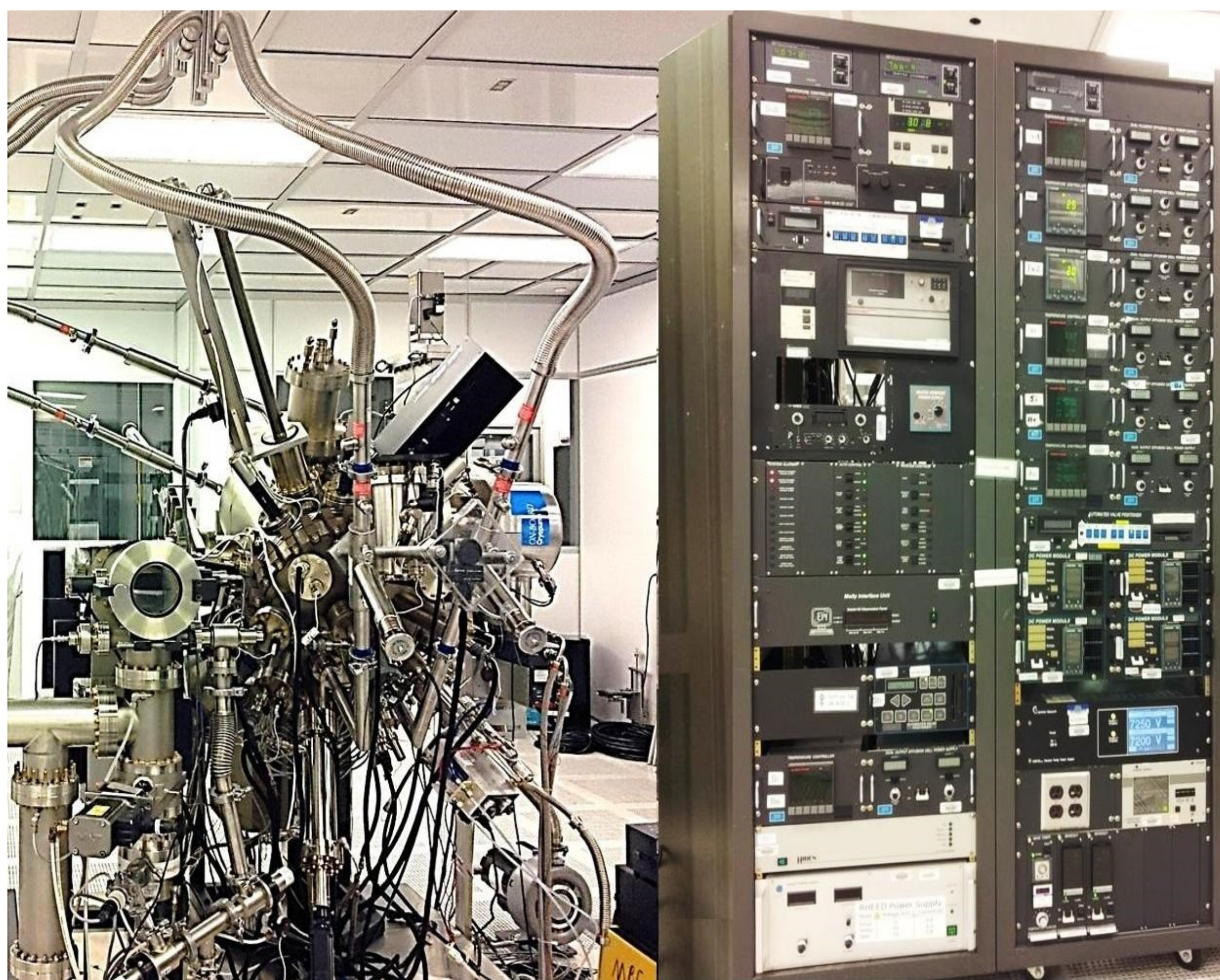

Figure 3.1. The EPI 930 MBE system along with electronic control rack in the clean room facility.

All the beam equivalent pressure values (BEP) were measured by an ion gauge prior to the growth of the epilayers. All the sources were controlled by rapid shutter action that allows the production of an abrupt interface. The BEP of group III elements (Ga and In) were controlled by the source temperature whereas, in the case of group V elements (As and Sb) the BEP values were controlled by both the source temperature and cracker valve position. The N plasma BEP was controlled by a gas flow control valve, manual leak valve and rf plasma power. Since ion pump has a high pumping capacity for nitrogen, the ion pump gate valve was closed prior to the introduction of N into the growth chamber. The N plasma BEP was measured by the chamber pressure after firing the N plasma. The N plasma shutter was opened only after the stabilization of N BEP and plasma fire which could be monitored by observing the brightness of the plasma through a view port.

All the heterostructures were grown on semi-insulating epi-ready (001) GaAs (single side/double side polished) substrates. The substrates were 10x10 mm^2 in surface area cut from a 2" diameter, 0.5±0.025 mm thick GaAs wafers with etch pit density ≤ 2000 cm^{-2}. These GaAs wafers were purchased from Wafer Technology Ltd. After cutting the wafer, a GaAs substrate was loaded onto a molybdenum sample holder consisting of two spring plates and a snap ring. Prior to the growth process these substrates were radiatively heated for 8 hrs at 200 °C using two halogen lamps inside a chamber with pressure maintained better than 10^{-7} Torr, to remove water vapor and any other volatile material from the growth surface.

3.3 Growth of InSb on GaAs

Below are the steps followed in sequence during the growth of InSb on GaAs substrate.

1. GaAs oxide desorption was carried at 614 °C under an As overpressure.
2. The oxide desorption was confirmed by a streaky (1x2) or (2x4) RHEED pattern.

3. After a good oxide desorption (observed by high intensity RHEED patterns), GaAs buffer (0.2 µm) was grown at 580 °C.
4. After the growth of GaAs buffer the substrate was cooled with As overpressure until 500 °C. Then the InSb growth temperature was extrapolated taking at least five data points using 0.5 emissivity in the pyrometer controller settings.
5. InSb buffer (variable thickness) was grown at 375 °C under 2√2x2√2 or pseudo (1x3) RHEED pattern.
6. After the growth of InSb under a streaky RHEED pattern the In shutter was closed to terminate the InSb growth.
7. The Sb shutter was kept open until substrate temperature was cooled below 330 °C.

3.4 Growth of InSbN on GaAs

After a successful growth of InSb buffer following steps were followed for the growth of InSbN.

1. In order to determine the growth temperature for InSbN the substrate temperature was increased with in a temperature range of 410-440 °C for extrapolation using at least 3 data points. Sb over pressure was maintained at this high temperature to prevent any outgas of Sb from the InSb buffer layer.
2. After the determination of InSbN growth temperature, the substrate temperature was reduced with an uninterrupted InSb growth at a relatively lower growth rate of ~0.4 µm/hr.
3. At the InSbN growth temperature (270~380 °C) the N-plasma was fired and adjusted for a stable and bright plasma glow. The N plasma was controlled by rf plasma power and the N gas flow.

4. The InSbN growth was carried out at the selected growth temperature by opening the N plasma shutter after the stabilization of N BEP observed by the chamber background pressure using a high vacuum ion-gauge.
5. A typical RHEED pattern of *c*(1x3) was observed during the growth of InSbN epilayers.
6. After the growth of required thickness of InSbN epilayer the growth was terminated by closing In, Sb and N shutter in sequence followed by lowering of the substrate temperature to room temperature.

3.5 Post Growth Processing: Annealing

Two types of annealing methods were carried out in order to study the effect of annealing on these MBE grown InSbN heterostructures.

1. *In-situ* annealing: In this technique the process of annealing was carried out inside the MBE growth chamber immediately after the growth of InSbN epilayer. After the termination of InSbN growth, the substrate temperature was increased to the desired annealing temperature with regulated Sb overpressure (2×10^{-6} Torr) at a ramp rate of 0.5 °C/sec. Once the sample was annealed for a desired duration the substrate temperature was lowered to room temperature with Sb overpressure kept on until the temperature fell below the InSbN growth temperature.
2. *Ex-situ* annealing: In this technique the process of annealing was carried out outside the growth chamber after the growth of InSbN. Here, for this study we have used Jepelec JetFirst 100 rapid thermal annealing (RTA) system in the Duke Shared Materials facility with a regulated flow of N_2 gas at 1500 sccm. A ramp rate of 20 °C/sec was selected while increasing the substrate temperature. The temperature was recorded using a standard thermocouple calibrated to measure the temperature of the Si wafer on which

the test sample was placed. An InSb wafer was placed on top of the InSbN sample during the process of RTA to prevent any excess loss of Sb.

3.6 Characterization Techniques

After the MBE growth of InSb and InSbN epilayers various semiconductor characterization techniques were used to analyze the structural, compositional, electrical and optical properties. Some of these techniques such as x-ray photoelectron spectroscopy, secondary ion mass spectroscopy and nuclear reaction analysis are destructive in nature. Hence, only a small piece cut out from the grown structure was used for these characterization techniques. It is to be noted that some of the characterizations were performed at other lab facilities namely Shared Materials Instrumentation Facility at Duke University after a certified training and some by expert personnel from Evans Analytical Group. The thickness values of the epilayers were measured using a Tencor thickness profiler from the step size of the grown layer taking GaAs substrate as the reference.

3.6.1 RHEED. The reflection high energy electron diffraction is considered to be a very powerful technique during the MBE growth of thin films due its non-destructive, *in-situ* and dynamic nature of the characterization. A high energy (20 KeV) electron beam directed towards the sample at a grazing angle. Due to a low angle of incidence (~2°) the incidence beam penetrates only a few atomic layers and gets diffracted onto a fluorescent screen creating a visual pattern. These visual diffracted beam patterns provide information on the behavior and atomic regularity at/near the surface. Hence, in-situ observation of the evolution of these patterns is used to understand the growth mechanism. For instance, inference of 3D or 2D growth can be made depending on the RHEED pattern to be spotty or streaky, respectively. These RHEED patterns can be recorded dynamically by using a CCD camera connected to a computer, as individual

images or continuous videos for detailed post growth analysis. In this study, a kSA 400 system manufactured by k-Space Associates, inc. equipped with an optical camera and software was used for recording and analyzing the RHEED patterns. A detailed study on the analysis of the RHEED data can be found in some of the work done by researchers in past.[104-109]

3.6.2 HRXRD. The principle of highly coherent beam of x-rays diffracted from a set of parallel planes following Bragg's law is used for characterization of epitaxial layers due to its non-destructive nature. These high resolution xray diffraction spectra can be used to provide information about the crystallographic structure, alloy composition and other heterostructure characteristics namely, strain, relaxation, dislocation density, tilt and lattice parameters.

All the HRXRD scans were performed using a Bruker Bede Scientific D1 system attached to a 2.2 kW sealed microsource x-ray generator. The Cu $K\alpha_1$ x-ray line is selected using a cut-channel crystal and a precision slit. The incidence beam was collimated by incidence optics and limited by a round slit of diameter 2 cm. The sample was placed on a vertical sample holder with the help of a double sided sticky tape such that the beam is incident on the center of the test area. The diffracted beam was detected with a 0D scintillation detector with an angular acceptance limited by a 0.1 mm wide slit. All the rocking curve (ω and coupled 2θ-ω) measurements were performed and recorded using a computer controlled gonio meter. The (004) symmetric scans were performed after optimizing the sample orientations (z, chi and ω) for a high intensity peak for GaAs substrate. Similarly, (115) asymmetric scans were performed at a grazing incidence after optimizing for a well resolved high intensity GaAs substrate peak.

Every peak in the acquired 2θ-ω plot corresponded to a specific epilayer in the test structure. The intensity of the peak is a function of epilayer thickness and the FWHM depends on the structural orientation of the epitaxial layers.

3.6.2.1 Compositional analysis from HRXRD. After acquisition of (004) 2θ-ω plots the compositional analysis was carried out using the RADS Mercury software, which employs the dynamic simulation of the x-ray intensity diffracted from a layered structure. The software takes the values for the thickness and composition for the individual layers within a given range as an input. After performing thousands of iterations of a genetic algorithm based on Vegard's law with the default bowing parameters, the software provides a unique solution in a couple of seconds based on the best data fit. Figure 3.2 shows the screen shot of the simulation of a typical InSbN heterostructure grown at 290 °C and Figure 3.3 shows the corresponding layers used to fit the data.

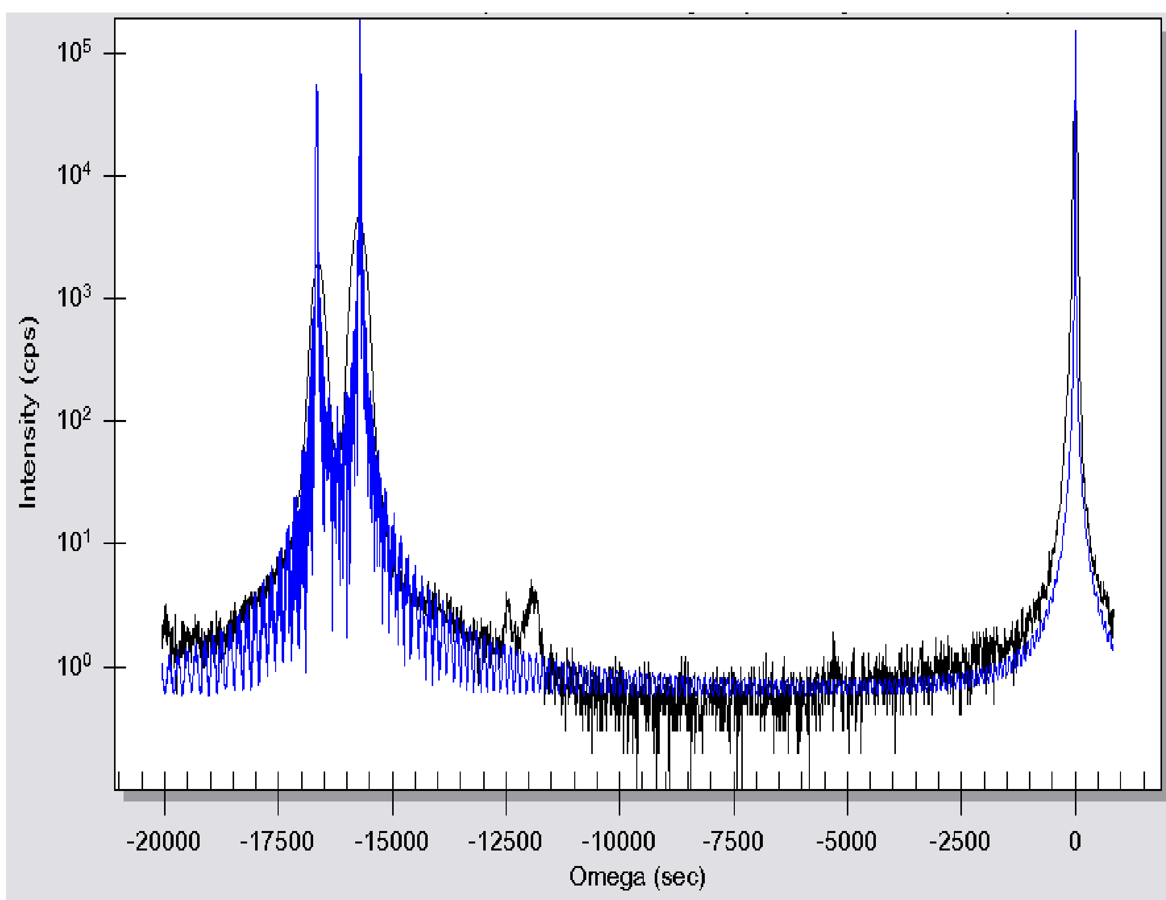

Figure 3.2. A screenshot of the (004) HRXRD simulation of InSbN/InSb/GaAs heterostructure performed by RADS mercury software.

Layers | Diffuse Scatter

	THICKNESS (Å)	fix	low	high	MATERIAL	X	fix	low	high
3	10200.09	☐	10000	15000	InSb(1-x)N(x) ▼	0.0166	☐	0.015	0.02
2	8167.41	☐	5000	10000	InSb ▼	0.0000	☐	0	0
1	3836.04	☐	1000	5000	GaAs ▼	0.0000	☐	0	0
SUB.	∞	☑	∞	∞	GaAs ▼	0.0000	☐	0	0

Figure 3.3. A screenshot of the individual layers and corresponding parameters used in the software for the simulated data in Figure 3.2.

3.6.2.2 Estimation of dislocation density. The dislocation density (D) of the epilayers was estimated using[110] the corresponding FWHM of the HRXRD peak using the expression

$$D = {}^{\beta^2}/_{9b^2}\ cm^{-2} \qquad (3.1)$$

where, β is the HRXRD rocking curve FWHM in radians and b is the magnitude of the Burgers vector (5.646 Å/ $8^{1/2}$) ≈ 2 Å.[111] The square dependence of D on the HRXRD FWHM indicates that a small change in the peak broadening is due to a variation in large number of dislocations in the sample. Hence, the HRXRD FWHM values can be used to compare the defects/dislocations in the heterostructures both qualitatively and quantitatively, when the peak broadening is predominantly due to dislocations.

3.6.3 RSM. The reciprocal space map studies for these heterostructures were used to examine the strain relaxation, crystalline quality, lattice parameters, tilt, and compositional gradient. These scans were carried out using Panalytical X'Pert Pro MRD X-Ray Diffraction system. The triple axis measurements were done using a PreFIX module which combines a triple axis and rocking curve attachment designed for rocking curve measurements and reciprocal space maps. It provided two different diffracted beam path options. One path was the rocking curve attachment, equipped with a slit holder for mounting slits in front of the detector to reduce the beam acceptance angle. The second path carried an analyzer crystal to convert the

diffractometer to triple axis mode for reciprocal space maps. The analyzer crystal was a channel cut Ge crystal where, the diffracted beam had to undergo two (220) reflections within the groove before entering the detector. The acceptance angle of the analyzer crystal was 12 arcsec. All the asymmetric (115) scans were performed in a glancing incidence mode. After the data acquisition the scans were plotted using X'Pert Epitaxy software and analyzed for various structural parameters. A standard 1/2° slit was used in the incidence beam path to limit the incoming x-rays.

A contour plot of ω-2θ vs ω was acquired and converted into a reciprocal space map using X'Pert Epitaxy software with axes Q_x vs Q_y in reciprocal lattice units (rlu). The individual layer peaks were identified and the values of mismatch estimated for further analysis. The asymmetric (115) scan was used to determine the parallel and perpendicular mismatch. The perpendicular mismatch values were confirmed from another independent (004) symmetric scan. Using the d-spacing values from corresponding RSM plots the lattice constant for the GaAs substrate, InSb buffer layer and InSbN epilayers were estimated.[112]

3.6.4 Micro-Raman spectroscopy. The study of Raman spectra provides information on the presence and absence of defects in the crystal depending on the mode of vibration observed in the spectra. The micro-Raman spectroscopy was performed using Horiba Jobin Yvon LabRam ARAMIS system. The word 'micro' is used to indicate the sampling dimension to be in microns. Hence, the acquired scan reflects the crystallographic property of the sampling volume only. In this case, a 632 nm He-Ne red laser was used for the excitation with an approximate diameter of 50 μm beam spot size focused on to the sample surface under study. The instrument was calibrated using a standard Si sample to observe a peak at 520 cm^{-1}. It is to be noted that, due to low growth temperature of InSbN, a highly focused laser beam can cause damage at the focused

spot. This phenomenon was observed using an optical microscope focused on to the sample surface at the same spot before and after shining the laser beam. To prevent this kind of damage, an optical intensity filter was used to reduce the laser intensity by a factor of 1,000. Although no more damage was observed after shinning the laser light, the intensity of the Raman data was observed to reduce with use of the optical filters. However, no information was lost due to the reduction of intensity rather it helped resolve various phonon modes in the scanned spectra.

Every peak observed in the acquired spectra was identified to a certain mode of vibration of atoms in the crystal. In our case, the peaks were observed at 112, 150, 180, 190 and 380 cm^{-1} corresponding to E_gSb, $A_{1g}Sb$, InSb transverse optical (TO), InSb longitudinal optical (LO) and InSb 2LO phonon modes, respectively.[88] The low energy phonon modes E_gSb and $A_{1g}Sb$ are observed in highly disordered crystals mostly due to elemental Sb vibrations indicating Sb antisite defects. The InSb TO modes indicate defects in the crystals which can be due to various reasons. The InSb LO modes are due to an ordering of the crystal indicating a good quality of the material. Presence of InSb 2LO modes indicate highly ordered crystalline material in all directions. Such a material is free from defects and highly desirable for an efficient device application. Most of the samples reported in this study observed to exhibit a convoluted/envelope of Raman shift peaks related to InSb LO and TO modes. As the peaks are separated only by ~10 cm^{-1}, numerical method like Lorentzian fitting was used to de-convolute the peaks. The ratio of peak intensities (I_{LO}/I_{TO}) was used as a parameter for comparison of defects and crystal quality amongst different heterostructures reported in this dissertation.

3.6.5 Absorption spectroscopy. To study the optical absorption property and estimate the band gap of the material, RT Fourier transform infrared (FTIR) spectroscopy was carried out using Agilent/Varian 670 FTIR Spectrometer. The sample was placed on a Harrick universal

transmission holder for a normal incidence to measure the optical transmission property. The normal incidence of the incoming light results in a Fabry Perot fringe interference in the acquired spectra due to change in refractive index and comparable epilayer thickness with the incoming light. Hence, InSbN heterostructures of different thicknesses were grown to reduce the effect of the fringe patterns in the acquired transmission spectra. Figure 3.4 shows FTIR RT transmission spectra of two InSbN heterostructures. The transmission spectrum of InSbN2 clearly shows the interference of fringe pattern, whereas InSbN1 shows a unique sharp absorption at λ cutoff ~9.3 μm.

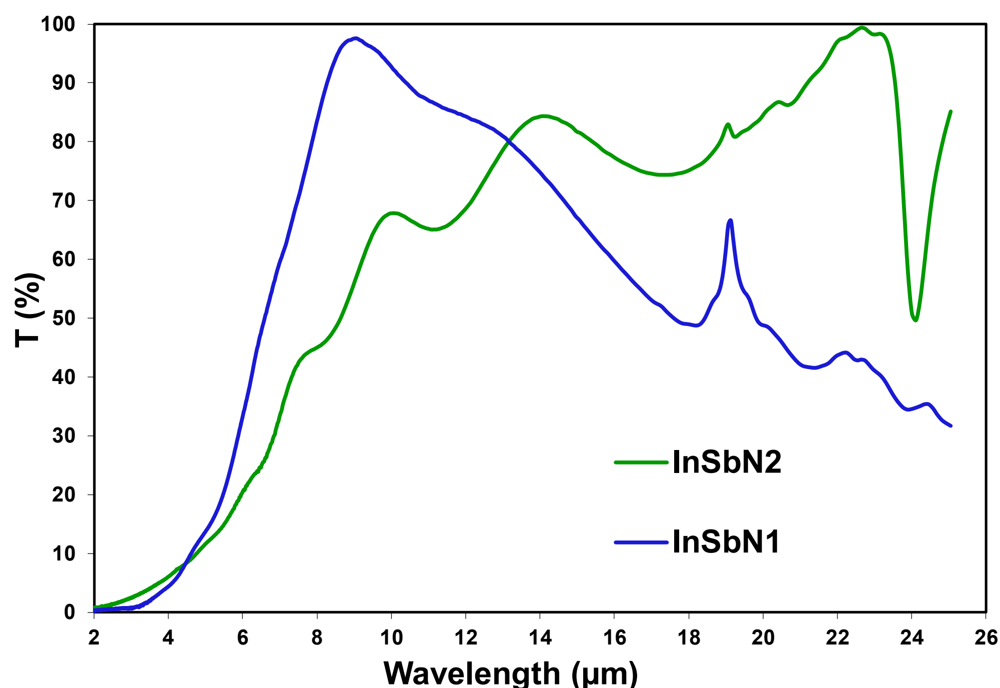

Figure 3.4. FTIR RT transmission spectrum of two InSbN heterostructures.

All the transmission spectra were obtained after subtracting GaAs substrate from the acquired data. This was done by acquiring a background scan using a GaAs substrate only in the path of the incidence beam. Consequent scan of all the spectra will be the resultant of InSbN on InSb. However, a trend of GaAs substrate spectra can still be observed beyond 16 μm. Hence,

for all the analytical purpose any absorption beyond 16 µm is neglected. Subtraction of GaAs substrate in this way increases the overall T (%) of the spectra. Further, use of a double sided polished GaAs substrate was observed to increase T (%) as compared to growth of the heterostructures on single sided polished GaAs substrates.

Figure 3.5 and Figure 3.6 compares the RT FTIR transmission spectra of InSb epilayer grown on single side and double side polished GaAs substrate, respectively. The noise observed in the acquired transmission spectra from the wavelength range 5.5 to 7.7 µm is due to strong absorption from water vapor present in the ambient atmosphere as depicted in Figure 1.2. This noise was observed to reduce after a strong purge of N_2 gas in the experimental setup enclosure. All the consequent data were acquired under such condition to obtain a noise free spectrum.

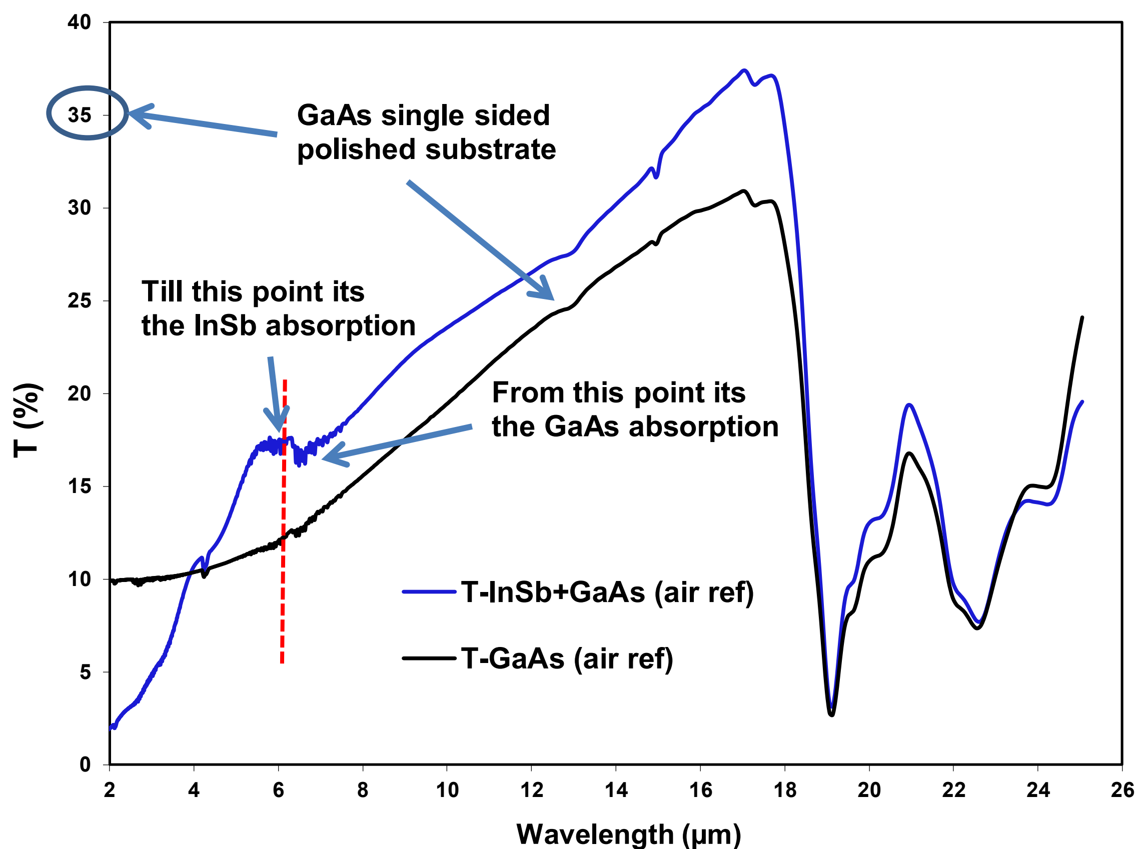

Figure 3.5. RT FTIR transmission spectra of InSb heterostructure grown on single sided polished GaAs substrate.

Figure 3.6 clearly shows that the InSb layer grown on double side polished GaAs substrate exhibits higher T (% values marked in circles in respective figures). Further, the double side polished GaAs substrate exhibits almost a constant transmission till ~16 µm distinctly indicating the behavior of the substrate beyond 16 µm. Even after subtracting the GaAs substrate from the InSb heterostructure spectra, the absorption feature of the substrate still visible beyond 16 µm. On an additional note, the T (%) is dependent on the thickness of the layer or the path length of incident beam. Hence, these acquired transmission spectra cannot be used for a quantitative comparison between various heterostructures as it is. Further, a broad edge in the transmission spectra makes it very difficult to determine the exact absorption edge or λ cut off.

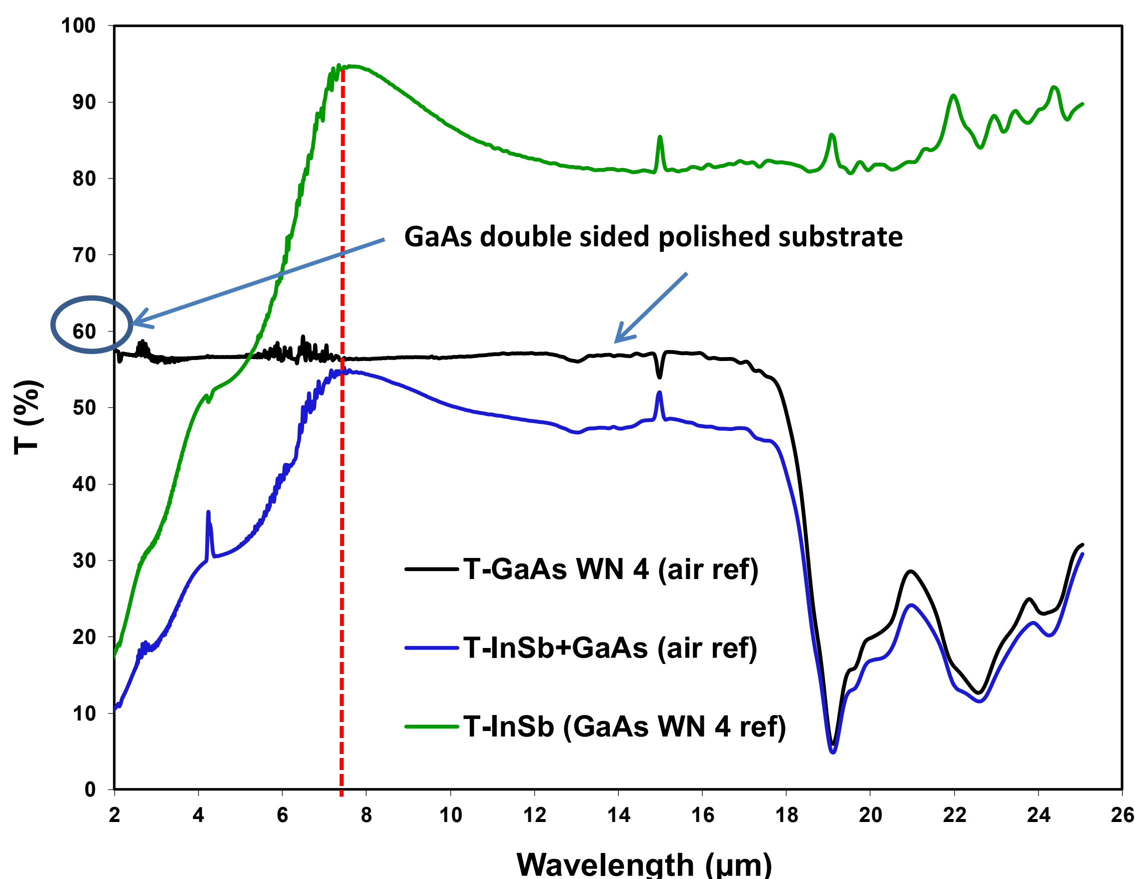

Figure 3.6. RT FTIR transmission spectra of InSb heterostructure grown on double sided polished GaAs substrate.

3.6.5.1 Optical absorption edge from FTIR. In addition to the above challenges there is further complexity due to the presence of various transitions in the absorption spectra of these nitride epilayers. These are (a) InSb band to band transition, followed by (b) transition to its localized band-tail states (also known as Urbach's tail), (c) InSbN band to band transition, followed by (d) its Urbach tail involving band to N-related defect transitions, and finally (e) the free carrier absorption. Since each of these transitions differ by only a few 10s of meV, the first derivative of the corresponding RT absorption coefficient (α) vs energy spectra (Figure 3.7) has been used to determine the absorption edge/optical band gap (E_o). This method is known to provide more accurate values for narrow band gap semiconductors, [113] and the absorption coefficient was calculated using

$$\alpha = \frac{1}{t_f} ln \frac{\mathbf{100}}{\boldsymbol{T}} \; cm^{-1} \tag{3.2}$$

where, α is the absorption coefficient of the epilayer, t_f the thickness of the epilayer (both epitaxially grown InSb buffer and InSbN combined) and T the % transmission measured by FTIR.

Figure 3.7 shows the RT absorption spectra of 1.2 µm InSbN/ 1.4 µm InSb/ GaAs and corresponding dα/dE to estimate the absorption edge. Each peak in the dα/dE plot corresponds to an absorption edge in the spectra. In this case, the peak at 0.178 eV corresponds to absorption due to InSb as it matches with its bulk RT band gap value. Although, the next two peaks correspond to InSbN absorption edge the sharp and periodic nature of the peaks can be due to the interference of Fabry Perot fringes as observed in the corresponding transmission spectra (Figure 3.4). However, the absorption edge for the InSbN layer in this specific heterostructure is within the range of 9 to 12.6 µm. Hence, dα/dE plot can also be used to distinguish the true absorption edge and the edge due to interference of fringe pattern from its periodicity.

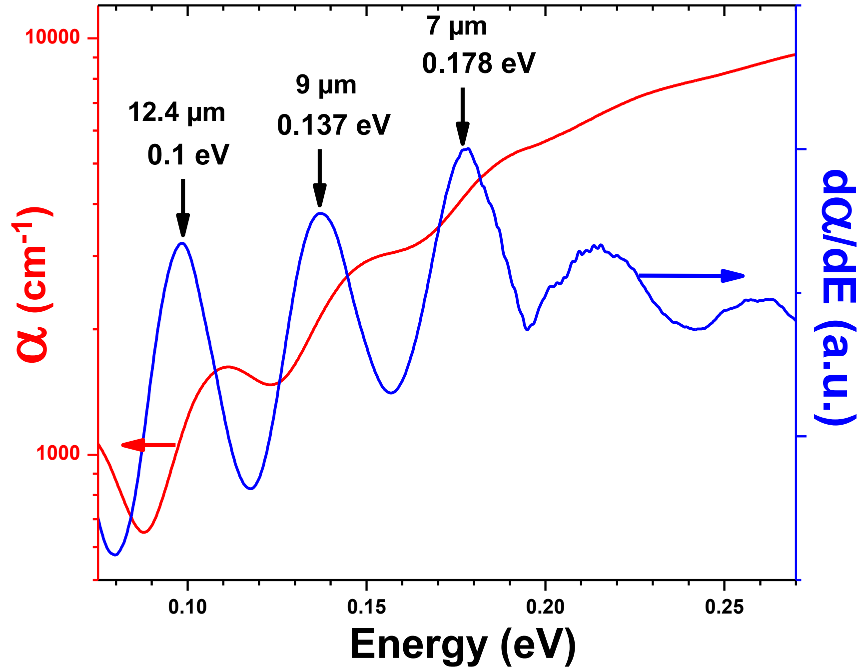

Figure 3.7. Estimation of optical absorption edge from FTIR absorption spectra.

3.6.5.2 Bandgap estimation using optical absorption edge. Once the optical absorption edge was determined from the absorption spectra, the bandgap was estimated using Equation 2.1. The energy shift due to Moss-Burstein effect is estimated by

$$E_{MB} = \left(\frac{1}{1+\frac{m_e}{m_h}}\right) \times 2kT \times ln\left(\frac{n}{\sqrt{N_C N_V}}\right) + 4kT \quad (3.3)$$

where, m_e is electron mass of InSb, m_h the hole mass of InSb, k the Boltzmann constant, T the temperature, N_C the effective conduction band density of InSb at T, N_V the effective valence band density of InSb at T and n the carrier concentration of the sample at T.[114] The band gap narrowing energy E_{BGN} is estimated by

$$E_{BGN} = An^{1/3} + Bn^{1/4} + Cn^{1/2} \quad (3.4)$$

where, n is the carrier concentration at above T, the coefficients A, B and C correspond to InSb material reported by Jain et al[115] are $1.22\text{x}10^{-8}$ eV/cm^{-1}, $1.09\text{x}10^{-7}$ eV/cm$^{-3/4}$ and $6.04\text{x}10^{-10}$ eV/cm$^{-3/2}$, respectively.

3.6.6 Hall measurements. The Hall measurement was carried out to study the electrical transport property of InSb and InSbN epilayers. Both RT and 77 K Hall data was measured using a HMS 2000 Hall measurement system at a constant magnetic field of 0.58 T. The variable field Hall measurement at RT was carried out using an in house constructed Hall system, where the magnetic field can be varied using an electromagnet from 0.03 T to 0.8 T. In both the cases, the sample with In dots in van der Paw configuration was loaded on a Lakeshore sample holder with gold plated spring contact connecting the In dots and the test probes.

3.6.7 AFM. The surface morphology was studied using Agilent Technologies 5600 LS Atomic Force Microscope. An automated tip mode was used to scan the test area with a minimum damage to the sample surface. A sampling area of 5x5 μm^2 was used to observe the surface roughness. After the data acquisition AFM analysis freeware tools such as SPIP was used to correct for any tilt/offset in the data. The surface roughness (R_{rms}) was estimated from the root mean square (rms) value of the intensities in the scanned data.

3.6.8 XPS. This technique allows the determination of the elemental composition, chemical state (bonding) and electronic state of the elements in the material. The XPS spectra are obtained by irradiating the test sample surface with a beam of x-rays while measuring the kinetic energy and number of electrons knocked off from the inner atomic shells at the same time. In this study the XPS spectra was acquired using Kratos Analytical Axis Ultra X-ray Photoelectron Spectrometer. The AXIS Ultra provides a high energy resolution capability for both conductive and insulating samples through the incorporation of the Kratos patented charge neutralization system. Incorporation of the patented spherical mirror analyzer in conjunction with the standard hemispherical system in the AXIS Ultra provides both high spatial resolution imaging and a real-time parallel detection facility that allows high quality chemical images in a few seconds.

A survey scan (Figure 3.8) was performed and recorded for every sample in order to obtain a clear C–C peak for calibration purpose. Each and every spectrum was calibrated using the C–C peak to a value of 284.5 eV. Thereafter a high resolution scan was performed for the region In 3d, Sb 3d and N 1s with a binding energy (BE) range 430-460 eV, 520-540 eV, and 390-410 eV, respectively.

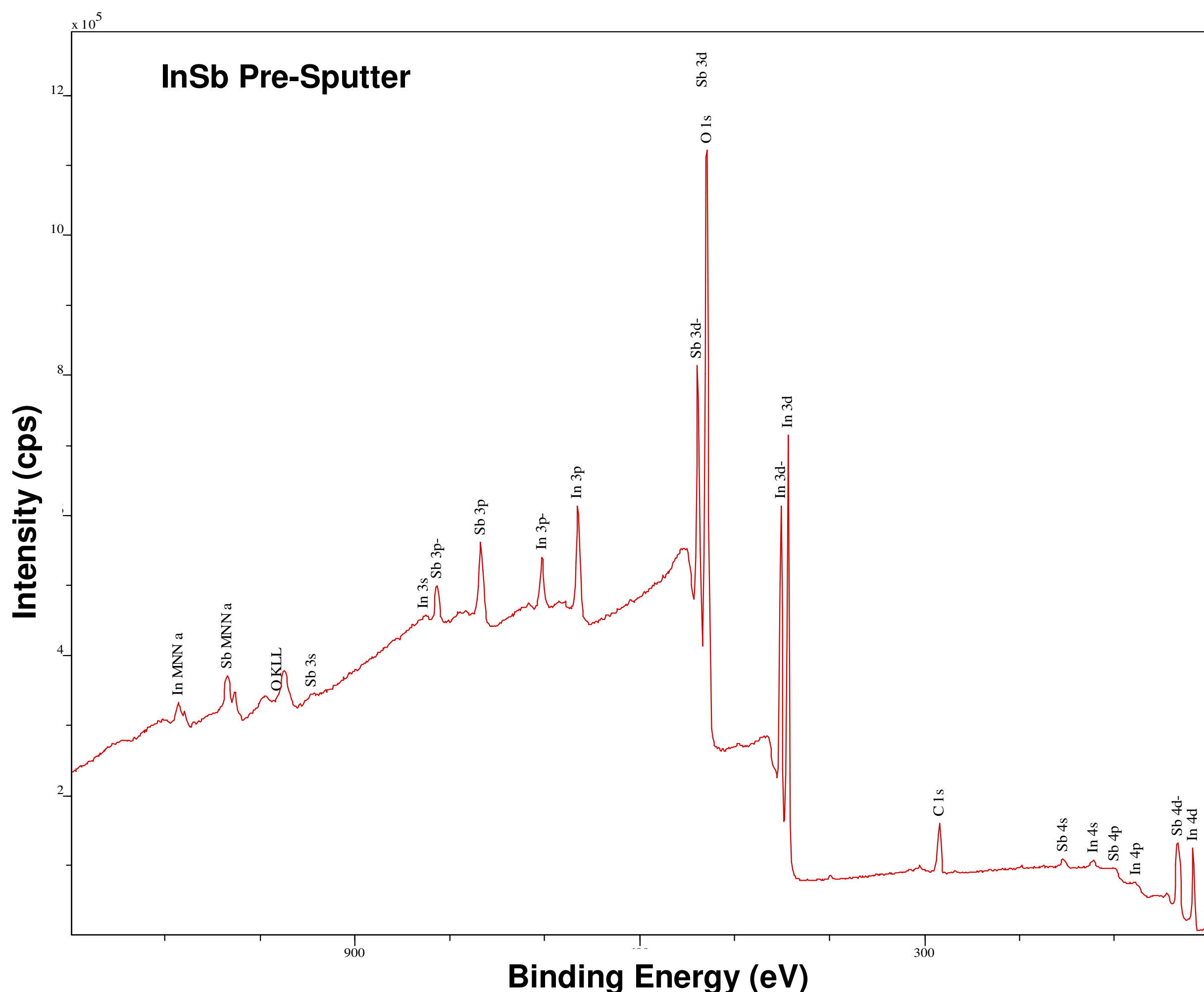

Figure 3.8. XPS survey scan spectra performed on the surface of InSb heterostructure.

After the data acquisition all the XPS spectra were processed and analyzed using a licensed version of Casa XPS software. A unique library file provided by the manufacturer of the instrument was used to take care of the sensitivity factor for every detected element. Each and every spectrum was calibrated using the C–C peak to a value of 284.5 eV. After the calibration,

every peak in the survey scan was assigned to a specific bonding type detected in the test sample to study the composition with the help of the in-built elemental library.

The surface oxide layer was removed by Ar ion sputter cleaning for 10 mins at an etch rate of 7 Å/min. Sputter cleaning of the surfaces resulted in the reduction in the intensity of C 1s peak, absence of oxides in In 3d and Sb 3d components. Before sputtering the In 3d and Sb 3d regions were observed to be dominated by In-oxides and Sb-oxides. Further, presputter survey scan (Figure 3.8) clearly shows O 1s peak obscured by the oxide component of the Sb $3d_{5/2}$ peak.

Figure 3.9 shows a typical InSbN XPS N 1s spectrum before and after sputter cleaning. The peaks seen on the sample before sputter cleaning were observed to be dominated by $-NH_2$ and N−O bondings. These are seen only before cleaning because of its formation due to surface to atmosphere interaction. After sputter cleaning the total nitrogen content decreased to some extent. And this is because of the removal of these atmospheric contaminations on the surface. Further, the intensity of In−N and Sb−N increased for N incorporation estimation/quantification. After sputter cleaning another survey was taken to compare the C−C peaks. The reduction in C−C peak at least by 50 % after sputter cleaning was considered as a benchmark to optimize the duration of sputtering.

In order to quantify various N− related bonding, XPS N 1s spectra were acquired at a high time constant from binding energies (BE) 390 to 410 eV with a resolution of 0.5 eV. Figure 3.9 shows the N1s spectra of a typical InSbN layer before and after sputter cleaning. The types of N− bonding were detected by deconvoluting the corresponding N 1s spectra. The spectrum was deconvoluted using a Shirley background mixed Voigt functions to get the information about the type and concentration of nitride bonding present in the epilayers. The area under the peaks at 396.4, 397.5, 399.7, 398.6 and 401.8 eV was used to quantify the percentage composition for

In−N, In−N−Sb, $-NH_2$, Sb−N, and N−O bonding, respectively.[91, 116] An increase in the ratio of the intensity of In–N peak to Sb–N at a depth of 70 Å indicated In-N being a dominant bonding mechanism during the growth of InSbN.

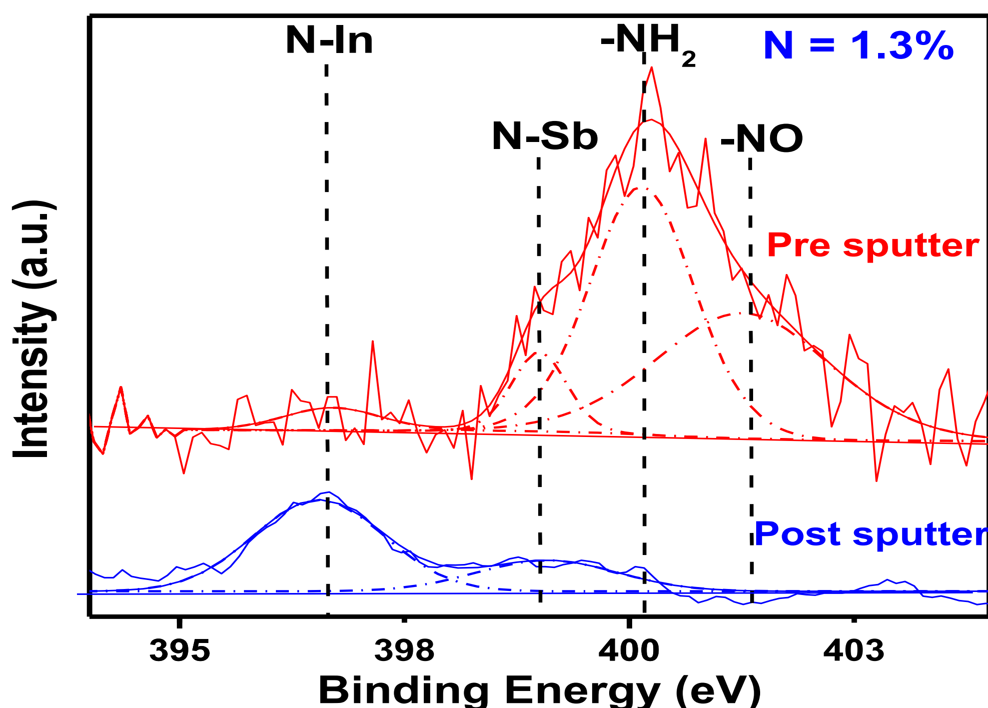

Figure 3.9. XPS N 1s spectra of InSbN sample pre and post sputter cleaning.

3.6.9 SIMS. The secondary ion mass spectroscopy was performed for a compositional depth profile of the grown heterostructures by Evans Analytical Group (EAG). To quantify the N content an ion implanted N in InSb substrate at a dose of $6x10^{15}/cm^2$ was used as the reference layer for calibrating the N content in InSbN. Figure 3.10 shows a typical SIMS depth profile of group III (In, Ga) and group V (Sb, N, As) atom fractions for a 0.4 µm InSbN/ 1.4 µm InSb/ GaAs heterostructure. Since it is a destructive technique the gradual roughening for the sample during the measurement observed to cause a broadening of the profile. Notably, this technique helped estimate the total N content in the heterostructures without distinguishing the substitutional and interstitial nature of N.

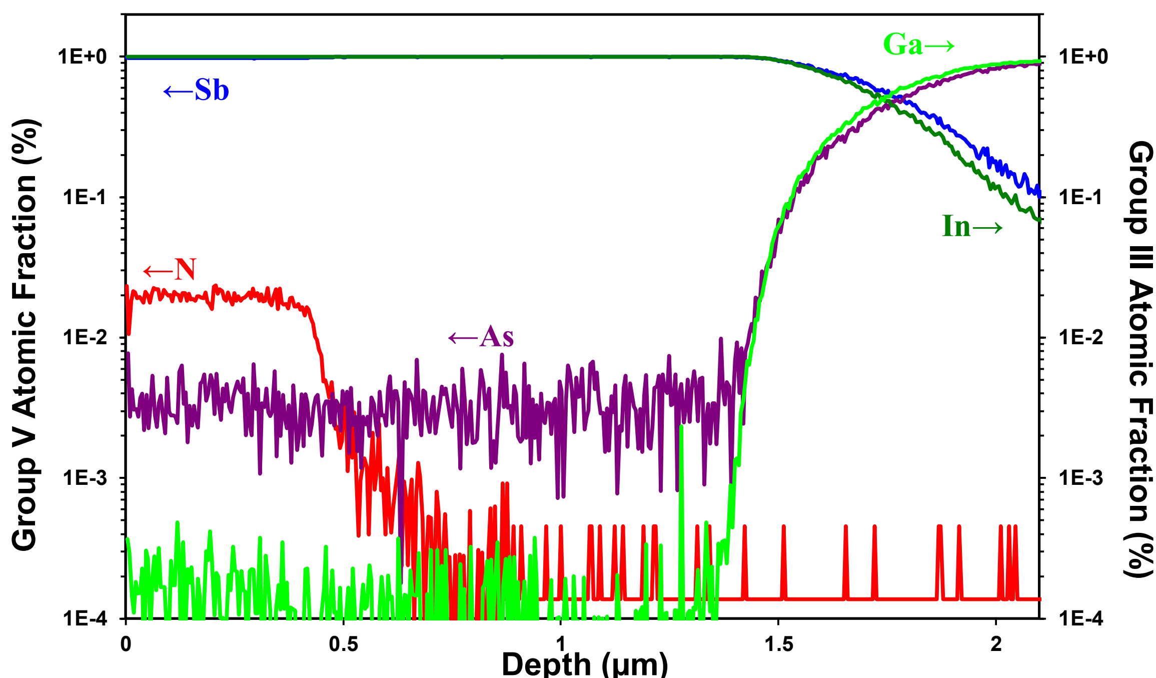

Figure 3.10. SIMS depth profile of 0.4 µm InSbN/ 1.4 µm InSb/GaAs heterostructure.

3.6.10 NRA. The nuclear reaction analysis (NRA) for Rutherford backscattering spectroscopy (RBS) was carried out by Evans Analytical Group to determine the interstitial/ substitutional N content in a specific InSbN heterostructure. A set of RBS (He++, 2.275 MeV) spectra were acquired in the random and channeled mode.

Ion channeling is an application of RBS in which the absence of backscattering signal is quantified. A crystalline sample consists of regularly spaced and repeating atomic structures. In the macroscopic sense, it is possible to 'see' through the entire crystal structure at a specific sample orientation. In an ion backscattering application, alignment of the incident beam with a major crystallographic axis allows the incident ions to be "channeled" down, all the way through the open regions of the crystal lattice. The probing ions are then "steered" down the rows of atoms, resulting in a reduction in backscattering yield with the minimum backscattering when the sample is optimally channeled. For a channeled orientation, the incident ions can be transported to very great depths (>3-5 µm) from which backscattering events cannot be detected. For

example, in crystal Si there are many sample orientations that will allow channeling to be observed. Varying degrees of channeling will result in an increase of detectable backscattering events. Thus, the degree of ion channeling can be quantified. If the crystal lattice contains a certain matrix or impurity atoms which are not at the crystal lattice structure that is at the interstitial positions, backscattering events can quantify the concentration of interstitial atoms (in units of atoms/cm^2). Thus, extent of damage from ion implantation, degree of crystal regrowth upon annealing, and the degree of impurity substitutional/interstitial can all be quantified in an ion channeling method.

Channeled and rotating random RBS spectra were acquired at detector angles of 160° and 105° from the forward trajectory of the incident He ion beam. Figure 3.11 compares both channeled and random NRA RBS spectra for InSbN heterostructure grown at 290 °C. The 101° grazing angle data provides improved depth resolution, while the 160° normal angle data allows a depth of up to 1 μm for the measurement. Table 3.1 lists the X calculated from the random and channeled intensities of the InSb layer and the N signals from the NRA. These are used to calculate the substitutional N concentration in the layer.

The percentage of N atoms in the substitutional position is calculated by:

$$S\,\% = \left(1 - \left(\frac{X_N - X_{matrix}}{1 - X_{matrix}}\right)\right) \times 100 \quad (3.5)$$

The N NRA signal from the sample was observed to be small. The sum of several transitions was used to calculate the X values. C and O were also observed in the NRA spectra. Some error may be introduced in the N calculation with this approach as the N is integrated over a deeper region than the X of the matrix signal. It is to be noted that, as the de-channeling increases with depth, the substitution estimated is a minimum value, and the actual amount of substitutional in the lattice is estimated to be higher.

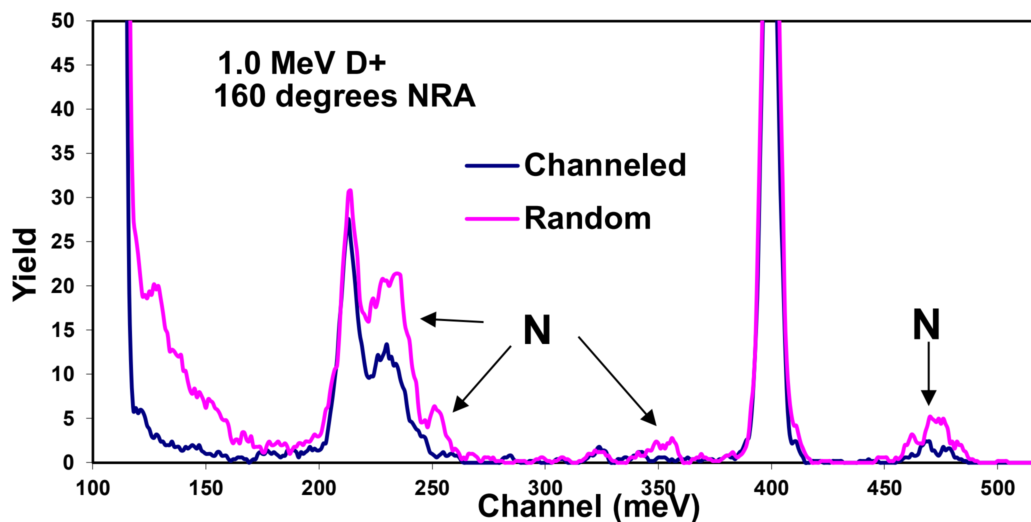

Figure 3.11. NRA Rutherford backscattered spectra of InSbN heterostructure grown at 290 °C.

Table 3.1

NRA measured channeling parameters

Sample	Element	X (channeled/random)	% Substitution
InSbN	N	0.34	85.7
InSbN	Matrix	0.23	--

3.7 Conclusion

MBE growth technique was used for the growth of InSb and InSbN on GaAs, due to its ability to precisely control the thermodynamic condition to favor the kinetics of high quality mismatched alloy growth. The adapted step wise MBE growth of InSb and InSbN epilayers on GaAs substrates were presented. Both post growth *ex-situ* and *in-situ* annealing optimized for InSbN epilayers were discussed. To understand the structural, compositional, electrical and optical property of the MBE grown InSbNheterostructures, various *in-situ* and *ex-situ* semiconductor characterization techniques, their principles, and the methodologies used have been reported in this Chapter.

CHAPTER 4

Growth and Characterization of InSb Epilayers Grown on GaAs (001) Substrates

4.1 Introduction

The growth of high quality InSb on GaAs substrates has been studied extensively and well understood. InSb is highly lattice-mismatched with respect to GaAs. Hence the growth parameters such as Sb/In flux and growth temperature play an important role in mitigating the defect due to the heterojunction. Many research works have been published[30, 44, 52-56, 58-60, 117, 118] explaining various growth techniques for the growth of high quality InSb epilayers.

In this chapter we present the optimization of all the essential MBE growth parameters Sb/In flux ratio, growth temperature and epilayer thickness to achieve a high quality InSb buffer layer on GaAs substrate. The growth of InSb epilayers on GaAs substrate was performed as outlined in Section 3.3 Growth of InSb on GaAs. The Sb/In flux ratio exceeding unity is reported to yield good quality InSb epilayers grown at the temperatures 380~400 °C. Since it is very difficult to measure the individual flux values a correlation of flux ratio need to be done with the measured BEP values using the RHEED patterns.

The RHEED patterns reported to change dynamically during the growth depending on the growth front being Sb rich or In rich at certain growth condition. Hence, by observing specific RHEED patterns the Sb/In flux ratio can be estimated and by recording the BEP values at growth condition the values can be calibrated. The details of the calibration process will be discussed in this chapter. A brief study of the defects is presented. The calibration of Sb/In BEP ratio using the dynamic RHEED pattern is suggested for a reproducible MBE growth of high quality InSb buffer layer. These results were also used for the subsequent growth of InSbN epilayers. Some of the results and discussion in this Chapter have been peer reviewed and published.[30]

4.2 Sb/In BEP Ratio and Growth Temperature Optimization

Dynamic RHEED observations were used for the optimization of Sb/In flux (will be referred to as BEP) ratio and InSb growth temperature for this study. A typical growth of an InSb epilayer on GaAs, begins with a spotty RHEED corresponding to 3D growth, which transforms to a bright and streaky 2D RHEED pattern after the growth of a few monolayers. Figure 4.1 (a) to (i) shows the sequence of RHEED patterns with an interval of 0.35 sec starting from the inception of the growth of InSb droplets to epilayer on a GaAs surface along (110) azimuth. Figure 4.1 (a) is a x2 pattern from the GaAs buffer surface. Figure 4.1 (b) shows the appearance of spots on the streaks instantly after opening the In shutter, indicating the formation of InSb islands. Following RHEED patterns Figure 4.1 (c) to (h) show the gradual disappearance of the GaAs x2 pattern and set of the spots transforming to streaks indicating the 3D InSb growing into an epitaxial layer (2D). Finally, Figure 4.1 (i) shows the streaky x1 pattern of InSb epilayer

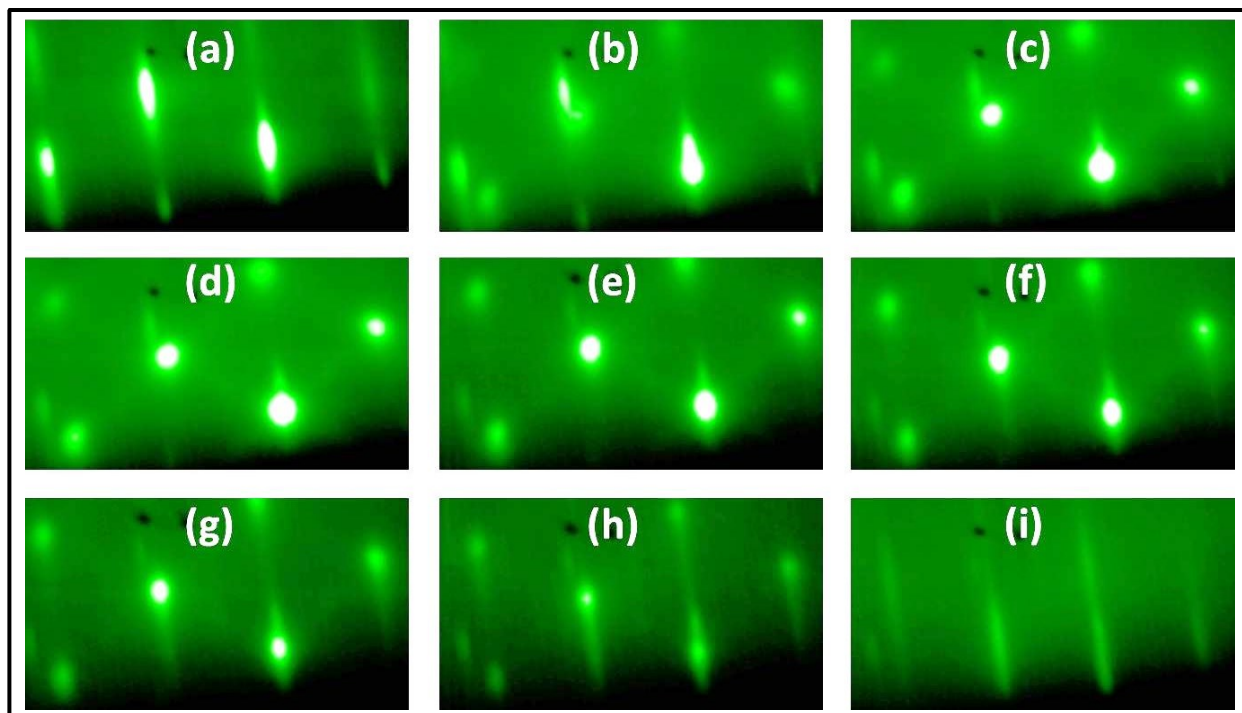

Figure 4.1. Sequence of RHEED patterns observed during growth of InSb on GaAs buffer along (110) azimuth.

~3 sec after opening the In shutter. This transition of growth pattern from 3D to 2D within a few seconds indicates the growth of 100 % relaxed InSb layer within a few monolayers, due to the large lattice mismatch between the two material systems.

A flux-temperature calibration was performed for the growth of InSb layer by varying Sb flux at a fixed In flux and growth temperature followed by varying the growth temperature for a given flux ratio to obtain at least four distinct RHEED patterns as indicated in Figure 2.1. Figure 4.2 shows the RHEED patterns on epitaxial InSb grown on (001) surface of GaAs (a) $(1\bar{1}0)$ azimuth showing a combination of pseudo x3 and x4 pattern, (b) $(1\bar{1}0)$ azimuth showing pseudo x3 pattern, (c) and (d) (110) azimuth showing a combination of x2 and x4 patterns. It is believed that for an Sb-rich InSb growth, the surface reconstruction is either a *pseudo*(1x3) (Figure 4.2 (b)) or a *c*(4x4) RHEED pattern, also referred to as $(2\sqrt{2}x2\sqrt{2})$-45°, depending on the growth temperature being above or below a certain transition temperature, T_C.[51, 117] In our case, for an

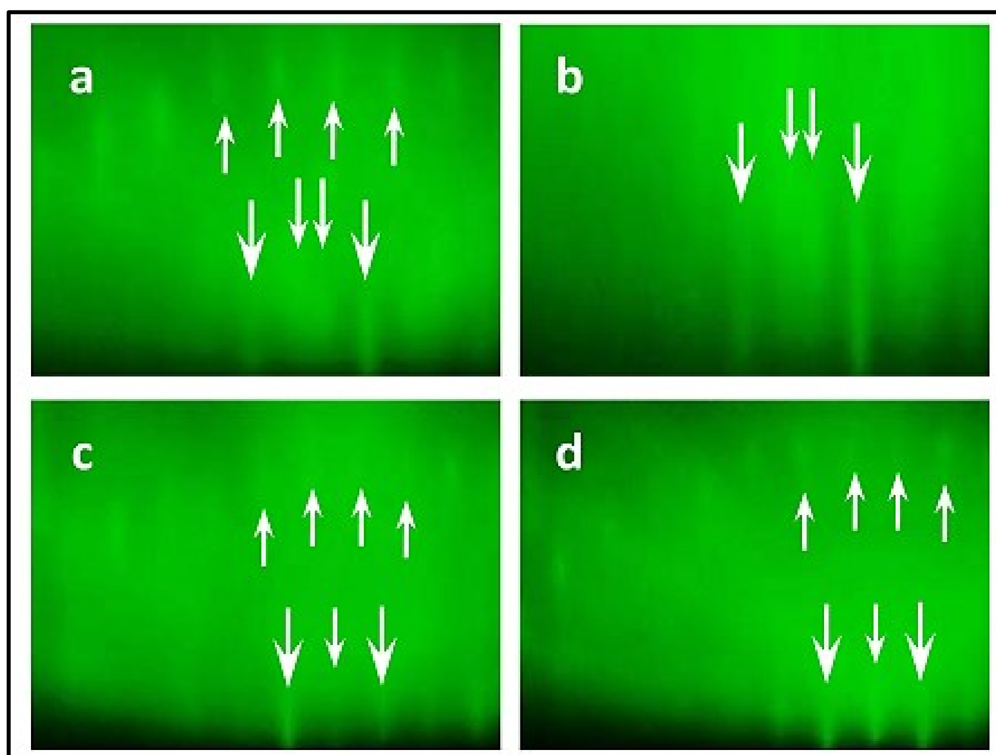

Figure 4.2. RHEED patterns on epitaxial InSb grown on (001) surface of GaAs.[30]

Sb:In BEP ratio of 3.3, this transition temperature T_C was observed to be ~ 400 °C which was recorded when a RHEED pattern Figure 4.2 (a) was observed. The growth temperature was calibrated using this RHEED transition each time, for a given Sb/In BEP ratio. We found that the growth of an InSb buffer layer slightly below T_C at $T_C - 10$ °C with a *c*(4x4) RHEED surface reconstruction resulted in reproducible good quality InSb epitaxial layers with low FWHM in their corresponding HRXRD scans.

4.3 Results and Discussion

Figure 4.3 shows the (004) HRXRD spectra of 0.6 µm InSb epilayer grown at 370 °C with two unique peaks at 66.05° and 56.8° corresponding to 2θ of GaAs substrate and InSb epilayer, respectively. The observed 2θ value for the InSb layer indicates a bulk like behavior, attesting to the RHEED observation for a 100 % relaxed layer. The FWHM values for GaAs substrate and InSb epilayer were observed to be 40 and 220 arcsec, respectively. The FWHM values observed for the InSb layers are comparable with the values reported by Debnath et al[119] 250±30 arcsec for the layer thickness of 1±0.2 µm grown under similar growth conditions.

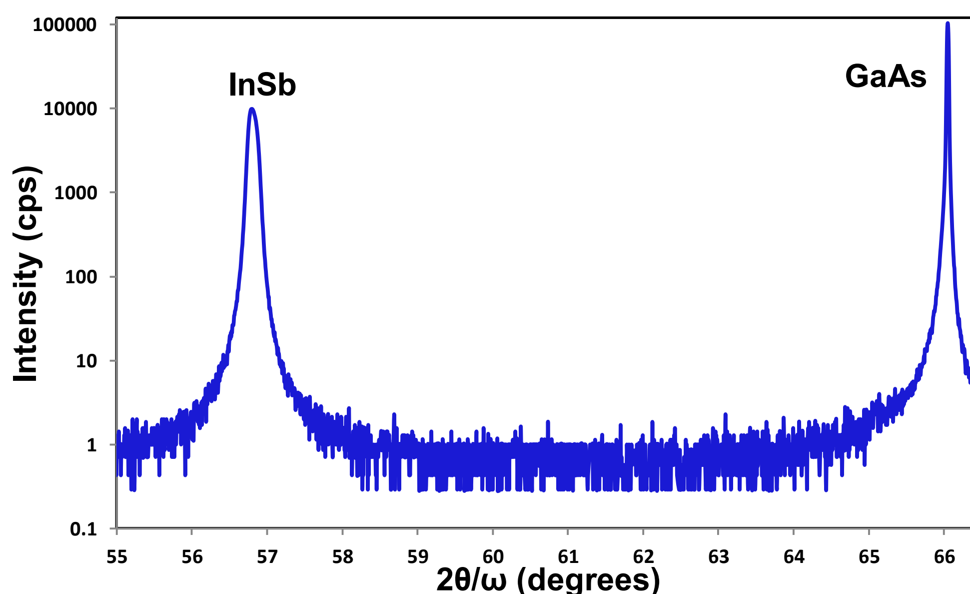

Figure 4.3. (004) HRXRD scan of 0.6 µm InSb epilayer grown on GaAs substrate.

Figure 4.4 shows the reduction in HRXRD FWHM of 1.4 μm InSb epilayers grown on GaAs substrates at growth temperature of 390±10 °C as a function of Sb/In BEP ratio. The reduction in the XRD FWHM indicates an improvement in the quality of the epilayer with an increase in Sb/In BEP ratio (and hence flux ratio). Further, the reproducible nature of XRD FWHM for Sb/In BEP ratio of 3.3 was considered to be an optimized growth condition and was used for all the consequent growths.

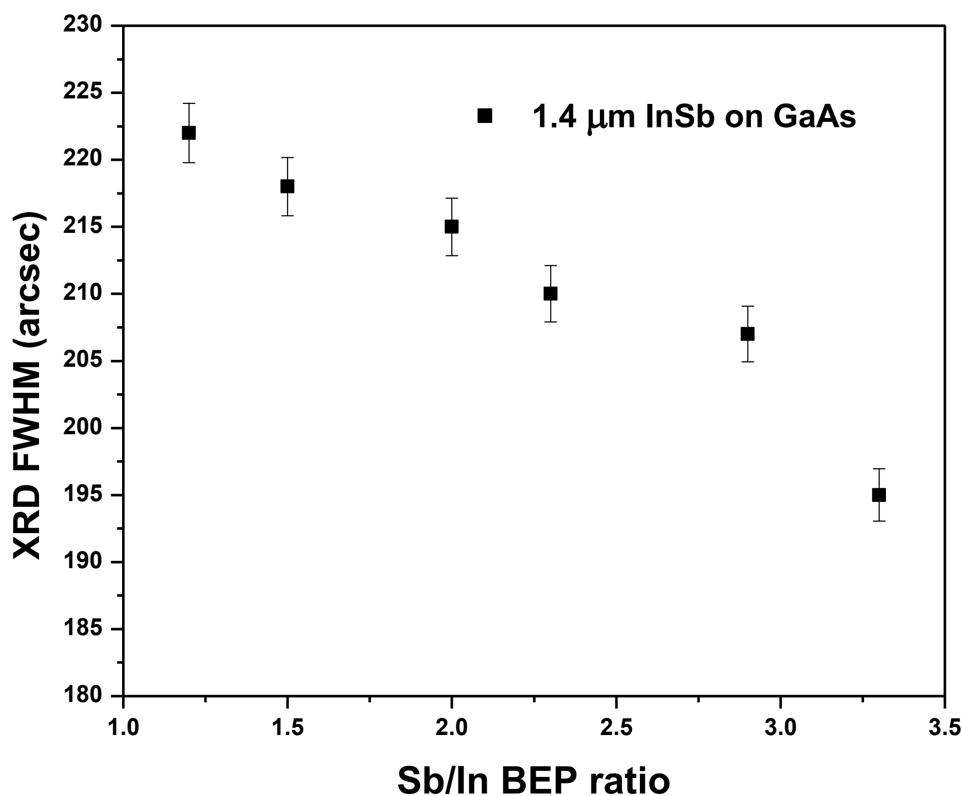

Figure 4.4. InSb grown on GaAs Sb/In BEP ratio vs HRXRD FWHM.

Figure 4.5 compares the RT micro-Raman spectra of InSb epilayers grown at two different temperatures with same Sb/In BEP ratios of 3.3. The spectrum marked by InSb old was grown at a relatively lower temperature $T_C - 40$ °C, whereas InSb new was grown at T_C. It can clearly be seen that the sample grown at low growth temperature exhibit very high E_gSb and $A_{1g}Sb$ peak indicating presence of Sb antisites. In addition, this creates disorder in the crystal

lattice which is characterized by presence of forbidden InSb TO mode. Whereas, the InSb epilayer grown at T_C exhibits InSb 2LO mode indicative of the high crystalline quality of the layer. Hence this growth temperature was considered as an optimized growth temperature. The difference in the crystalline structures observed in the micro-Raman spectra are also reflected in the corresponding differences noted in the electrical properties of these two InSb heterostructures.

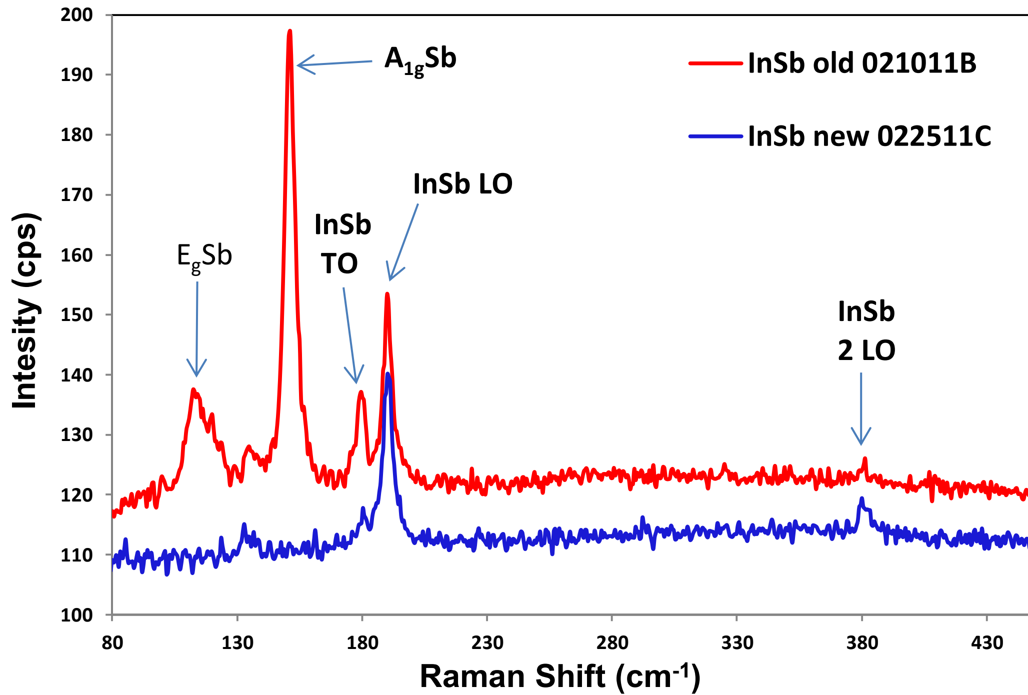

Figure 4.5. RT micro-Raman spectra comparison of 1.4 µm InSb grown at different growth conditions.

The RT *n* for InSb old and new was measured to be 7×10^{16} and 2×10^{16} cm^{-3}, respectively. The high *n* observed in case of the InSb old 021011B heterostructure is clearly due to the donor nature of Sb present in the form of Sb antisites. Further, the RT μ for InSb old and new were observed to be 29,000 and 45,000 cm^2/Vs, respectively. A relatively low mobility observed for the InSb old can be correlated to the defects in the crystal attesting to the InSb TO modes

observed in the corresponding Raman spectra (Figure 4.5). These Hall μ values were observed to be in the range of values reported in the literature[119, 120] for similar epilayer thickness. The dislocation density (D) was estimated (Section 3.6.2.2) to be in the order of ~10^8 cm^{-2} for the optimized InSb layers.

Figure 4.6 shows the SIMS depth profile of 0.6 µm InSb/GaAs heterostructure grown under optimized InSb growth condition. Almost an abrupt junction can be seen between the InSb epilayer and the GaAs substrate. Further, a matching atomic fraction of group V (Sb) and group III (In) along the depth of InSb epilayer indicates a perfect stoichiometric condition during the growth of InSb epilayer. In addition to that, no excess Sb in the SIMS profile attests to the absence of A_{1g}Sb and E_gSb peaks in the Raman spectra of the optimized InSb epilayer.

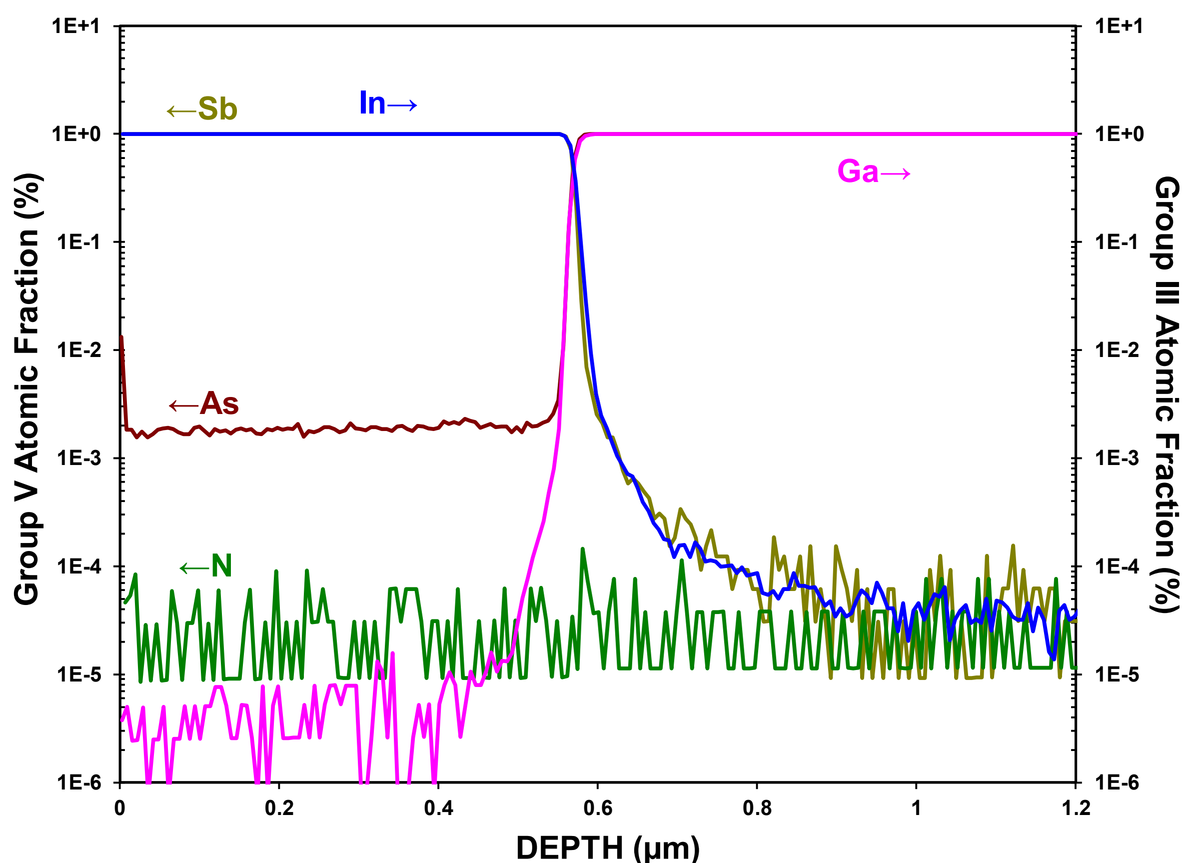

Figure 4.6. SIMS depth profile of 0.6 µm InSb/GaAs heterostructure.

Figure 4.7 (a) shows the Nomarski optical image of a typical surface of InSb grown under relatively lower Sb:In BEP ratio of 1.5. The surface was observed to be rough, most probably due to a loss of Sb. A relatively smooth surface was observed after increasing the Sb:In BEP ratio to 3 and higher (Figure 4.7 (b)). This indicates a high Sb/In BEP ratio during the growth of InSb epilayers helps smoothen the surface due to availability of Sb in excess for bonding with all the available In to form InSb. However, there is a limit to which Sb BEP can be increased. A very high Sb BEP can also result in Sb antisites which can eventually increase the surface roughness.

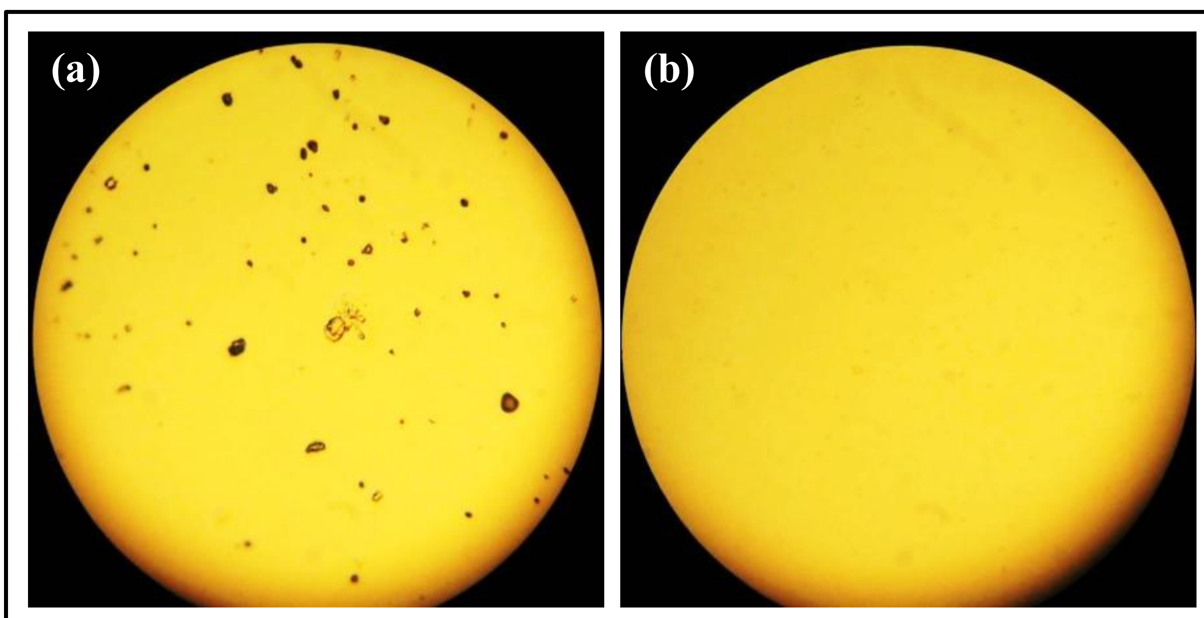

Figure 4.7. The Nomarski optical microscope image of InSb grown at 380 °C on GaAs substrate under Sb:In BEP ratio of (a) 1.5 and (b) 3.3.

Figure 4.8 shows the best AFM surface roughness of R_{rms} ~ 0.28 nm in case of 0.6 µm InSb grown at T_C. The surface roughness R_{rms} was observed to be in the range of 4±2 nm for most of the *as-grown* InSb heterostructures. A reduction in the R_{rms} observed up to 2 nm with an increase in epilayer thickness. However, some exceptionally rough surface up to R_{rms} ~ 5.8 nm in case of 1.4 µm thick InSb suggest no systematic dependency on the epilayer thickness.

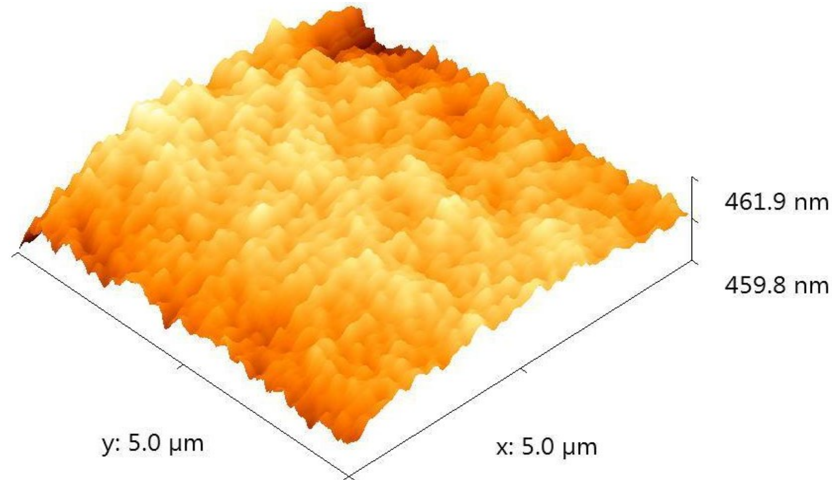

Figure 4.8. AFM surface image of InSb grown at T_C with best surface roughness of 0.28 nm.

4.4 Conclusion

In conclusion, the MBE growth parameters (Sb/In BEP ratio and growth temperature) for InSb were optimized using the dynamic RHEED reconstruction patterns. Highly crystalline InSb heterostructures were grown on GaAs with optimized Sb/In BEP ratio of 3.3 at a growth temperature of 400 °C. The growth of InSb at the transition temperature T_C is critical for a good crystalline InSb epilayer. Further, growth at temperatures below T_C can result in Sb antisites which in turn increase the background n and reduce μ due to defects. It was reported that the calibration of T_C at a given Sb/In BEP ratio using the dynamic RHEED observation results in a reproducible growth, as it approaches its stoichiometric condition.

CHAPTER 5

Growth and Characterization of InSbN Heterostructures on GaAs (001) Substrates

5.1 Introduction

Incorporation of N beyond a couple of % in group III-V alloys is very well known[30] to be a challenge due to the large miscibility gap, N centers[121] that it produces and incorporation of N in the interstitial sites. The MBE growth technique allows growth under non-equilibrium conditions, hence epilayers can be grown in the miscibility gap and is ideally suited for the growth of dilute nitride epilayers where the miscibility gap extends almost in the entire composition rang. The MBE growth conditions play a very important role in order to get the suitable epitaxial layers for a detector. In the literature,[21, 83, 88] low growth temperatures (~330 °C) and low rf N plasma power (~200 W) were reported to be favorable for high N incorporation. Hence we used these growth conditions for our initial attempts of InSbN growth. However, with increase in N BEP beyond $1x10^{-7}$ Torr the growth of InSbN was observed to be unstable from the RHEED pattern transition from streaks to spots indicating a non 2D growth. In order to study the effect of N incorporation with variation of N BEP, a more stable growth condition at a higher growth temperature of 380 °C was selected. The optimized growth parameters for the high quality InSbN epilayer were thereafter established by carrying out a systematic and detailed study of the growth by varying each of the growth parameters one at a time and correlating its effect on the structural, electrical and optical properties of the InSbN layers.

5.2 Experimental Details

After the growth of highly crystalline 1.4 µm thick InSb buffer, the InSbN epilayers were subsequently grown as per the steps outlined in section 3.4. InSbN heterostructures were grown

at 380 °C with varying N plasma BEP: 1, 1.5, and 1.7 ($x10^{-7}$ Torr) and are identified as N1, N2 and N3 respectively. This set of InSbN heterostructures were used to study the effect of N incorporation with variation in N BEP.

To study the effect of N incorporation with variation in growth temperature, InSbN heterostructures were grown at fixed N plasma BEP of $1x10^{-7}$ Torr with different growth temperatures of 290, 330 and 380 °C, which are represented by T1, T2 and T3, respectively. All the InSbN epilayers were 1.2±0.2 µm thick grown at a growth rate 0.4 µm/hr. More than 10 % error in the thickness values has been accounted for a change in growth rate with change in growth temperature at a fixed Sb/In BEP ratio. The Sb/In BEP ratio was maintained at 3 throughout the nitride layer growth.

5.3 Results and Discussion

The RHEED patterns observed during the growth of InSbN were used as one of the main factors to understand and control the stability of growth condition during the growth process. Figure 5.1 (a) and (b) shows the RHEED recombination *c*(1x4) which was observed during the growth of InSbN under Sb/In BEP ratio < 1 whereas (c) and (d) shows the pattern *c*(1x3) for

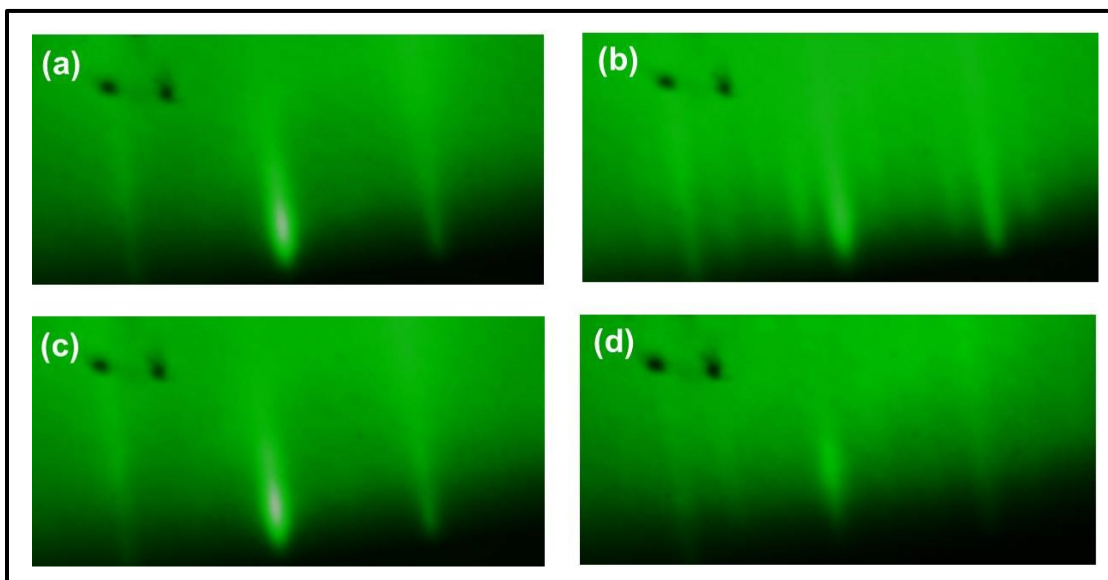

Figure 5.1. RHEED patterns observed during the growth of InSbN epilayers.

Sb/In BEP ratio >1 both grown at 330 °C and N BEP $1x10^{-7}$ Torr. The transition of pattern x4 (Figure 5.1 (b)) to x3 (Figure 5.1 (d)) with increase in Sb BEP (keeping In BEP constant) was used to obtain a stoichiometric condition for the growth of InSbN. These streaky RHEED patterns clearly indicate a 2D growth and hence a highly favorable growth condition for InSbN epilayers.

At a relatively lower growth temperatures of 290 ~ 330 °C and Sb/In BEP ratio >1 the 2D growth of InSbN was observed to be unfavorable for N BEP higher than $2x10^{-7}$ Torr. Figure 5.2 (a) shows the combination of streaks and spots on x1 pattern observed during the above growth condition, indicating roughening of the growth front due to an unfavorable thermodynamic condition for InSbN layer growth. Further continuation of such a growth observed to result in spotty RHEED pattern as shown in Figure 5.2 (b), indicating a 3D growth and hence a highly unfavorable condition for good quality InSbN layer growth.

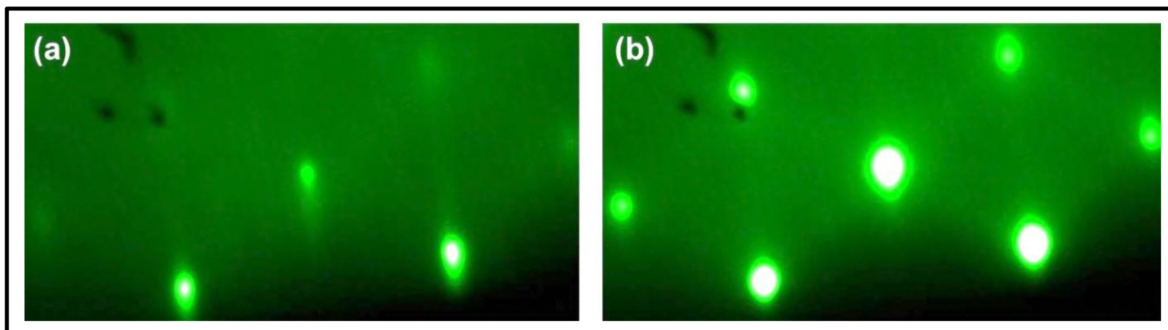

Figure 5.2. A combination of spots and streaks in the RHEED pattern observed during InSbN growth.

5.3.1 N BEP variation. The growth of InSbN (N1, N2 and N3) was observed to be under a RHEED pattern of *c*(1x3) (as shown in Figure 5.1 (c) and (d)) indicating an Sb rich growth as per the selected growth condition for Sb/In flux ratio higher than unity. A periodic observation of the RHEED pattern indicated a constant 2D growth throughout in case of the epilayers N1 and N2. In case of N3 a combination of streaks and spots in the RHEED pattern (similar to Figure 5.2

(a)) were observed after 90 minutes of growth, indicating a rough growth front. This could be due to an unstable growth condition for InSbN epilayer with a very high N plasma flux at the given growth temperature and chosen Sb/In BEP ratio.

Figure 5.3 shows the (004) HRXRD spectra of InSbN epilayers grown under varying N plasma BEP at a constant growth temperature of 380 °C. The main peak at 0 arcsec corresponds to the InSb epilayer with 2θ at 56.8°. The FWHM values for N1, N2 and N3 were observed to be 190, 216 and 246 arcsec, respectively. This indicates N1 exhibits a better structural quality of the nitride epilayer as compared to N2 and N3. A high FWHM observed in case of N3 is due to a shoulder on the right of the InSb peak. The shoulder seen for N3 indicates degradation in the quality of the layers, which can be correlated to the combination of spotty and streaky RHEED observed during the growth. However, this shoulder also could be due to an N incorporation of 0.7 % estimated from the simulation of XRHRD data. Whereas, in case of N1 and N2 the N incorporation is believed to be below 0.5 % because any N incorporation less than 0.5 % could get enveloped by the broad profile of InSb peak.

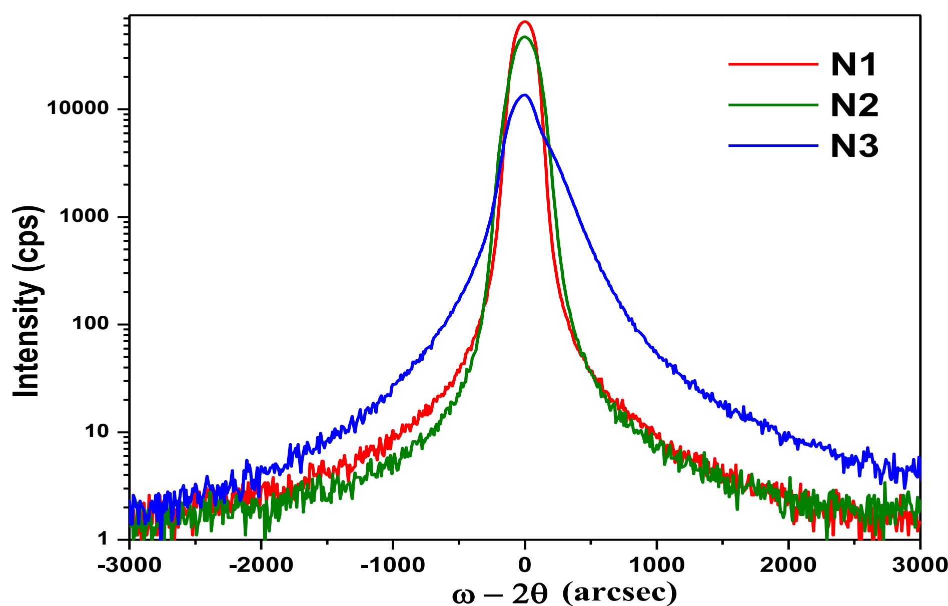

Figure 5.3. HRXRD (004) scan of InSbN epilayers grown under different N BEP at Ts 380 °C.

Figure 5.4 shows the RT micro-Raman spectra for nitride epilayers N1, N2 and N3. The TO phonon was observed to increase with increase in N BEP, indicating degradation in the crystal structure due to increase in N incorporation. A low energy peak observed at 150 cm^{-1} in the case of N2, identified as A_{1g}Sb, is due to Sb–Sb antisite defects. The presence of A_{1g}Sb modes and variation in I_{LO}/I_{TO} with N BEP variation indicate that the selection of right N BEP for nitride epilayer growth is critical for a given Sb/In BEP ratio and growth temperature. In addition to that, InSb 2LO mode observed only for N1 indicates highly crystalline quality attest to the best FWHM observed in the corresponding HRXRD plot as compared to N2 and N3.

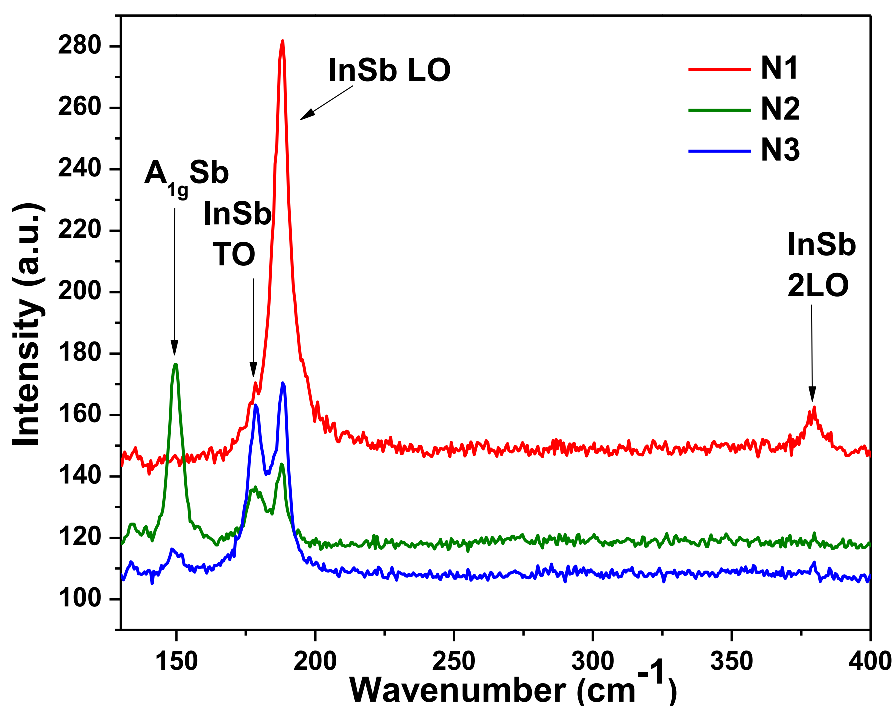

Figure 5.4. RT micro-Raman spectra of InSbN heterostructures grown under different N BEP at Ts 380 °C.

These observations clearly suggest two important points. First, it is clear from the micro-Raman spectra (Figure 5.4) that, there is an increase in the InSb LO mode with an increase in the N BEP. As N BEP, the only growth parameter varied during the growth of InSbN layer in these

heterostructures, the degradation in the epilayers can be attributed to the variation in N incorporation. This also drives home the second important point, the N incorporation in InSbN can be increased with increase in N BEP at a constant growth temperature and Sb/In flux ratio. Hence, one has to trade between the crystalline quality and the amount of N incorporation in InSbN epilayers. The surface morphology studies as shown in Figure 5.5 and tabulated in Table 5.1 indicate no significant change in surface roughness with either increase in growth temperature or increase in N BEP. The high R_{rms} observed for N3, was due to the combination of 2D and 3D growth evident from the mixed streaky and spotty RHEED pattern during the growth. This also correlates with the high FWHM observed in the corresponding HRXRD peak.

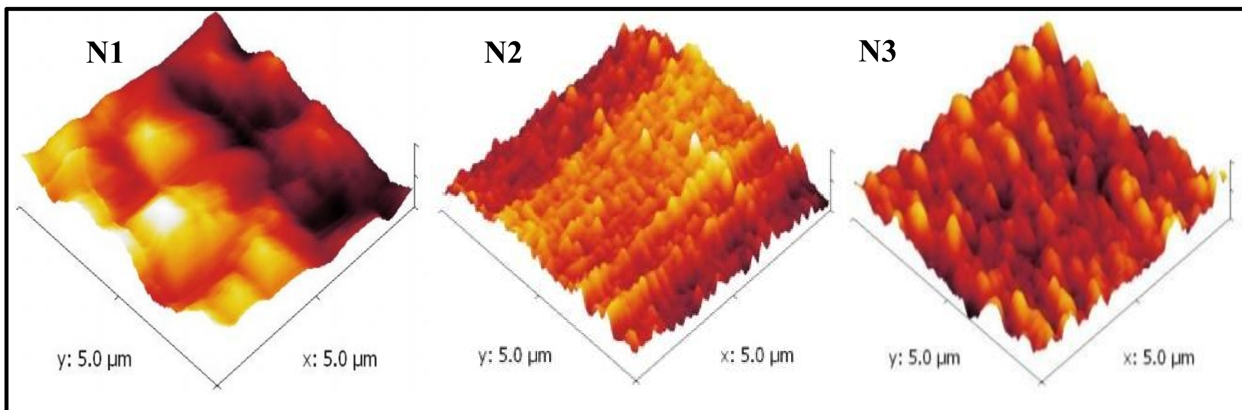

Figure 5.5. AFM images of InSbN epilayers grown under different growth conditions.

Table 5.1

Comparison of AFM measured R_{rms} *and Hall data of InSbN epilayers grown at different N BEP.*

InSbN heterostructure	AFM RMS (nm)	n_{RT} (cm^{-3})	μ_{RT} (cm^2/Vs)
N1	6	1.1×10^{17}	46,500
N2	5	2.6×10^{18}	3,000
N3	17.6	1.1×10^{18}	5,000

Hence, N BEP variation was found to fall within a narrow window for a high quality growth of InSbN epilayer. Although no trend in the surface roughness observed with increase in N BEP, an increase in n and reduction in μ was evident for higher N BEP. The increase in n at high N BEP can be due to the donor nature of N and a corresponding reduction in μ is believed due to the defects in InSbN layer attesting to the micro Raman (Figure 5.4) results.

The absorption spectra of InSbN (Figure 5.6) grown at 380 °C under different N plasma BEP indicate the effect of high N on the optical property of the epilayer. The high n observed in these InSbN epilayers results in Moss-Burstein shift which blue shifted absorption edge. In case of N2 and N3 the increased absorption beyond 10 µm after the band edge can be attributed to the plasma resonance absorption due to the enhanced carrier concentration. The band gap values for N1, N2 and N3 were estimated to be 0.16 eV (7.8 µm), 0.071 eV (17.35 µm) and 0.094 eV (13.21 µm), respectively. These estimated band gap values correspond to a theoretical N incorporation of 0.2 %, 1.2 % and 1 % for N1, N2 and N3, respectively.[70]

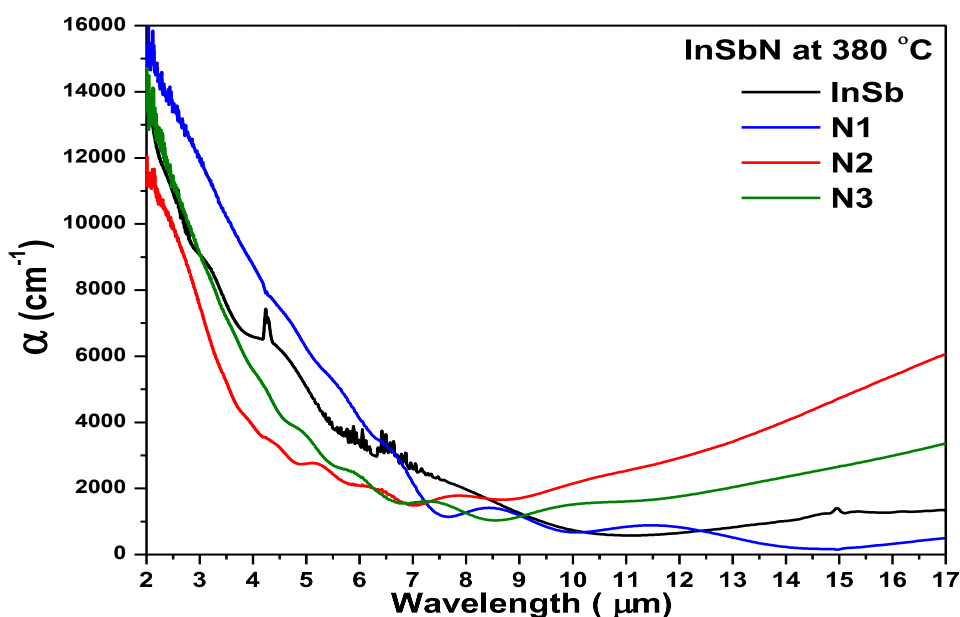

Figure 5.6. RT FTIR absorption spectra of InSbN epilayers grown at various N plasma BEP, compared with the reference InSb.

5.3.2 Growth temperature variation. All the InSbN epilayers T1, T2 and T3 were observed to be grown under a RHEED pattern of *c*(1x3) (as shown in Figure 5.1 (c) and (d)) indicating an Sb rich 2D growth. Figure 5.7 shows the HRXRD spectra of InSbN heterostructures grown at different temperatures. A sharp peak with FWHM 40 arcsec was observed at 66.05° corresponding to the GaAs substrate. The InSb peak was observed at 56.8° with FWHM ~ 190 arcsec for all the three InSbN heterostructures. An additional peak on the right of InSb was observed only for T1 and T2 at 57.12 and 57.13°, respectively was assigned as the nitride peak. The nitride peak was observed to exhibit a slightly higher FWHM of ~ 210 arcsec indicating degradation due to N incorporation as compared to the InSb HRXRD peak.

The simulation of HRXRD data indicated an N incorporation of 2.4, 2.7 and <0.5 % for T1, T2 and T3, respectively assuming all the InSbN layers 100 % relaxed. It is to be noted that the N % was estimated using simple Vegard's law considering the mismatch observed in the InSbN peak was only due to N incorporation, ignoring any mismatch arising from the interstitials.[81] This may result in a discrepancy in the N % estimated using this simple technique needs to be accounted, which has been discussed in details in Chapter 7.

Figure 5.8 shows the RT micro-Raman spectra of the InSbN heterostructures grown at different growth temperatures. It is evident that with the reduction in the growth temperature the InSb LO mode intensity also reduced indicating an increase in crystal lattice distortion due to high N incorporation at lower growth temperatures. Further, InSb 2LO observed only for T3 indicates highly crystalline nature due to very low N incorporation attesting to the low estimated N % from HRXRD. This clearly shows the increase in N incorporation with reduction in growth temperature. Hence, the defects observed in case of T2 and T3 is predominantly due to the increase in N incorporation at lower growth temperatures.

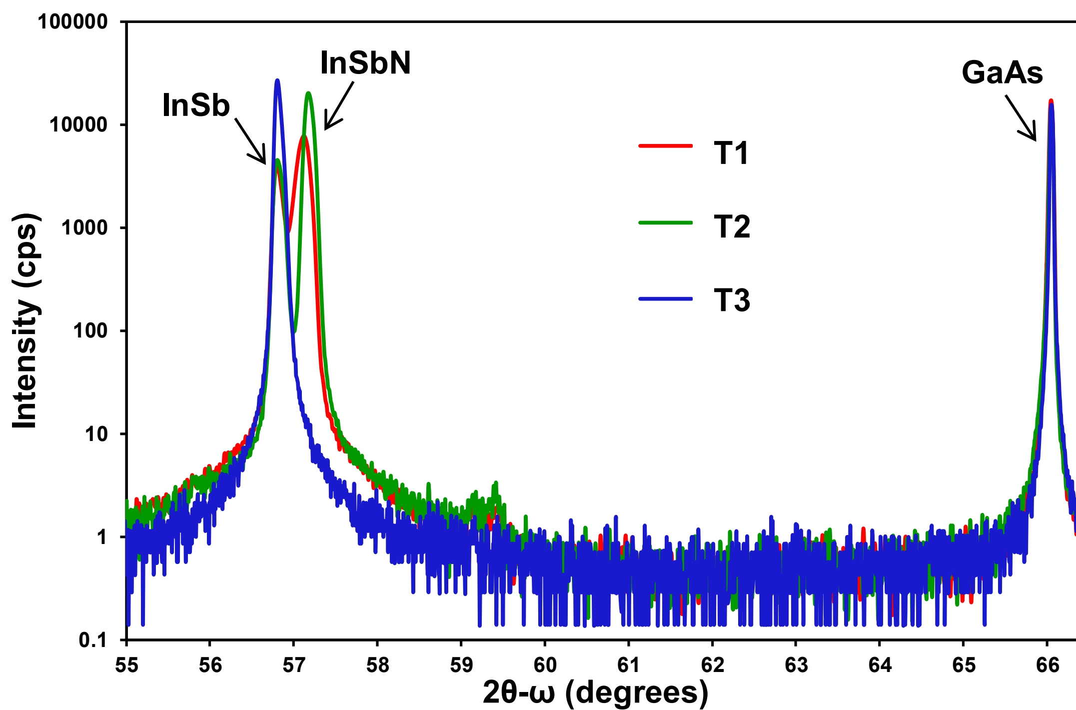

Figure 5.7. (004) HRXRD scan of InSbN epilayers grown at various temperatures along with the reference InSb sample.

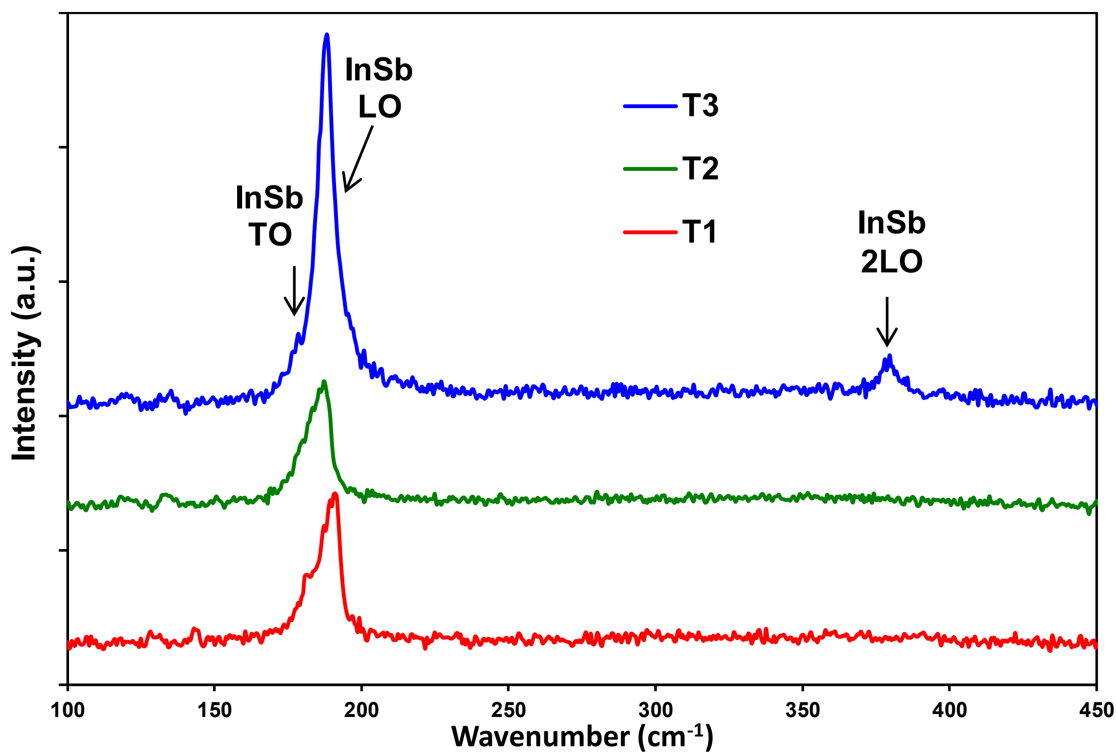

Figure 5.8. RT micro-Raman spectra of InSbN heterostructures grown at different temperatures.

Table 5.2 compares the surface roughness of all the InSbN heterostructures grown at different temperatures along with corresponding RT Hall data. Although there is no trend in the surface roughness with change in growth temperature, the roughness values observed to be higher than that of InSb heterostructures. However, a trend in the reduction in μ_{RT} and increase in n_{RT} observed with an increase in estimated N %. This can be clearly due to the defects in the crystal after an N incorporation. A detail study of Hall data correlating to various N related bonding has been reported in Chapter 6.

Table 5.2

Comparison of AFM measured surface roughness and Hall data of InSbN epilayers grown at different growth temperatures.

InSbN heterostructure	AFM RMS (nm)	n_{RT} (cm^{-3})	μ_{RT} (cm^2/Vs)
T1	5	1.6×10^{17}	12,500
T2	7	2.2×10^{17}	11,500
T3	6	1.1×10^{17}	46,500

Figure 5.9 compares the RT transmission spectra of InSbN heterostructures grown at different temperatures. To estimate the absorption edge, Figure 5.10 compares the RT absorption spectra of these InSbN heterostructures with InSb reference heterostructure. All the InSbN heterostructures observed to exhibit an absorption edge at a relatively lower energy than InSb. It can clearly be seen than T1 and T2 exhibit an extended absorption edge as compared to T3. However, due to a comparable thickness between the InSbN epilayer and the InSb, an interference of the Fabry Perot fringes makes it very difficult to estimate the exact absorption

edge and the corresponding bandgap values. Hence, heterostructures with relatively thick InSbN and thin InSb layer need to be used to study the absorption edge of the InSbN epilayers. The absorption results of such InSbN heterostructures have been reported in Chapter 7. Further, a correlation of Hall data with the absorption edge in InSbN has been reported in Chapter 6.

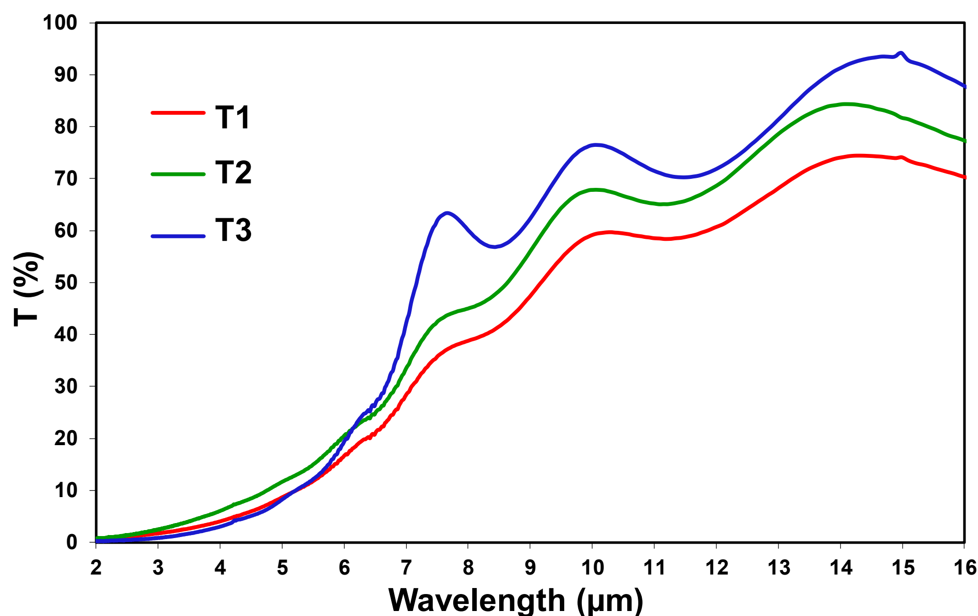

Figure 5.9. RT FTIR transmission spectra of the InSbN epilyaers grown at different Ts.

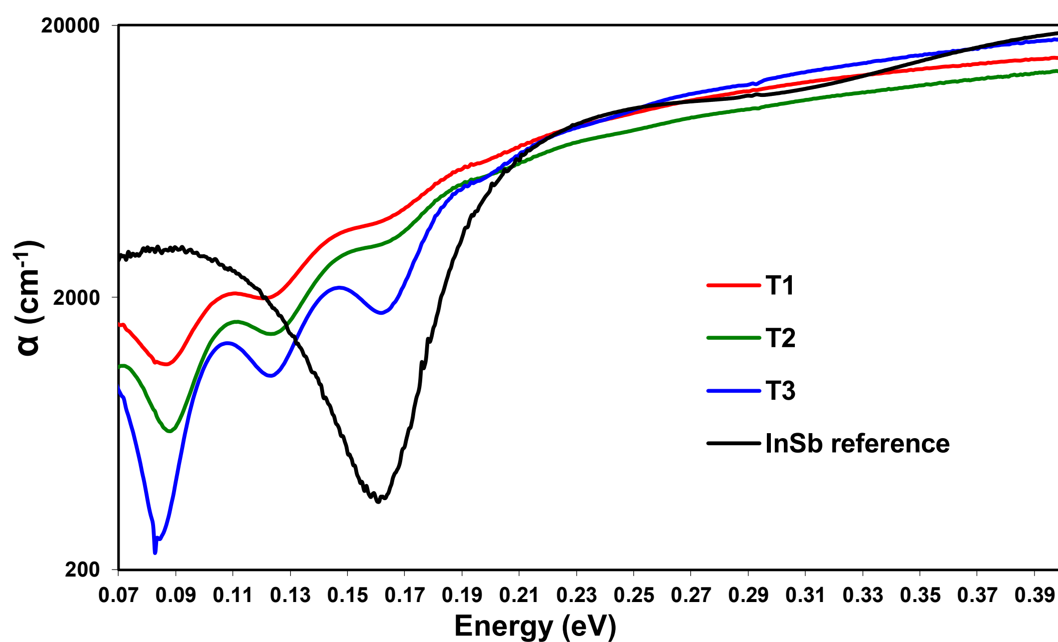

Figure 5.10. RT absorption spectra of InSbN epilayers grown at different Ts with InSb reference.

5.4 Conclusion

InSbN epilayers were grown by varying N plasma at a constant growth temperature and by varying growth temperature at constant N BEP. With increase in N BEP the N incorporation in the InSbN layers were observed to increase. However, a very narrow window of N BEP was observed to be favorable for the growth of crystalline quality InSbN epilayers. Further, higher N BEP was observed to result in very rough surface and high background carrier concentration with low mobility. Moreover, reduction in the growth temperature at a fixed N BEP observed to provide a favorable growth condition for good quality InSbN epilayers with an increase in N incorporation up to 2.7 %. Further, a large window of growth temperatures from 290 °C to 380 °C can be used for the growth of InSbN epilayers resulting in an absorption edge at a higher wavelength as compared to InSb. However, InSbN growth at low temperature observed to create crystalline defects, as determined from Raman data, resulting in low RT mobility which need further systematic study. In addition, relatively thick InSbN epilayer needs to be grown on a thin InSb buffer to study the optical absorption and hence the determination of the optical band gap from the absorption edge. Finally it can be concluded that, growth of InSbN epilayers with high N incorporation can effectively be achieved by reduction of growth temperature instead of increase in N BEP.

CHAPTER 6

Study of N Incorporation in InSbN with Variation in Growth Temperature

6.1 Introduction

Amongst the different growth parameters, the variation of growth temperature was reported[122] to have a greater impact in the incorporation of N in III-V dilute materials, particularly in GaNSb. A similar behavior in case of InSbN has been reported briefly by Lim et al[89] and Zhang et al.[83] In this chapter, we present a systematic study on the effect of N incorporation as a function of growth temperature, correlating the structural, type of N- bonding and optical characteristics of InSbN grown on GaAs substrate using various characterization techniques. All the results and discussion in this Chapter have been published.[30]

6.2 Experimental Details

The InSbN layers of 0.4 μm thickness were grown at three substrate temperatures (Ts) of 290 °C, 330 °C and 380 °C keeping a constant Sb:In BEP ratio of 3:1 and N rf plasma power of 200 W. An N BEP of 1×10^{-7} Torr and growth rate 0.4 μm/hr was maintained during the InSbN epilayer growth.

6.3 Results

6.3.1 RHEED. Figure 6.1 shows the RHEED patterns (a) x1 along (110) and (b) x3 along $(1\overline{1}0)$ azimuths during the growth of InSbN epilayer. The combination of these two RHEED patterns where were observed at two different sample orientations separated by 90° is denoted by *c*(1 x 3). Such RHEED patterns were observed during the growth in case of InSbN epilayers grown at 290 °C and 330 °C. The streaky RHEED patterns for the InSbN epilayers, indicative of a 2D growth for all the nitride epilayers reported here. A sharp change in RHEED pattern from a pseudo x3 (Figure 4.2 (b)) to a clear x3 (Figure 6.1 (b)) surface reconstruction upon opening the

N shutter is indicative of a phase transition of the growth front that leads to an abrupt interface and an Sb rich surface.

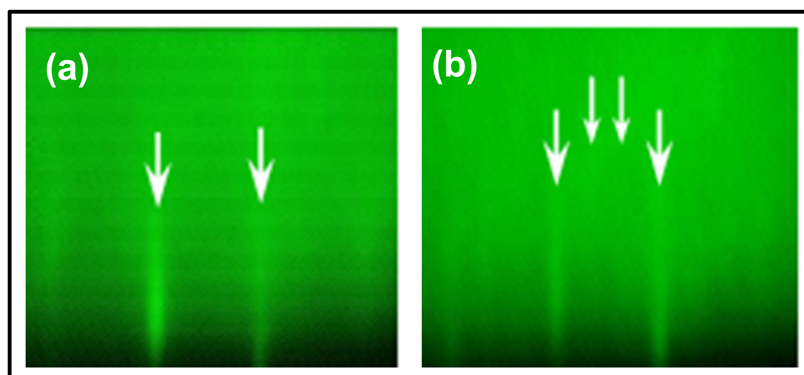

Figure 6.1. RHEED patterns showing a *c*(1 x 3) reconstruction during the growth of InSbN epilayers.[30]

6.3.2 HRXRD. Figure 6.2 shows the HRXRD (004) spectra of InSbN epilayers grown under various growth temperatures along with the InSb reference. InSb exhibited a FWHM of 200 arcsec, while the best FWHM of 207 arcsec has been observed on nitride epilayer grown at 290 °C. Epilayers grown at 290 °C and 330 °C exhibit a distinct InSbN peak, whereas epilayer grown at 380 °C does not exhibit a distinct nitride peak.

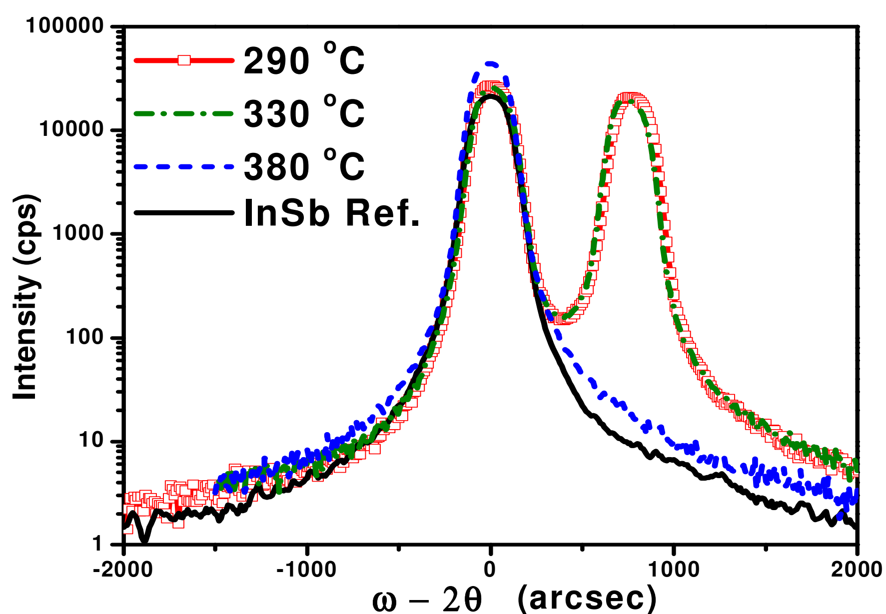

Figure 6.2. HRXRD (004) scan of InSbN epilayers grown at different Ts with InSb reference.[30]

6.3.3 Micro-Raman spectroscopy. Figure 6.3 (a) shows the micro-Raman spectra of InSbN epilayers with varying growth temperatures and a reference InSb epilayer. The well-defined InSb LO phonon mode at 190 cm^{-1}, a weak InSb TO phonon mode at 181 cm^{-1} and a clear 2nd order InSb LO (2LO) mode at 380 cm^{-1} were observed in the reference InSb epilayer. In case of nitride epilayers no InSb 2LO modes were observed. Further, none of the test samples (both InSb and InSbN epilayers) observed to exhibit low order E_gSb or A_{1g}Sb modes.

Figure 6.3 (b) shows the Lorentzian fit for the first order InSb TO and LO Raman of InSbN epilayers and InSb reference. The intensity of individual TO (I_{TO}) and LO (I_{LO}) phonon modes were estimated after deconvoluting them. The intensity ratio I_{TO}/I_{LO} as listed in Table 6.1, has been used to quantify and compare the disorder in the crystal lattice of the corresponding epilayers.[83] The InSbN epilayer grown at 330 °C observed to exhibit relatively higher I_{TO}/I_{LO} ratio as compared to the epilayers grown at 290 and 380 °C. Further, the FWHM of individual peaks (both LO and TO modes) were observed to increase with reduction in growth temperatures.

Table 6.1

Comparison of N_{Sb} (%) from HRXRD, N 1s XPS peak compositions along with I_{TO}/I_{LO} ratio from micro-Raman and electrical properties measured at 0.5 kG of InSbN epilayers grown at different temperatures.

Ts (˚C)	HRXRD N (%)	In-N (%)	In-N-Sb (%)	Sb-N (%)	Raman I_{TO}/I_{LO}	n_{RT} (cm^{-3})	μ_{RT} (cm^2/V-s)
290	1.4	60	11.3	28.7	0.7	8.5×10^{16}	20,000
330	1.4	68.4	2.1	29.5	1.3	9.2×10^{16}	19,000
380	-	43	34.7	22.3	0.2	1.6×10^{17}	14,000

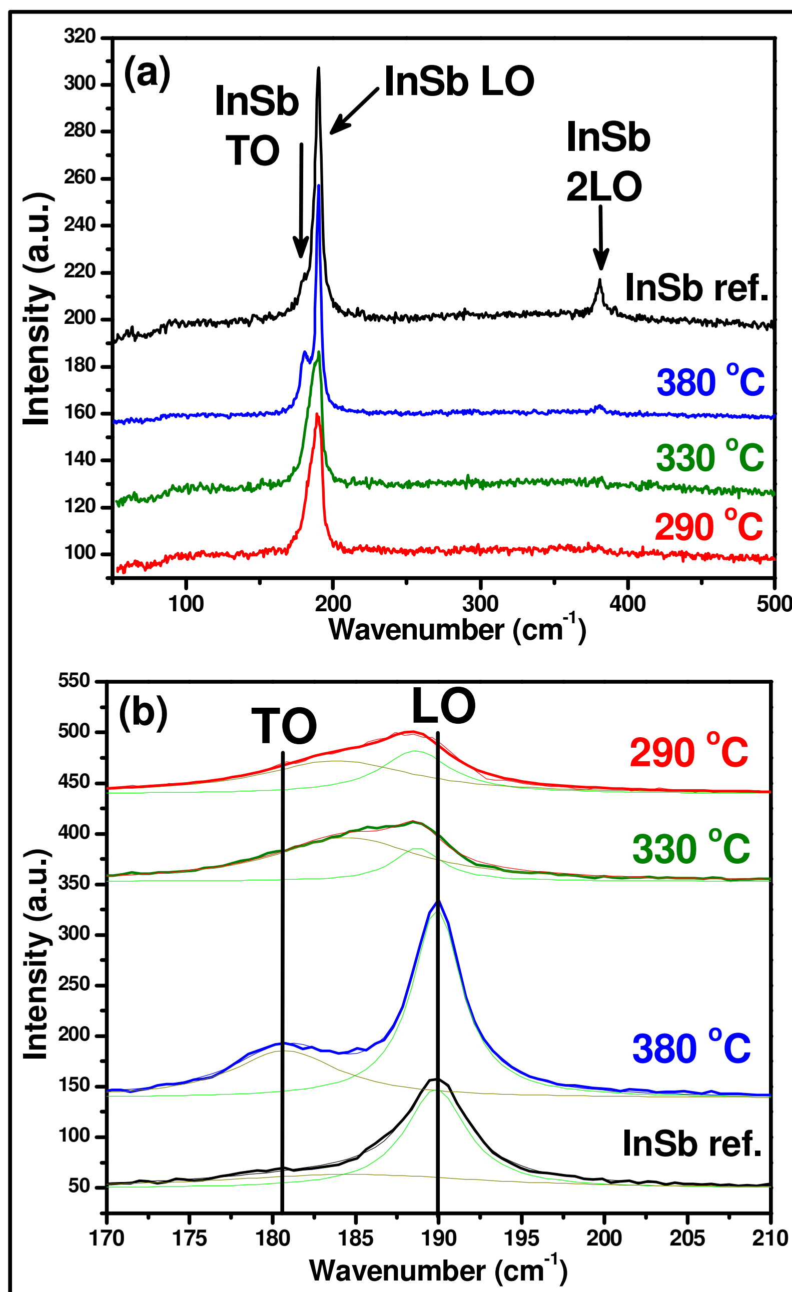

Figure 6.3. (a) Comparison of RT micro-Raman spectra of the InSb reference epilayer with InSbN alloys grown at different temperatures, (b) Lorentzian fit for Raman spectra in first order TO and LO phonon ranges of all the epilayers represented in Figure (a).[30]

6.3.4 XPS. Figure 6.4 shows the N 1s spectrum of nitride epilayers grown at different growth temperatures. Table 6.1 indicates the composition of various nitrogen bonds present in the epilayers grown at different temperatures for a constant N plasma power and N BEP.

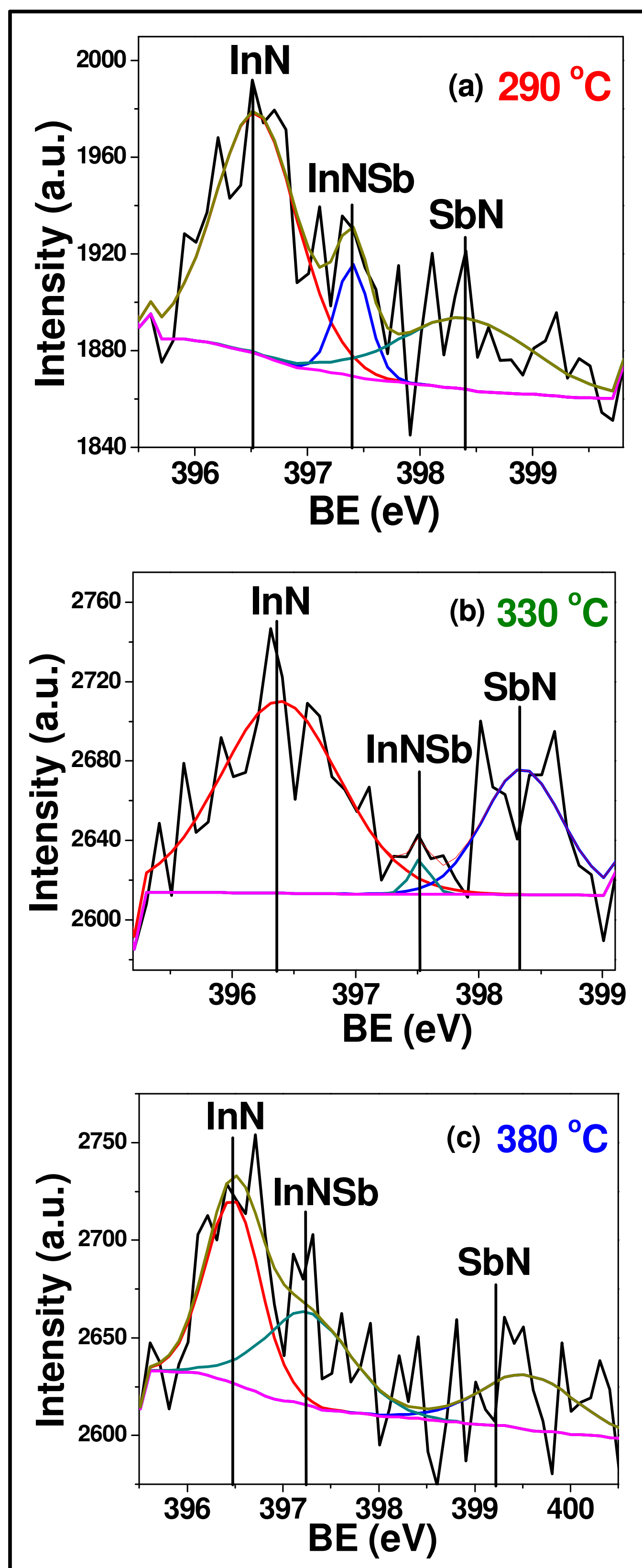

Figure 6.4. N 1s spectrum of InSbN epilayers grown at different temperatures.

6.3.5 AFM. Figure 6.5 shows the surface study of all the grown epilayers. The surface roughness R_{rms} for these epilayers ranged from 5.4 nm to 14.7 nm and no systematic variation was observed as a function of growth temperature.

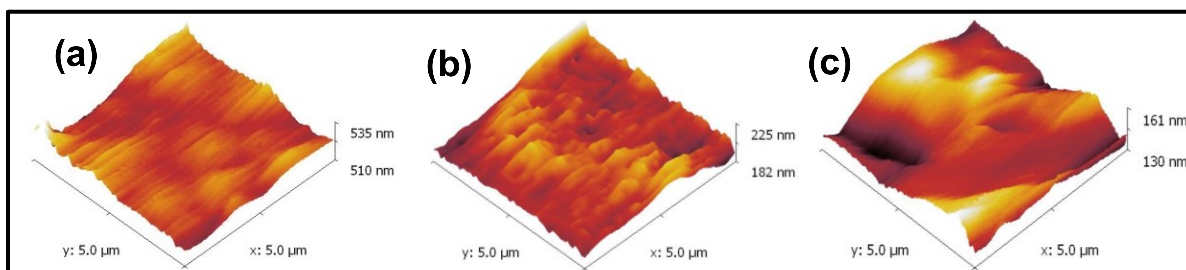

Figure 6.5. AFM images of InSbN epilayers grown at (a) 290, (b) 330 and (c) 380 °C.[30]

6.3.6 Hall measurement. RT and 77 K single-field Hall measurements were carried out on all epilayers to determine the electrical properties. Figure 6.6 compares the RT and 77 K Hall n and μ values measured at a 5.8 kG magnetic field for the InSbN epilayers grown at various temperatures.

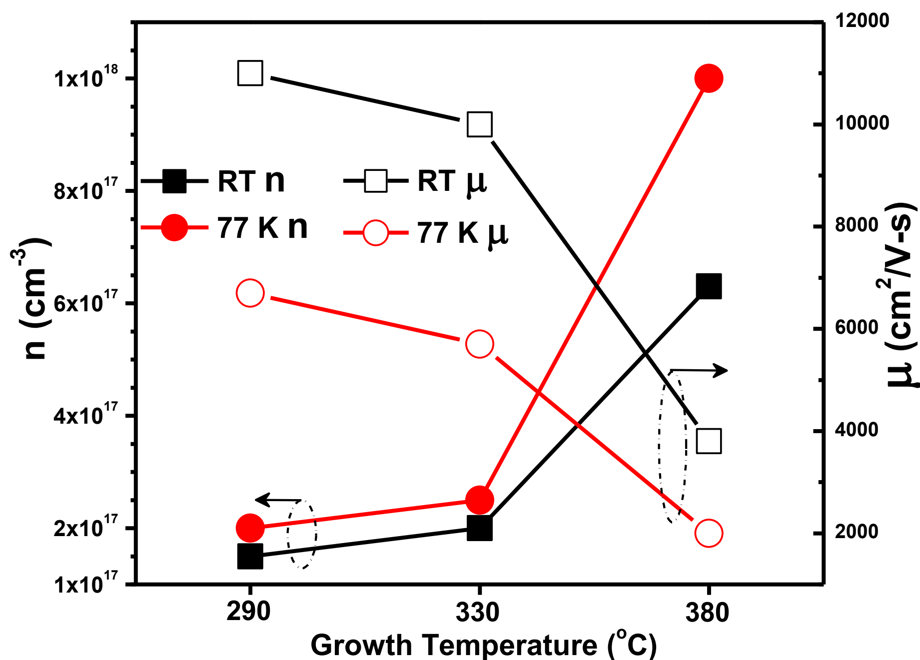

Figure 6.6. RT and 77 K Hall n and μ measured at 5.8 kG for InSbN epilayers grown at different growth temperatures.[30]

Figure 6.7 compares the RT Hall n and μ values measured at two different magnetic fields 0.5 and 5.8 kG, for the InSbN epilayers grown at different temperatures. The carrier concentration and mobility for all the epilayers are tabulated in Table 6.1. The InSb reference epilayer exhibit an intrinsic level carrier concentration of 2.6×10^{16} cm^{-3} and a mobility 38,000 cm^2/V-s. Since the effect of magnetoresistance is still present in these values, this comparison is only for a qualitative study of the scattering mechanisms.

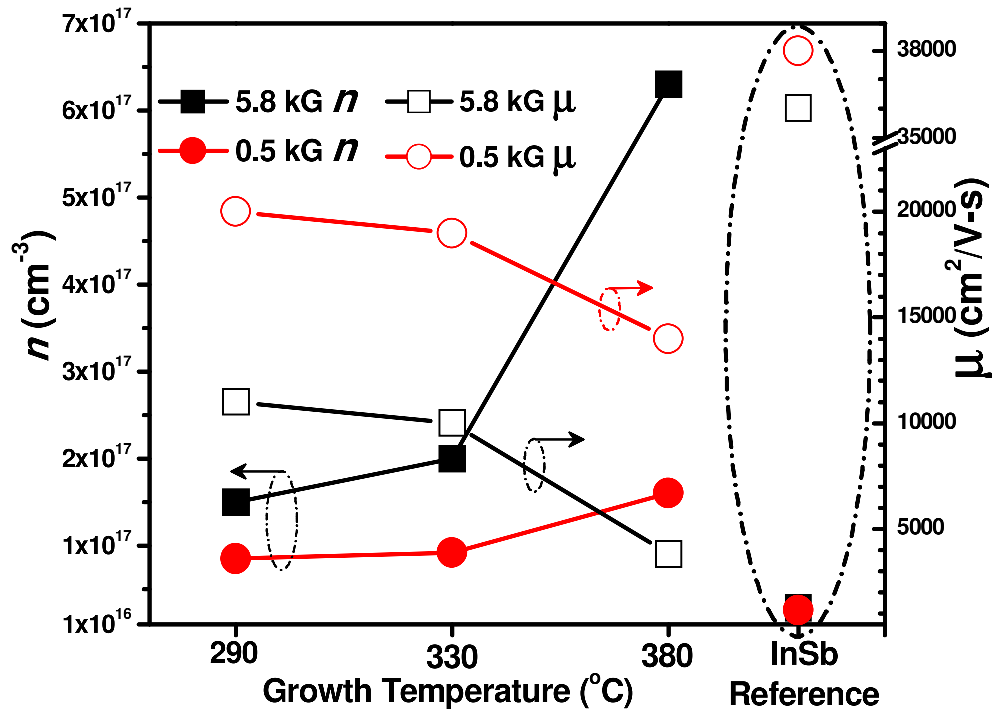

Figure 6.7. RT Hall carrier concentration (n) and mobilities (μ) measured at 0.5 and 5.8 kG magnetic.[30]

All the nitride epilayers show an increase in background carrier concentration and relatively lower mobility (values indicated in Table 6.1) as compared to the reference InSb. The lowest carrier concentration of 8.5×10^{16} cm^{-3} and highest mobility 20,000 cm^2/V-s was exhibited by the epilayer grown at 290 °C. The Hall measurements were also carried out at a high field of 5.8 kG both at RT and 77 K for a qualitative comparison between the epilayers.

6.3.7 FTIR. Figure 6.8 shows α vs eV plot for all representative epilayers grown at various temperatures, along with InSb reference. The InSb reference exhibits a sharp absorption edge at 0.17 eV. Epilayers grown at lower temperatures of 290 °C and 330 °C exhibit a redshift in the absorption edge, with a cutoff at ~0.135 eV while the ones grown at 380 °C have an edge at 0.15 eV.

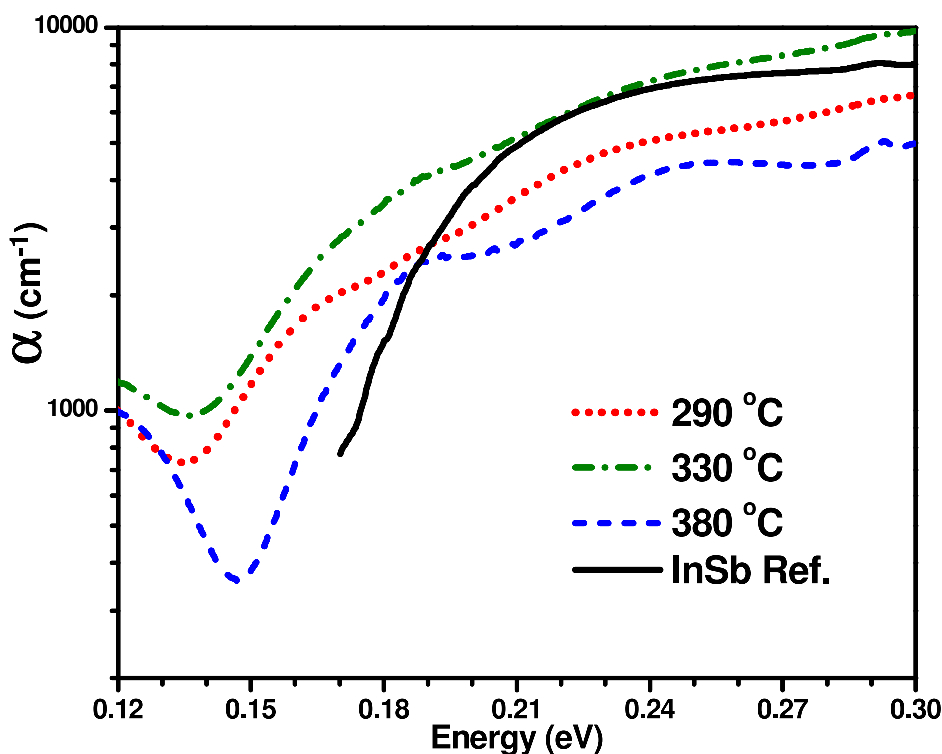

Figure 6.8. α vs energy plots for InSbN epilayers grown at different temperatures compared with InSb reference.[30]

6.4 Discussion

The HRXRD spectra of InSbN epilayers grown at different growth temperatures (Figure 6.2), exhibit distinct positive mismatched nitride peaks on epilayers grown at 290 °C and 330 °C, indicative of lattice contraction with N incorporation. N composition is found to be ~ 1.4±0.2 % in both the above epilayers, as determined from XRD simulation. However, SIMS (Figure 3.10) performed on the InSbN epilayer grown at 290 °C exhibited an N content of 2±0.2 %. The higher

N content observed by SIMS as compared to HRXRD, indicates that a relatively small amount of N goes into the interstitial sites as compared to the substitutional sites. These interstitials can be in different directions as reported by Pham et al,[81] affecting the overall positive or negative mismatch of the InSbN epilayer. Furthermore, the N % estimated using simple Vegard's law from the corresponding (004) HRXRD scan do not account for the mismatch in the InSbN epilayers due to interstitials. Hence, an error factor of ±0.2 % was applied and observed to account for this discrepancy. In case of epilayers grown at a higher temperature of 380 °C, although do not exhibit any distinct nitride peak but N was estimated to be 0.5±0.2 %. A somewhat larger FWHM of 210 arcsec makes it very difficult to distinctly detect nitride peak in the x-ray spectrum due to less mismatch with respect to the InSb buffer. Also the presence of an N 1s peak in the corresponding XPS spectra (Figure 6.4 (c)), confirms the N incorporation. Thus, our growth procedure appears to provide a wider growth temperature window in contrast to earlier reports,[83, 89] where N incorporation was found to be more strongly influenced by growth temperature.

It is to be noted that the observed HRXRD FWHM of the InSb peak is always lower than the corresponding InSbN peak, indicating an increase in crystal disorder with the addition of N. The best (004) HRXRD FWHM (207 arcsec) observed for our InSbN epilayer grown at 290 °C is found to be comparable to the corresponding InSb FWHM (205 arcsec) with similar intensities, attesting to the good quality of the layer grown and is considerably less than the FWHM values reported by Lim et al[82] grown using a thin buffer or two-step buffer growth process. Although the InSbN epilayer thickness reported here are relatively thinner than those of Lim et al, similar results were observed (Figure 5.7) for the 1.2 μm thick InSbN epilayers grown under similar growth conditions. Furthermore, AFM shows overall surface roughness values

higher than the values reported in the literature[123] for InSb grown on GaAs. The increase in surface roughness is attributed to the presence of interstitials and N related disorders.

Most of the N incorporation was found to be in the form of In−N bonding, from XPS spectra, which happens to be substitutional (N_{Sb}) resulting in lattice contraction, observed as a unique nitride peak in the corresponding HRXRD spectrum (Figure 6.2).[81] The formation of In-N bonds leaves more numerous highly-reactive Sb atoms readily available for bonding to attain a thermodynamic equilibrium, which leads to other types of bonding, namely the Sb−N and In−N−Sb present in all our epilayers, and is believed to have formed during the nitridation process as proposed in the anion exchange model.[88] Although the presence of N−N interstitials were reported by Lim et al[89, 93] in their InSbN epilayers, no such XPS peak corresponding to N−N binding energy (303.8 eV) has been observed in our InSbN epilayers (not shown here). Hence, in our case Sb−N has been the major contributor of N− related point defects, which causes the lattice expansion as observed by Pham et al in their samples.[81] Formation of these interstitials, either N−N, Sb−N or both, are believed to be dependent on various nitridation parameters.[124, 125] The high percentage of In−N−Sb bonding observed in the epilayers grown at 380 °C as compared to the epilayers grown at 290 °C and 330 °C is attributed to a weak bonding formed because of lower energetic N ions. However, since in our case the N flow rate and plasma power remained invariant for the growth of all the three nitride epilayers, the variation in the In−N−Sb bonding appears to be influenced by the growth temperature. In these bonds, the N is bonded with both In and Sb atoms,[126] indicating the interstitial nature of the bonding. In−N−Sb is believed to have a smaller bond length as compared to In−Sb but larger than In−N, resulting in relatively less lattice contraction as compared to In−N. This explains the absence of a distinct nitride peak in the corresponding x-ray spectrum of the epilayer grown at 380 °C (Figure 6.2).

Hence, we speculate N in the form of In−N−Sb bonding to create less lattice distortion as compared to other N bonding such as In−N, Sb−N and N−N. The effect of this bonding on the crystal structure and electrical properties will be discussed in greater detail.

Thus the distribution of different N bonding configurations has been found to be a strong function of growth temperature. For a fixed Sb, In and energized atomic N arrival rate, the growth temperature provides a unique thermodynamically favorable condition for the formation of different types of N bonding. As discussed earlier for all the three growth temperatures, the substitutional N incorporation occurs in the form of In−N bonding, which is favored at relatively lower growth temperature, consistent with the reports in the literature.[21, 81, 83, 89, 91] However, an opposite trend is observed for the formation of In−N−Sb bonding. Sb−N bonding on the other hand appears to be independent of the growth temperature. Furthermore, Veal et al[91] have also reported that Sb−N bonding remains invariant upon annealing up to 300 °C in their InSbN epilayers. The robustness of this bonding clearly indicates the challenge in reducing these interstitials in this material system.

Raman spectra of the reference InSb epilayer (as discussed earlier) exhibit sharp InSb LO and 2LO modes, illustrating high crystalline quality. With the introduction of N, degradation in the quality of epilayers is evident from the reduction in the InSb LO mode in conjunction with an enhanced InSb TO mode (Figure 6.3 (a)), caused by changes in the local lattice structure.[88] The absence of low energetic acoustic phonon modes indicates that there are no Sb related defects, such as Sb segregation on the surface and Sb antisite defects, in contrast to earlier reports[88, 93] on InSbN grown on both InSb and GaAs substrates. Variation of lattice disorder with growth temperature is reflected from the Raman I_{TO}/I_{LO} ratio (will be referred to as disorder) (Figure 6.3 (b)) and can be correlated to the types of N bondings observed in the corresponding XPS spectra

(Figure 6.4 and Table 6.1). The InSbN epilayer grown at 380 °C shows only a slight increase in the disorder as compared to the reference InSb epilayer. With the reduction in growth temperature from 380 °C to 290 °C, a substantial increase in the disorder, upward shift in InSb TO mode and downward shift in LO mode can be correlated to the increase in the In−N % bonding. A relatively higher disorder observed for the epilayers grown at 330 °C, as compared to other growth temperatures, is consistent with the work reported by Lim et al,[88] who reported the highest degree of lattice distortion at 330 °C. The downward shift in the InSb LO mode observed in the epilayers grown at 290 and 330 °C has generally been attributed to either the shortening of phonon correlation length[127] or LO modes associated with microscopic electric field variation due to N incorporation.[83] However, in our study we see a direct correlation between the In−N % bonding and Raman disorder. Hence, we speculate this frequency shift to be the result of correlation length shortening caused by compositional disorder at higher N incorporation.[127, 128]

The effect of the nature of N-bondings is also reflected in the electrical properties of these epilayers, as is evident from the Hall measurements (Table 6.1). To study the true effect of N incorporation on the electrical properties of the InSbN epilayers, the dislocation density due to heterojunction needs to be accounted first. Using Equation 3.1 the density of the dislocations in the reference InSb epilayer was calculated to be 2.6x10^{8} cm^{-2}. The dislocation density was reported to be a function of the epilayer thickness,[57, 129] and this estimated value matches with the corresponding InSb epilayer thickness and observed mobility as reported in the literature.[47, 110] Furthermore, the observed HRXRD FWHM for all the reported InSbN epilayers are close to the reference InSb epilayer indicating not much variation in the dislocation density for the InSbN epilayers. Hence, any change in the electrical properties of the InSbN epilayers as compared to the reference InSb epilayer needs to be accounted due to the effect of N incorporation. The

variations in the n and μ with growth temperature of these InSbN epilayers seem to closely follow the combination of % In−N and % In−N−Sb bonding (Table 6.1). At RT, the μ is dominated by alloy scattering and lattice scattering, while at 77 K it is scattered by ionized impurities and heteroepitaxial dislocation defects.[82] In the case of high magnetic field Hall measurements on these InSbN epilayers, RT n increased further and μ decreased by ~ 50% with respect to the low field values. These are attributed to the magneto-resistance effect.

At 77 K, a further increase in n (2×10^{17} to 1×10^{18} cm^{-3}) and decrease in μ (6.7×10^{3} to 2×10^{3} cm^2/V-s) was observed for all the InSbN epilayers. This can be attributed to the increase in impurity scattering that becomes dominant at the low temperatures, as the heteroepitaxial dislocation scattering is believed to be less, due to high crystalline quality of the InSb reference epilayer attested to by Raman spectra (Figure 5.4). The epilayers grown at 380 °C exhibits the highest n with the lowest μ and can be associated with a combination of higher % In−N−Sb bonding and low % In−N bonding states indicative of more N in the interstitial position. The observed behavior of the electrical properties of these epilayers is somewhat different from the literature.[82] The best RT μ of 20,000 cm^2/V-s has been observed on our epilayers grown at 290 °C, and is considerably higher than the values reported by Lim et al.[82] These measured values are believed to be overestimated for the InSbN material system, due to an influence of the InSb buffer in our epilayers. It is worth noting that, with a relatively thicker InSb buffer in our InSbN epilayers for this study, a multi-channel conduction phenomenon is believed to arise.[118] Hence, the actual electrical properties of InSbN may not be evident with these results. However, the overall trend observed in the electrical properties of InSbN epilayers with growth temperature can be explained by variation in N− bondings. Based on the specific composition of the N− bonding, weather N is in substitutional or interstitial site the behavior of the material is reflected.

RT FTIR results indicate a bulk-like absorption edge for the InSb reference epilayer, which again attest to the good quality of the InSb epilayers. Figure 6.8 compares the absorption coefficient of all the InSbN epilayers along with the reference InSb heterostructure. The epilayer grown at 380 °C exhibits only a slight redshift in the absorption edge at 0.15 eV (8.3 µm), whereas epilayers grown at 290 °C and 330 °C both exhibit a maximum redshift of up to ~ 0.135 eV (9.2 µm), consistent with the increased N incorporation in the substitutional sites.[130] The observed band gap of these epilayers includes the Moss-Burstein blue shift due to high background *n*. The band gap values for the InSbN epilayers grown at 290, 330 and 380 °C were estimated (using Equation 2.1) to be 0.094 eV (13.2 µm), 0.104 eV (11.9 µm) and 0.065 eV (19 µm), respectively with a corresponding theoretical N incorporation of 1.2 %, 1 % and 1.3 %, respectively. The theoretical N incorporation values were inferred from the band anticrossing model reported by Murdin et al.[70] Although the theoretical N incorporation is close to the HRXRD estimated N incorporation for the InSbN epilayers grown at lower growth temperatures, the N % corresponding to the band gap estimated for the epilayer grown at 380 °C observed to be overestimated. The discrepancy in the N % can be accounted by the presence of maximum % of In−N−Sb bonding which also contributes to more active N for band gap reduction[126] with little contribution towards lattice mismatch in the corresponding nitride layer.

6.5 Conclusion

These results on InSbN epilayers conclude that the growth conditions should not only be optimized for high N incorporation (N_{Sb}), but also for reduced N related defects to observe a band gap reduction for better device performance. Also they clearly show that lower growth temperature favors In-N bonding, which dictates N composition, whereas high growth temperature favors the formation of In−N−Sb bonding. The crystal lattice disorder arising due to

N incorporation is predominantly due to In−N bonding, as compared to any other N bonding states. The 77 K electrical transport parameters are dictated by ionized impurity scattering, which can be correlated to In−N−Sb bonding as opposed to RT transport parameters dominated by lattice scattering due to disorder with increase in N incorporation. We found that for InSbN epilayers, a low growth temperature of 290 °C was optimum, with a relatively high % of In−N bonding corresponding to 1.4 % of N_{Sb} with reduced lattice disorder and comparatively less % of In−N−Sb bonding states. The above epilayer demonstrated a maximum redshift, with an absorption cut-off at 0.135 eV (~ 9.2 μm), the lowest carrier concentration and highest Hall mobility, at both RT and 77 K.

CHAPTER 7

Effect of Annealing on InSbN

7.1 Introduction

Annealing forms an important part of the study of dilute nitride systems, in general, as it leads to significant improvement in the quality of the epitaxial layers due to reduction in defects and localized N-centers.[121, 131-133] Wang et al[79, 95] reported the out diffusion of N atoms from the bulk to both the surface and the substrate in their ion implanted $InSb_{1-x}N_x$ alloys, on annealing for extended durations even for annealing temperatures below 400 ºC, which they attributed to an interstitial dominated diffusion mechanism. The post growth[28] RTA of MBE grown InSbN epilayers was reported to have no significant change in the total N content for annealing temperatures up to 430 ºC.[93] Improvement in the crystalline quality, reduction in room temperature (RT) carrier concentration to the intrinsic level with increase in mobility and a red shift in the RT band gap of the material up to 0.15 eV have been reported in these annealed MBE grown layers, due to the annihilation of N−N interstitials. However, *in-situ* annealing of InSbN sequentially grown on two step InSb buffer on GaAs substrate using MBE, has been reported[28] to result in a net loss of incorporated N (N_{Sb}) at an annealing temperature of 430 ºC. A maximum photodetection limit up to 10 μm at 77 K was achieved using the *in-situ* annealed samples. Although these annealing studies of InSbN reported in the literature clearly indicate the improved quality of InSbN epilayers, the data is scattered. Hence, in the current work we present the results of our detailed and comprehensive investigation on a comparative study of *as-grown* and annealed (both *ex-situ* and *in-situ*) InSbN epilayers on the structural, vibrational, electrical and optical properties using various characterization techniques. The comparative study of annealing (*as-grown*, *ex-situ* and *in-situ*) has been peer reviewed and published.[134]

7.2 *Ex-situ* Annealing

A systematic study of RTA was carried out at different temperatures (400, 430 and 450 °C) for different durations (30, 60, 90, 120 and 180 sec) using InSbN heterostructures grown at different growth conditions. The electrical characteristics of the epilayers were not only observed to be dependent on the annealing temperature and duration but also on the InSbN epilayer thickness, growth temperature and N BEP. For example, RTA performed on InSbN heterostructures N1, N2 and N3 at annealing temperatures of 450, 430 and 400 °C, respectively for duration of 30, 90 and 60 sec, respectively indicated a maximum reduction in n from 2.6×10^{18} to 3.3×10^{17} cm^{-3} and increase in μ from 2,910 to 9,420 cm^2/Vs for N2. In the sample N3 the changes in n and μ were somewhat reduced, RT n reducing from 1×10^{18} to 5×10^{17} cm^{-3} with corresponding increase in μ from 5,000 to 7,400 cm^2/Vs. However, in case of N1, though the sample was annealed at the highest temperature, there was no significant change in n and μ observed after RTA attributed to a very short annealing duration. Hence, the duration of annealing was observed to be a critical factor besides the annealing temperature.

Figure 7.1 compares the HRXRD spectra of InSbN heterostructure N2 before and after *ex-situ* annealing. The single peak in the *as-grown* heterostructure observed to split into two with a peak onto the right of InSb peak at 2θ of 56.67°. The peak on the right at 56.81° emerged after annealing is believed to be due to InSbN with an increase in N incorporation during the process of annealing. However, no significant red shift w.r.t. InSb reference was observed in the absorption edge (Figure 7.2) after annealing. The high absorption observed in the *as-grown* N2 heterostructure at higher wavelengths (Figure 5.4) corresponding to energies below 0.18 eV (Figure 7.2) observed to reduce after annealing. Further, the process of annealing reduced (not shown here) the A_{1g}Sb observed in the corresponding micro-Raman spectra (Figure 5.4).

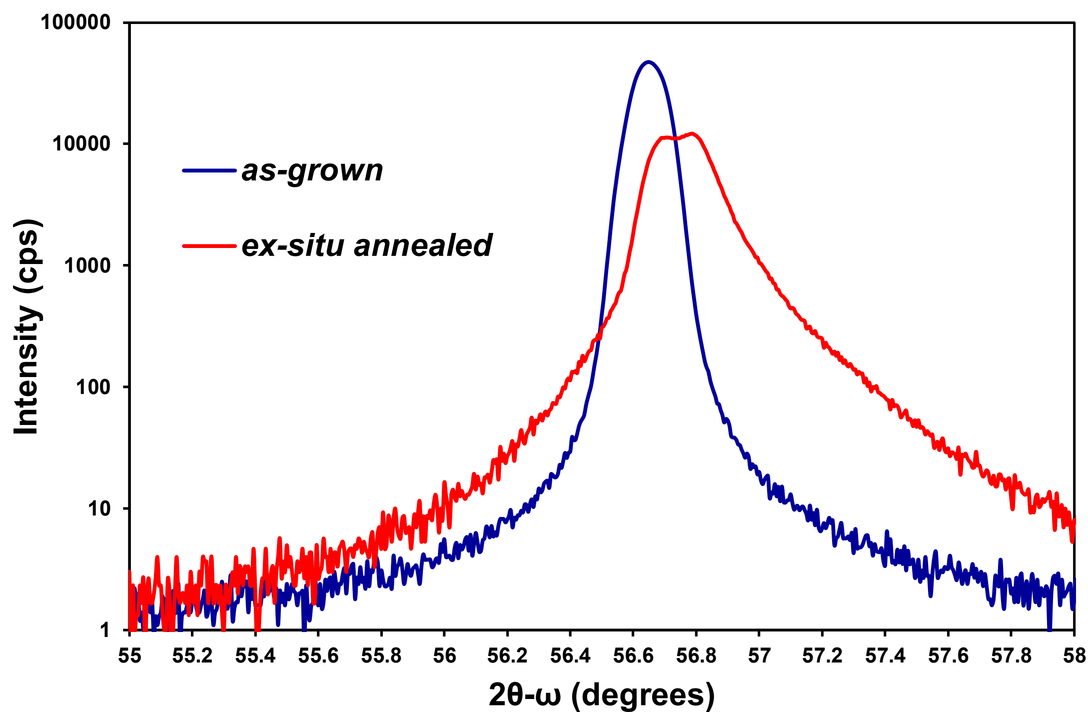

Figure 7.1. HRXRD spectra of InSbN N2 before and after *ex-situ* annealing.

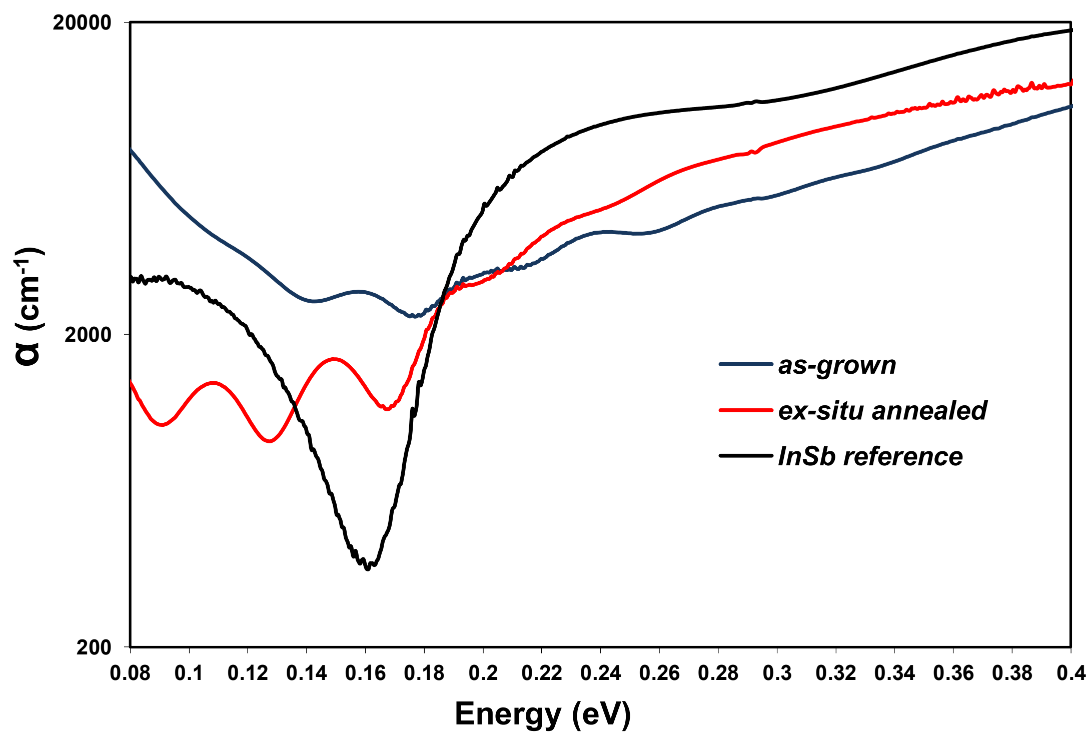

Figure 7.2. RT absorption spectra of InSbN N2 before and after *ex-situ* annealing compared with InSb reference heterostructure.

Ex-situ annealing was also performed on InSbN heterostructures grown at lower growth temperatures and high N BEP. In case of InSbN grown at 330 °C (T2) and 1.7×10^{-7} Torr (N3) when annealed at 450 °C for 45 sec, the absorption edge was observed to be at λ ~11.6 µm with n ~5×10^{16} cm^{-3} and μ ~42,000 cm^2/Vs. Figure 7.3 shows the RT optical absorption edge of the above InSbN heterostructure with absorption edge at 0.107 eV. Further, RT n in the range of ~10^{16} cm^{-3} results in a negligible Moss-Burstein shift in the band gap. Hence, the band gap of the material can be estimated to be same as 0.107 eV which corresponds to the theoretical N incorporation of 0.8 %.[70]

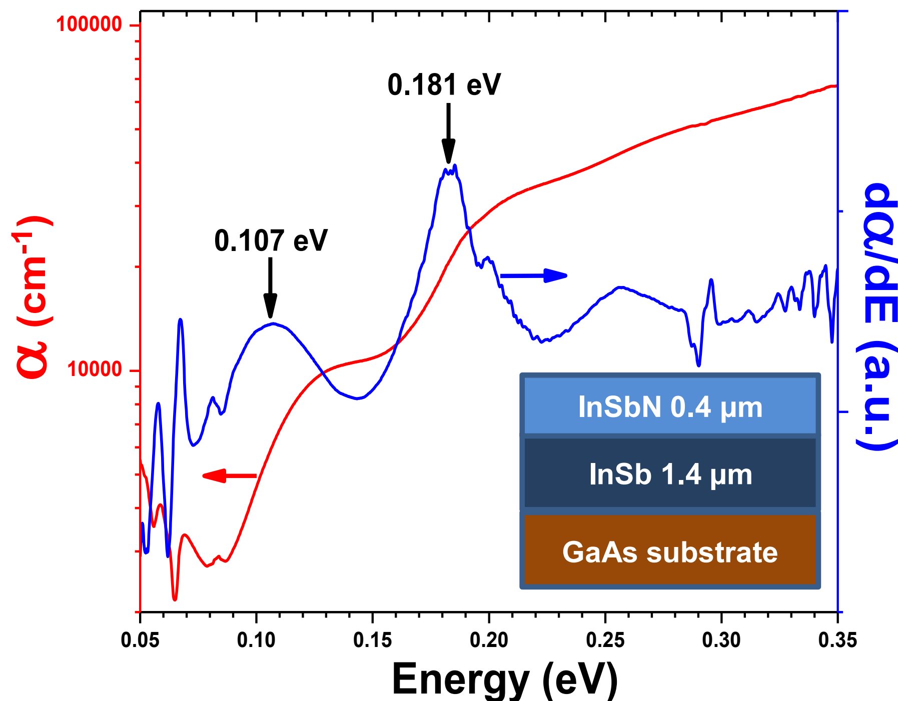

Figure 7.3. RT optical absorption edge for InSbN heterostructure annealed at 450 °C.

7.3 *In-situ* Annealing

Two 1.2 µm InSbN heterostructures grown at 290 and 380 °C on 0.2 µm InSb buffer were *in-situ* annealed at 430 ºC for a duration of 20 minutes. Figure 7.4 shows the (004) HRXRD scan of these in situ annealed heterostructures compared with a reference InSb epilayer. Both the

in-situ annealed InSbN heterostructures were observed to exhibit a positive mismatch w.r.t. the InSb reference peak. This can be either due to change in the lattice parameter due to the process of annealing and/or loss of N_{Sb}.

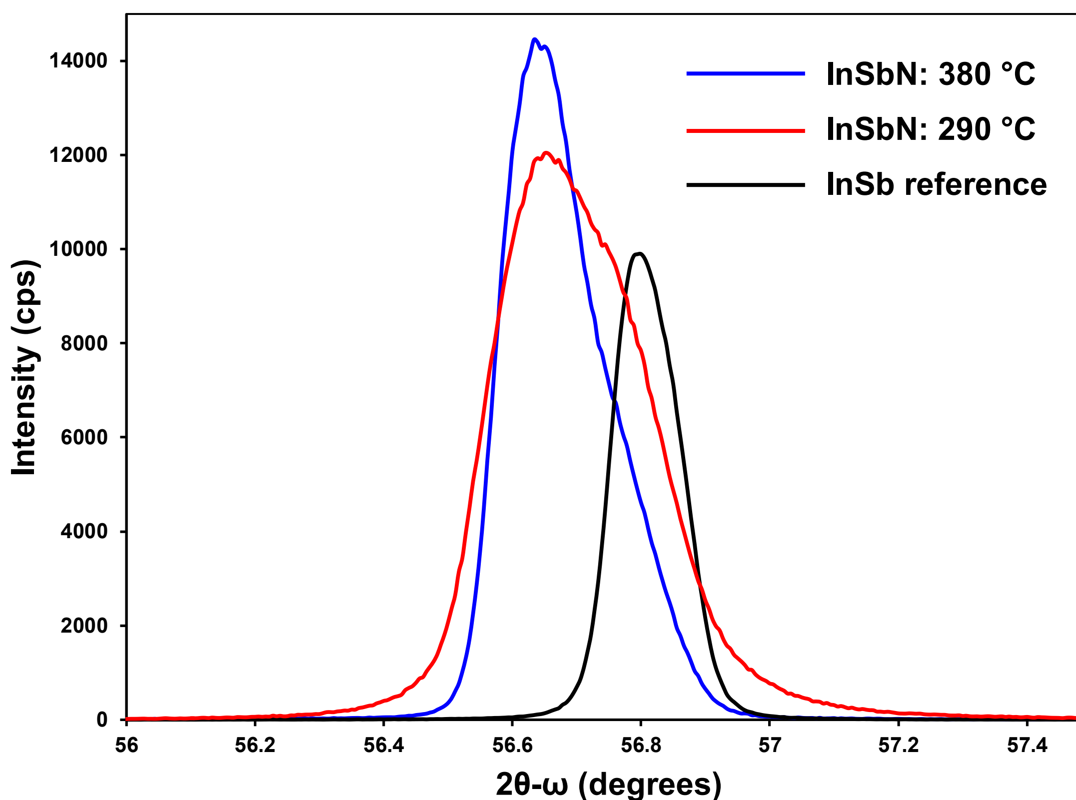

Figure 7.4. (004) HRXRD scan of *in-situ* annealed InSbN heterostructures annealed at 430 ºC.

Further, the heterostructure grown at 290 ºC observed to exhibit a relatively higher FWHM as compared to the structure grown at 380 °C. The broadening of this HRXRD peak is believed to be due to either presence of heteroepitaxial dislocations or mosaic spread rather than N-related defects, as annealing has been reported[93, 134] (also discussed further in this Chapter) to reduce the lattice crystal disorder arising from N incorporation. A detailed study of these dislocations using RSM technique has been presented in Chapter 8. Figure 7.5 shows the RT absorption spectra of these *in-situ* annealed InSbN heterostructures compared with the InSb reference layer. Although it is very difficult to estimate the band gap due to the interference of

the Fabry Perot fringes, a clear red shift in the absorption edge in case of both InSbN samples w.r.t. InSb indicate a fundamental band gap reduction. The RT Hall measurement for these *in-situ* annealed heterostructures was found to vary with growth temperatures. In case of the InSbN heterostructure grown at 290 °C, the n was observed to 1.6×10^{16} cm^{-3} and μ 12,600 cm^2/Vs. Whereas, in case of the InSbN heterostructure grown at 380 °C, the n was observed to be 1.4×10^{17} cm^{-3} and μ 7,200 cm^2/Vs.

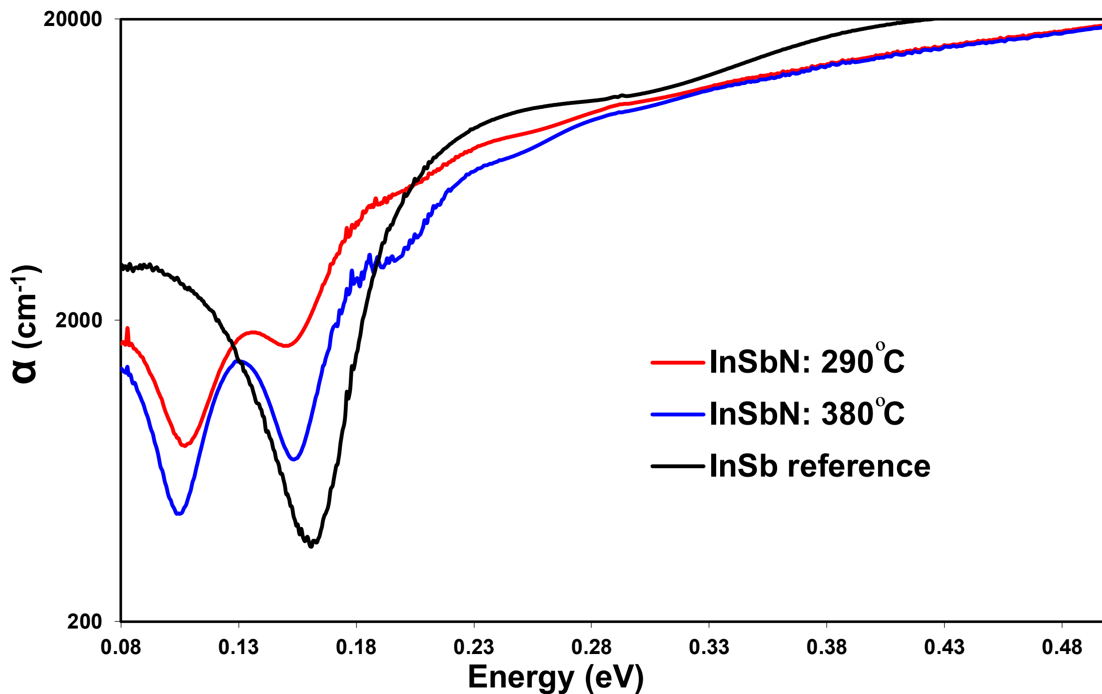

Figure 7.5. RT absorption spectra of *in-situ* annealed InSbN heterostructures.

From the previous two sections it can be concluded that annealing at higher temperatures 430 ~ 450 °C observed to reduce background n and increase carrier μ in the InSbN epilayers. However, in order to see a considerable change in the material property the duration of annealing was observed to be dependent on the technique of annealing. Hence, a comparative study of these two annealing techniques has been presented in the following section for two InSbN heterostructures grown under similar growth conditions and annealed by two different techniques at same annealing temperature but for different durations.

7.4 Comparative Study of *Ex-situ* and *In-situ* Annealing

The InSbN heterostructures used for this study were 2 µm thick, grown at ~290 ºC on a 0.2 µm InSb buffer layer. Both *ex-situ* and *in-situ* annealing was carried out at 430 ºC for 3 and 20 minutes, respectively. The choice of the annealing temperature and corresponding duration was made from the above annealing results, after observing the most effective annealing condition in each case which results in a considerable reduction in n and increase in μ.

7.4.1 HRXRD. A (004) HRXRD scan of the *as-grown* InSbN heterostructure as shown in Figure 7.6, exhibits a buffer InSb peak and a distinct InSbN peak to the right at 57.17°, with FWHM 280 and 342 arcsec, respectively. However, for both the *ex-situ* and *in-situ* annealed InSbN epilayers, the nitride peak was observed to be positively mismatched with respect to the InSb peak. The corresponding FWHM of the *ex-situ* and *in-situ* annealed InSbN epilayers were observed to be 348 and 320 arcsec, respectively.

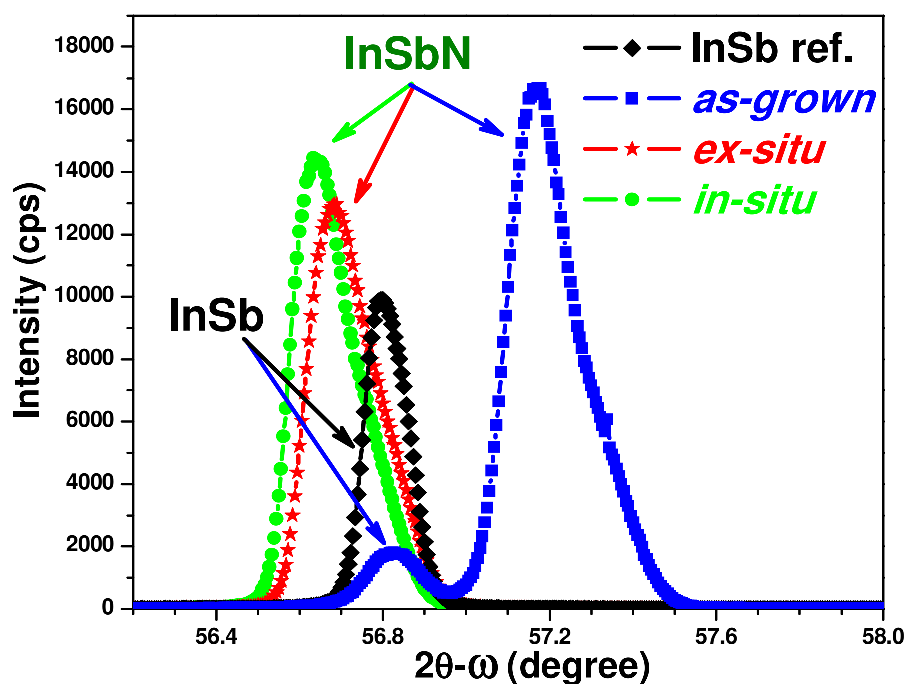

Figure 7.6. Plot of (004) HRXRD scan for the InSb reference, *as-grown*, *ex-situ* and *in-situ* annealed InSbN epilayers.[134]

All the epilayers were found to be 100 % relaxed based on the mismatch values determined from symmetric (004) and asymmetric (115, not shown here) HRXRD scans. These FWHM values of the nitride epilayers grown on single step InSb buffer are comparable to those reported by Lim et al,[82] grown on a two-step InSb buffer layer. We speculate that the annealing of the InSb buffer layer at higher temperatures prior to the growth of InSbN epilayer helps mitigate the dislocation density, thereby serving the purpose of a two-step buffer. The reduction in threading dislocation density with increase in epitaxial layer thickness and annealing in the highly lattice mismatched heteroepitaxial semiconductors[47, 135-138] is commonly attributed to the creation of half loops caused by the coalescence of threading dislocations.[136, 137] The dislocation density in the reference InSb and InSb buffer layers estimated (using Equation 3.1) to be in the low 3-5x10^8 cm^{-2} range and was higher in the 8x10^8 cm^{-2} range for the InSbN epilayers. The estimated dislocation density for the InSb buffer is observed to be 3 folds lower than the reported values[58] for similar thickness of InSb grown on GaAs . It is to be pointed out that these dislocation values may be underestimated as these are based on (004) HRXRD broadening only, which is more sensitive to screw/angular dislocations.[139] The dislocation density values estimated here for the InSbN samples are slightly higher than our earlier (in Chapter 6) estimated values,[30] due to reduction in the thickness of InSb buffer layer.

An excellent fit of the simulated HRXRD data to the experimental (004) scan data was obtained with an N incorporation of 2.5±0.2 % for the *as-grown* InSbN epilayer, considering all the InSbN epilayers were 100 % relaxed. These InSbN layers were confirmed to be 100 % relaxed from the corresponding reciprocal space map studies which has been presented in details in Chapter 8. In the case of the annealed epilayers, the nitride layer peak shifts to the left of the InSb peak and hence the computation of N incorporation from the (004) HRXRD scan poses a

challenge. N % from SIMS (Figure 7.7) were determined to be 2.6±0.5 %, 1.2±0.2 % and 0.8±0.2 % for *as-grown*, *ex-situ* and *in-situ* annealed epilayers, respectively. A very less difference in these two N % values in *as-grown* epilayer indicate the presence of N maximum in the substitutional sites than interstitial sites.[88] Further, this attests to the NRA study of the *as-grown* epilayer, which confirmed at least 85 % of N to be in the substitutional site. Notably, the N % determined from the HRXRD mismatch assumes only the presence of substitutional N atoms (N_{Sb}) and therefore the mismatch/strain due to the presence of interstitials provide considerable inaccuracy in the determination of the N % using a simple Vegard's law calculation. Depending on the type of interstitials involved, it can provide either lattice dilation or contraction.[81] In view of this, the only inference that could be drawn is that the *as-grown* epilayer exhibits a much higher N concentration in the substitutional than interstitial sites similar to the annealed epilayers. In the case of annealed epilayers the positive mismatch is attributed to the loss of N_{Sb}[47] and the presence of Sb–N interstitials leading to compressive strain.[81]

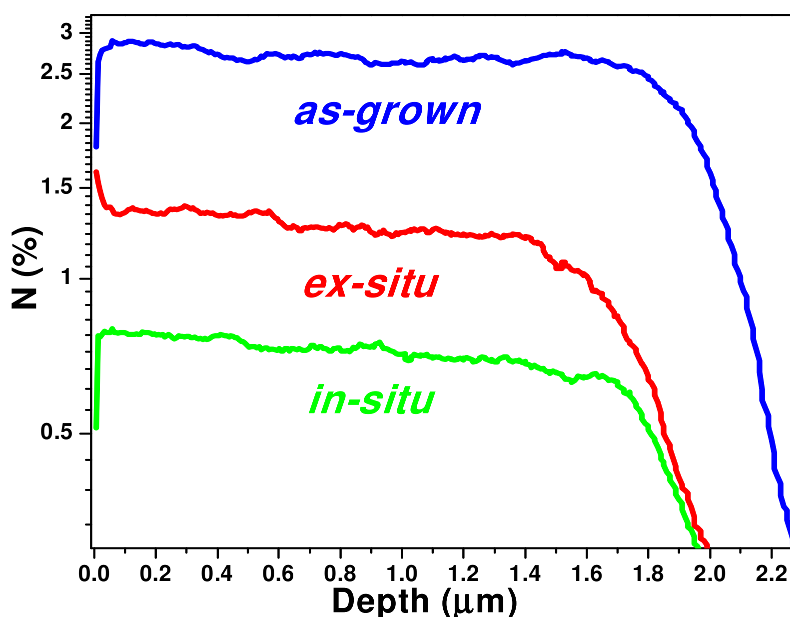

Figure 7.7. SIMS depth profile of *as-grown*, *ex-situ* and *in-situ* annealed InSbN heterostructures grown at 290 °C.

7.4.2 Micro-Raman spectroscopy. Figure 7.8 (a) shows a comparison of RT micro-

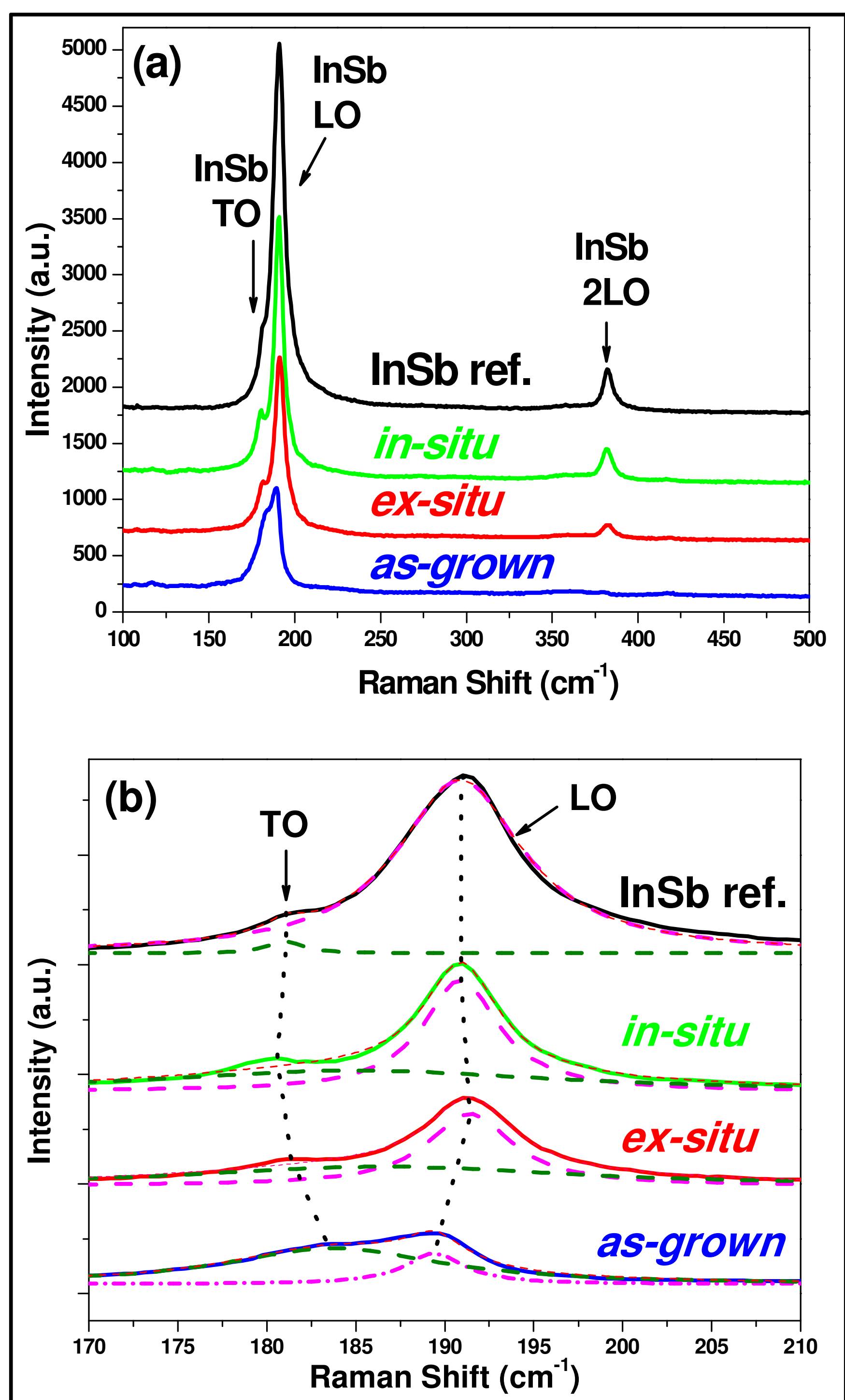

Figure 7.8. (a) The RT micro-Raman spectra of *as-grown*, *ex-situ* and *in-situ* annealed InSbN epilayers compared with the InSb reference and (b) Lorentzian fit for the RT micro-Raman spectra in the 1st order InSb TO and LO phonon range for the spectra illustrated in (a). [134]

Raman spectra of InSb reference along with all the InSbN epilayers. Figure 7.8 (b) exhibits the Lorentzian fit to the different peaks observed in the corresponding spectra. The dotted line indicates the shift in TO and LO peaks for the InSbN epilayers. All of the spectra exhibit LO and TO phonon modes of InSb at 191 cm^{-1} and 181 cm^{-1}, respectively.[116] In the reference InSb epilayer, well-defined first and second order LO phonon modes (382 cm^{-1}) along with a weak TO phonon mode of InSb are observed, attesting to the high crystalline quality of the InSb reference epilayer.[116] Reduction in the InSb LO peak as well as its nonsymmetrical shape, absence of 2LO modes along with the appearance of the forbidden InSb TO phonon mode at 183 cm^{-1}, are all characteristics of the *as-grown* InSbN epilayers, while the annealed epilayers exhibit a significantly higher peak ratio of InSb LO/TO (I_{LO}/I_{TO}) (Table 7.1) with an increase from 0.8 to 7.1 and reappearance of 2LO modes attesting to the good quality of these epilayers.

Table 7.1

SIMS N %, Raman I_{LO}/I_{TO}, RT and 77 K carrier concentration (n) and mobility (μ) data for the as-grown, ex-situ and in-situ annealed InSbN epilayers.

InSbN epilayer	SIMS N (%)	Raman I_{LO}/I_{TO}	n_{RT} (cm^{-3})	μ_{RT} (cm^2/V-s)	n_{77K} (cm^{-3})	μ_{77K} (cm^2/V-s)
As-grown	2.6±0.5	0.8	1.0×10^{18}	3,300	1.2×10^{18}	3,200
Ex-situ annealed	1.2±0.2	4.4	2.0×10^{16}	12,000	8.4×10^{15}	6,000
In-situ annealed	0.8±0.2	7.1	1.5×10^{16}	13,000	4.8×10^{15}	7,100

In light of the above HRXRD, SIMS and Raman data, the following qualitative explanations of the variations observed between the *as-grown* and annealed epilayers are

provided. *As-grown* epilayer have large N %, both in substitutional as well as interstitial sites as discussed above, leading to the degraded quality of the epilayer due to the N induced lattice disorder, as evidenced from Raman spectra. On annealing, improvement in the quality of the epilayer is consistent with those commonly observed in other dilute nitride systems[131, 132] and have generally been attributed to the annihilation of N- related defects. Further, a well-resolved TO peak in *in-situ* annealed epilayer provides strong evidence of N being incorporated in the substitutional sites[30] as well. *In-situ* annealed epilayer exhibited relatively higher HRXRD intensity and high I_{LO}/I_{TO} in the corresponding Raman spectra compared to *ex-situ* annealed epilayer, indicative of good ordering in the InSb lattice structure. This is consistent with our group's prior annealing studies[14,15] carried out on other dilute nitride systems, where we find that the *in-situ* annealing leads to efficient annihilation of N related defects and improved bonding in comparison to the *ex-situ* annealing. Note that the InN TO or LO phonon modes reported by Lim et al[93] were not observed in our InSbN epilayers, due to the low cross section for In-N phonon scattering in conjunction with the resonant frequency far from the exciting line used in this study.[116] The absence of any low energy peak corresponding to A_{1g}Sb elemental mode, reported in the growth of InSbN by Lim et al,[88] indicates minimal Sb antisite defects in our epilayers.

7.4.3 Hall measurement. Hall measurements were carried out at both RT and 77 K. The electrical transport parameters thus determined are listed in Table 7.1. These epilayers were found to be n-type. No significant changes in values were observed with variation in applied magnetic field, suggesting a negligible magneto-resistance effect as compared to InSb. These values reflect the true electrical properties of InSbN, due to a relatively thick InSbN epilayer in these heterostructures. The reference InSb epilayer exhibited an intrinsic carrier concentration (*n*) of 2.6×10^{16} cm^{-3} and mobility (μ) 38,000 cm^2/V-sec at RT. At 77 K, both *n* and μ of the *as-*

grown InSbN epilayers were not significantly altered. However, in the annealed epilayers at 77 K reduction in both n and μ with respect to their RT values were observed, though μ of the annealed epilayers remained higher than those of the *as-grown* epilayers. The variation in the μ data can be explained using the temperature dependence of three dominant scattering mechanisms present in the layers, namely, lattice (phonons), ionized impurity and lattice defects/dislocations. The high n and low μ values observed in the *as-grown* InSbN epilayer at both RT and 77 K is consistent with our earlier conjecture of N interstitials as well as poor quality of the *as-grown* epilayer. The donor nature of N-interstitials and their energy levels being higher[73] than the host lattice conduction band minimum (CBM) further explains the invariant nature of high n observed both at RT and 77 K in the *as-grown* InSbN epilayer. The reduction in RT n on annealing is therefore attributed to the annihilation of N-interstitials and N-related defects. A further reduction in n at 77 K observed only for the annealed epilayers is most likely due to partial freeze-out of the carriers. The origin of the shallow donors is speculated to be Sb antisites. Although Sb antisite was observed to be below the detection limit for our samples in their Raman spectra, they are believed to be present as a congruent process of annealing and formation of Sb-N as reported by Lim et al[28, 93] The increase in μ on annealed epilayers can be correlated predominantly to the reduced phonon scattering at RT due to the improved quality of the layers as attested by the Raman spectra. At 77 K, due to the estimated dislocation density being in the high 10^8 cm^{-2} range, the contribution from dislocation scattering becomes comparable to the ionized impurity scattering for the carrier concentration in the 10^{16} cm^{-3} range, as per the deformation potential model of Dexter-Seitz.[140] So though the lattice scattering contribution decreases with temperature, the mobility remains low due to the contribution of the above two scattering mechanisms. Further, the highest μ observed for the *in-situ* annealed InSbN

attest to the maximum I_{LO}/I_{TO} ratio observed in the corresponding Raman spectra. These are the best mobility values for both *ex-situ* and *in-situ* annealed InSbN on GaAs reported to date. These characteristics of the annealed InSbN epilayers correlate to the loss of N both from the epilayer and bulk (Figure 7.7). The phenomena of N loss from the epilayer and bulk after annealing are believed to be assisted by dislocation and/or interstitial diffusion.[95, 141]

7.4.4 FTIR. Figure 7.9 displays the RT absorption spectra of these epilayers determined from the FTIR measurements. The annealed epilayers are observed to exhibit an overall lower absorption coefficient in the wavelength region investigated. All the nitride epilayers display a red shift in their corresponding absorption edge E_{abs} with respect to the InSb reference layer.

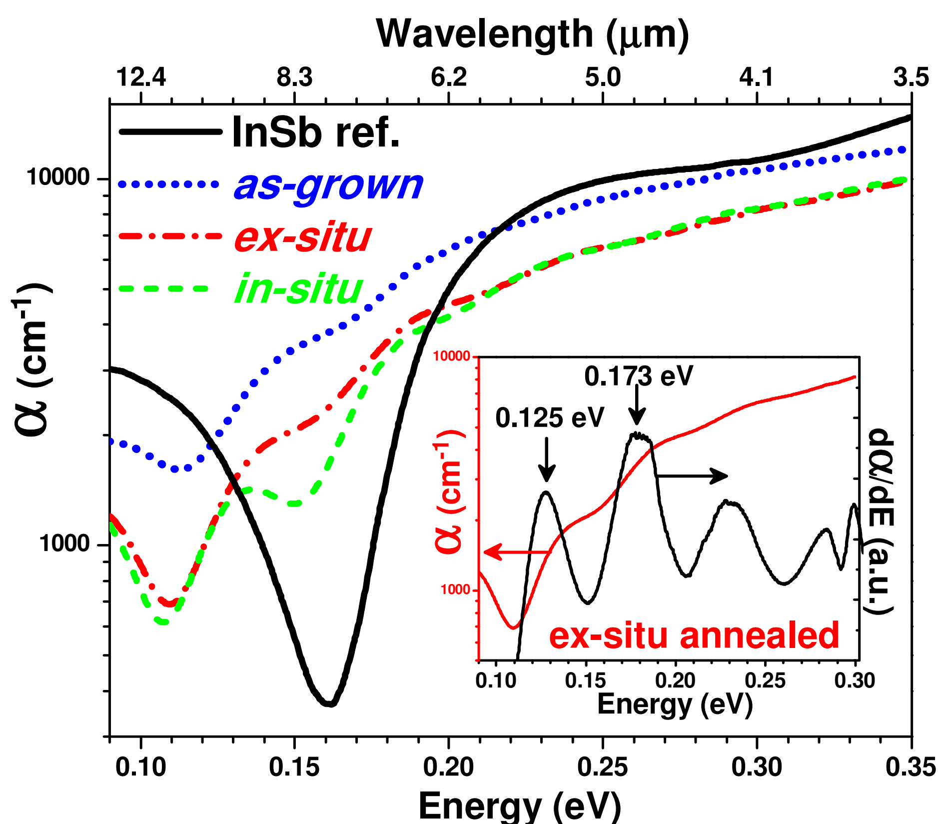

Figure 7.9. The RT absorption coefficient (α) vs energy (eV) plot for *as-grown*, *ex-situ* and *in-situ* annealed InSbN epilayers along with the InSb reference. The inset shows the first order derivative of α vs eV for the *ex-situ* annealed InSbN epilayer.[134]

As shown in the inset of Figure 7.9, the peak observed at 0.125 eV (9.9 µm) in the *ex-situ* annealed layer has been assigned to the *ex-situ* annealed nitride epilayer E_{abs} while the other peak at 0.173 eV (7.2 µm) is close to the InSb band gap. The E_{abs} determined similarly for InSb reference, *as-grown* InSbN and *in-situ* annealed epilayers were estimated to be 0.19 (6.5 µm), 0.132 (9.4 µm) and 0.12 (10.3 µm) eV, respectively. The somewhat higher absorption edge determined for the InSb reference epilayer as compared to InSb buffer is most likely due to the high carrier-concentration-induced Moss Burstein shift, because the reference epilayer did not undergo any high temperature annealing after the growth as the buffer layer of all the nitride epilayers. The Moss-Burstein shift for the *as-grown* InSbN due to high *n*, estimated (using Equation 3.3) to be 0.137 eV, which leads to the original bandgap being a negative $E_g = -0.004$ eV corresponding to a theoretical estimation of 2.6 % N incorporation.[70] This estimated N is in excellent agreement with the observed HRXRD and SIMS N %. In addition, the lowest absorption coefficient observed in the annealed epilayers before the onset of free carrier absorption is found to be half the magnitude of the *as-grown* epilayer occurring at 0.11 eV. The low absorption coefficient and relatively fast roll-off observed below E_o (Figure 7.9) achieved in these annealed epilayers attest to the reduction in localized band-tail states due to N induced defects, consistent with the above Raman and Hall measurement data. In addition, the distinct absorption minima with a relatively lower width Urbach tail observed at 0.15 eV only in the *in-situ* InSbN epilayer again attest to the improved Raman spectra as well as the best Hall μ values obtained in this epilayer. Further, the SIMS data for this epilayer is also in good agreement with the 0.7 % N value predicted using the k.p model by Murdin et al[70] on InSbN, corresponding to the optical bandgap of 0.12 eV exhibited by this sample. Hence, all the above results indicate that the substitutional N in InSbN resulted in the band gap reduction as theoretically predicted.

7.5 Conclusion

InSbN heterostructures were annealed *ex-situ* by RTA and *in-situ* after the growth in the MBE chamber. Along with the annealing temperature the duration of annealing was observed to affect electrical property of the epilayers. The annealing temperature of 430 ºC was found to be effective for a high quality InSbN epilayers. The *as-grown* InSbN epilayer revealed high N incorporation in the substitutional, high N-induced defects, high background carrier concentration and low carrier mobility. Although a negative band gap was estimated corresponding to a high 2.6 % N incorporation, the Moss-Burstein effect due to high *n* observed lead to blue shifting of the absorption edge up to 0.132 eV. The annealed epilayers show significant improvement in the quality of the layers, attributed to the effective annihilation of N related defects and dislocations in the layer, with the red shift in the absorption edge to 0.12-0.125 eV. The improved quality of the layers is attested by a reduced InSb TO peak and the presence of InSb LO and 2LO peaks in the Raman spectra and enhanced carrier mobility as high as ~10,000 cm^2/V-s. A reduction in InSb Urbach tail width in the absorption spectra of *in-situ* annealed InSbN has been correlated to enhanced InSb crystalline quality and reduction in dislocation density due to annealing. A relatively longer duration of *in-situ* annealing was observed to be more effective in increasing μ as compared to *ex-situ* by RTA when annealed at same temperature. However, the best absorption cutoff ~11.6 µm was observed for InSbN annealed at 450 °C with n ~$5x10^{16}$ cm^{-3} and μ ~42,300 cm^2/V-s. Thus, these preliminary data show great promise for extending the absorption edge in this material system up to 14 µm through optimization of annealing conditions.

CHAPTER 8

Study of Defects in InSbN Heterostructures

8.1 Introduction

Defects in InSb grown on GaAs[41, 42, 119] and Ge[110] substrates have been extensively studied and very well established for highly mismatch semiconducting alloys. In order to fabricate a semiconducting device for a high efficiency operation, the defects in the device need to be minimized. Hence, study of defects in InSbN epilayers plays a very important role for a high performance detector fabrication. Since, InSbN epilayer is subsequently grown on InSb buffer our preliminary results indicated that the quality of InSbN epilayer is greatly affected by the quality of the InSb buffer. Hence, in addition to the defects due to N incorporation, the effect of heteroepitaxy on the quality of InSbN needs to be investigated. In order to observe the effect of heteroepitaxial defects on the InSbN epilayer, InSbN heterostructures with different InSb buffer thicknesses were grown without changing any growth parameter for both InSb and InSbN. In addition to observe the effect of InSbN epilayer thickness on its layer quality and N incorporation, heterostructures with different InSbN epilayer thickness has also been studied with the InSb buffer layer thickness being invariant. In this Chapter the study of overall structural quality of the heterostructure using HRXRD and RSM techniques and correlation with its thickness and alloy composition is reported.

8.2 Experimental Details

Four sets of InSbN heterostructures were used for a systematic study of the effect of InSb buffer thickness and InSbN epilayer thickness on the quality of grown InSbN epilayer in the heterostructure. The heterostructures of 1.2 µm InSbN/ 1.4 µm InSb/ GaAs, 0.4 µm InSbN/ 1.4 µm InSb/ GaAs, 0.4 µm InSbN/ 0.2 µm InSb/ GaAs and 2 µm InSbN/ 0.2 µm InSb/ GaAs are

referred to as S1, S2, S3 and S4, respectively. A 0.6 µm thick InSb layer on GaAs was used as a reference. All the grown parameters of both InSbN and InSb epilayers were kept same for all the four heterostructures except the individual layer thickness. All the InSbN epilayers were grown at 290±10 ºC.

8.3 Results

Figure 8.1 shows the (004) HRXRD plot of the four InSbN heterostructures S1, S2, S3 and S4 along with InSb reference. The peaks observed at ~ 56.8° in case of all the heterostructures correspond to InSb buffer layer and the peaks on the right of InSb around 57.2±0.2° correspond to the InSbN epilayer. The FWHM values and intensity of the individual HRXRD peaks have been used to compare the quality of the corresponding layers in these heterostructures.

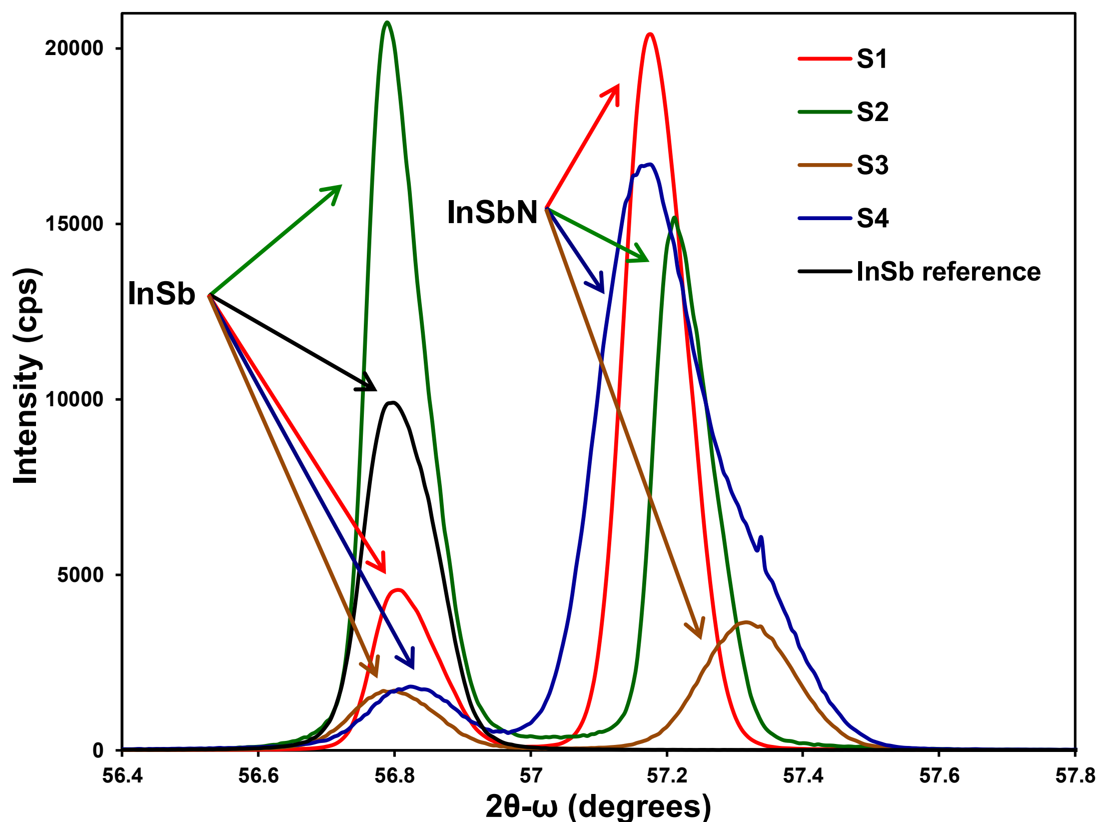

Figure 8.1. (004) HRXRD of four different InSbN heterostructures along with InSb reference.

In order to study the effect of threading dislocations on the quality of heterostructures, asymmetric scans were performed in (115) plane for all the test samples. Figure 8.2 shows the (115) HRXRD scan performed in the glancing incidence configuration. All the plots are aligned to InSb peak at 0 arcsec, as InSb is 100 % relaxed due to a very large lattice mismatch w.r.t. the GaAs substrate. The peaks on the right of InSb around 1000~1500 arcsec correspond to InSbN epilayer. The FWHM values of individual peaks were measured from both (004) and (115) scans and recorded in Table 8.1. Although all the InSbN epilayers in these heterostructures were grown at same growth temperature, the variation observed in the (115) peak position of the nitride peaks is believed to be due to the variation in the parallel and perpendicular lattice mismatch values between these test heterostructures. The exact lattice mismatch values were estimated from the corresponding (115) RSM study and recorded in Table 8.1.

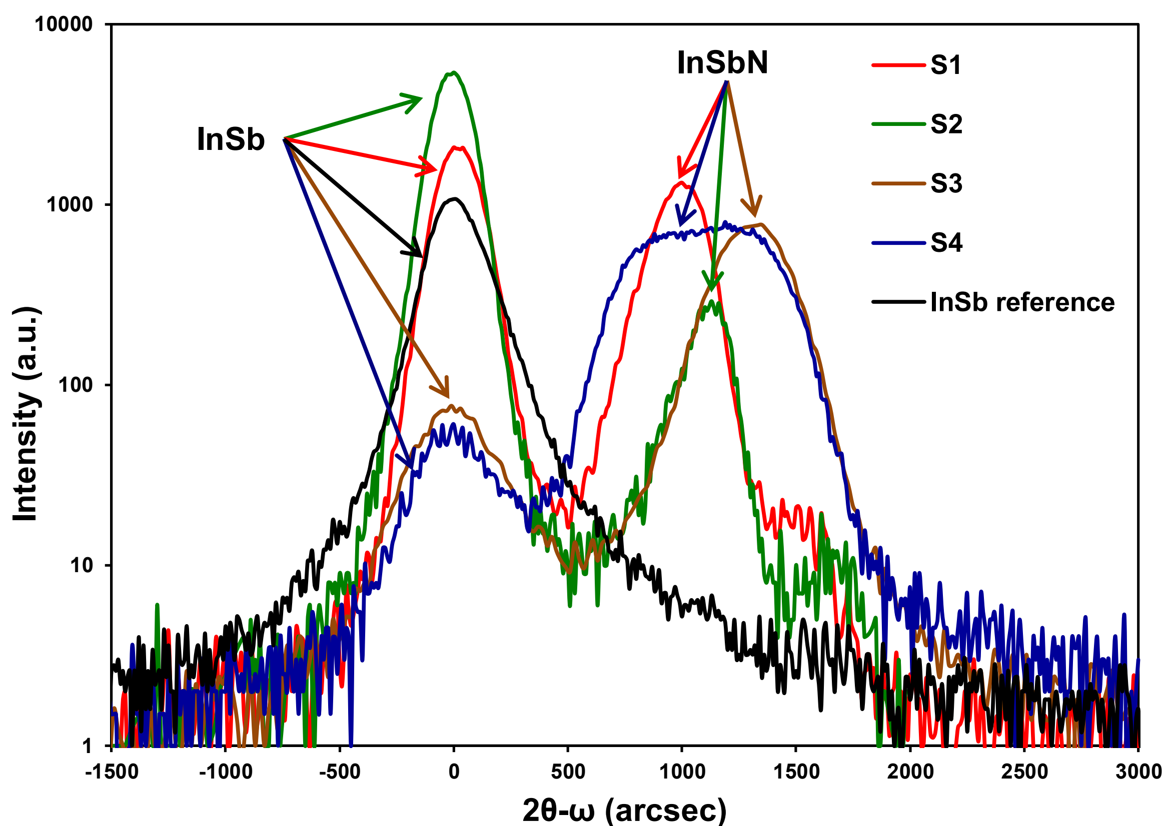

Figure 8.2. (115) HRXRD plot of four different InSbN heterostructures.

Table 8.1

(004) and (115) HRXRD FWHM of different InSbN heterostructures.

Common Features in the Heterostructures	InSbN Heterostructure	Layer Thickness (μm)		(004) FWHM (arcsec)		(115) FWHM (arcsec)		Parallel Mismatch (ppm)	Perpendicular Mismatch (ppm)
		InSb	InSbN	InSb	InSbN	InSb	InSbN		
Same InSb buffer (thick) →	S1	1.4	1.2	199	193	214	238	-370	-5691
Same InSbN epilayer →	S2	1.4	0.4	190	190	191	197	-294	-6895
Same InSb buffer (thin) →	S3	0.2	0.4	260	290	380	360	-3902	-7928
	S4	0.2	2	280	338	367	722	-4040	-5652

Reciprocal space map study was performed on all the four heterostructures to study the mismatch, strain/relaxation, tilt in the layers. Figure 8.3 shows the (115) glancing incident RSM contour plot of S1 along with the GaAs substrate peak. The individual peaks are labeled in the plot. Clearly the GaAs substrate observed to exhibit sharp Bragg reflection and the broad ones correspond to InSb buffer layer and InSbN epilayer. The parallel and perpendicular mismatch of InSb reciprocal lattice point (RLP) w.r.t. GaAs substrate was estimated to be 14.58 % and 14.73 %, respectively indicating 100 % relaxed InSb buffer layer. The parallel and perpendicular mismatch values for the InSbN epilayer w.r.t. InSb layer estimated from the plot are tabulated in Table 8.1. The lateral correlation length of InSb and InSbN was calculated to be 15,362 and 6,056 Å. A mosaic spread of 0.1° was estimated both for InSb and InSbN. The lattice constant values estimated for GaAs, InSb and InSbN were 5.655, 6.488 and 6.459 Å, respectively.

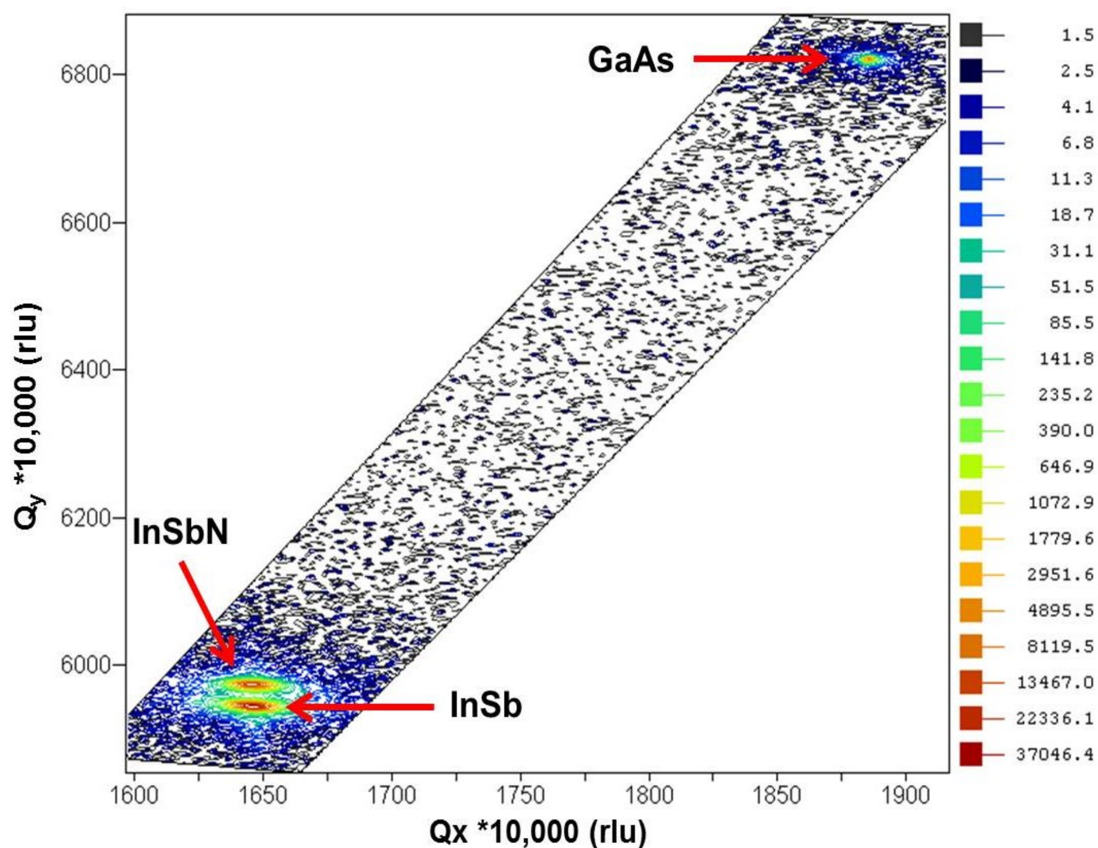

Figure 8.3. (115) reciprocal space map of heterostructure S1 along with GaAs peak.

Figure 8.4 shows the (a) (004) and (b) (115) RSM contour plot of S1showing only the InSb and InSbN RLPs. The vertical solid line indicates the surface normal. This line observed to cross through the center of both the RLPs in the asymmetric plot (Figure 8.4 (b)) which indicates the InSbN epilayer to be strained w.r.t. InSb buffer layer. This attests to the large difference observed in the parallel and perpendicular mismatch values estimated for the InSbN epilayer (Table 8.1).

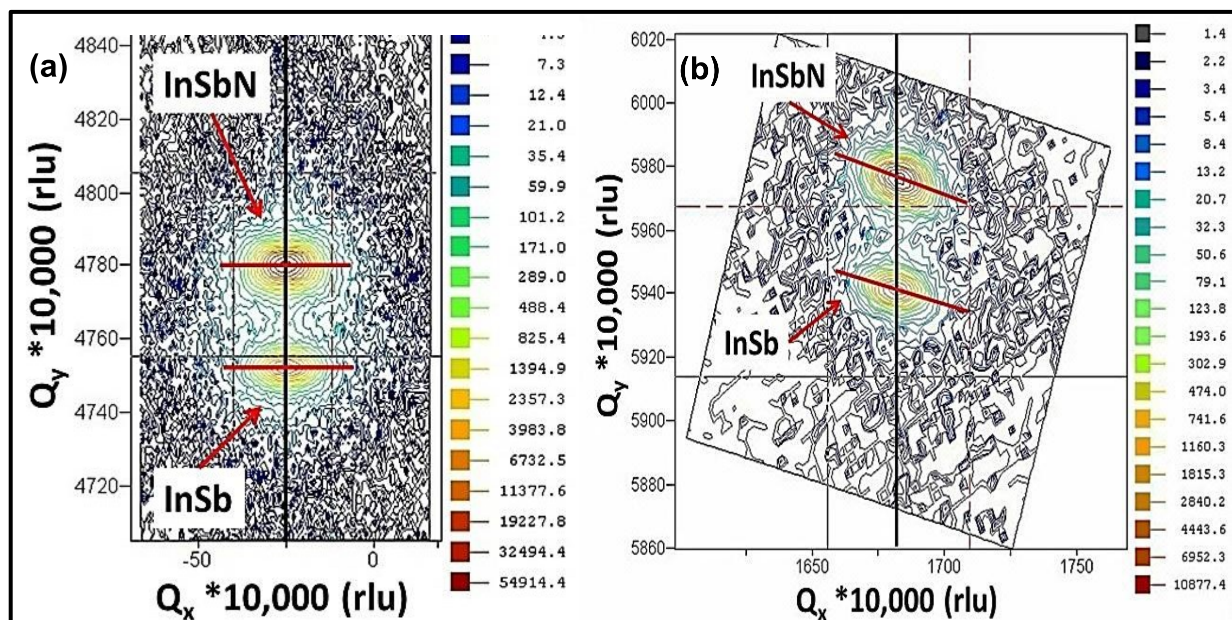

Figure 8.4. (a) (004) and (b) (115) reciprocal space maps of the heterostructure S1.

A similar behavior observed for the heterostructure S2. Figure 8.5 shows the (115) RSM of S2 where it can clearly be seen that the InSbN layer is strained to InSb layer even though there is a lattice mismatch in the nitride epilayer. The RLP spread along Q_X and Q_Y was observed to be same both for InSb and InSbN similar to S1. This indicates the observed quality of InSbN epilayer remains unchanged in these two heterostructures. The lateral correlation length for the InSbN epilayer was estimated to be 3073 Å. Further, a similar mosaic spread of 0.1° was estimated for the InSbN epilayer. In this case the lattice constant of InSb and InSbN epilayer was estimated to be 6.487 and 6.445 Å, respectively.

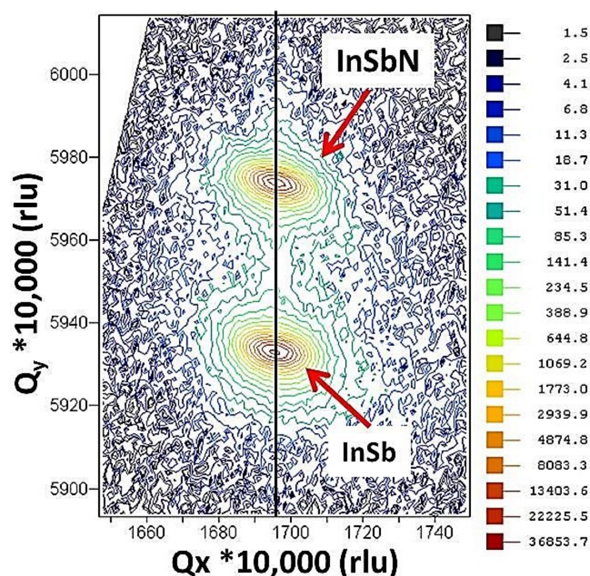

Figure 8.5. (115) reciprocal space map of the heterostructure S2.

Figure 8.6 shows the (a) (004) and (b) (115) RSM plots of S3. It can clearly be seen that in the asymmetric scan (Figure 8.6 (b)) the surface normal not crossing through the center of InSbN RLP, indicating the layer to be relaxed as compared to S1 and S2. However, a large difference in the mismatch values (Table 8.1) indicates only a partial relaxation. The lattice constant of InSb and InSbN epilayer were estimated to be 6.485 and 6.434 Å, respectively.

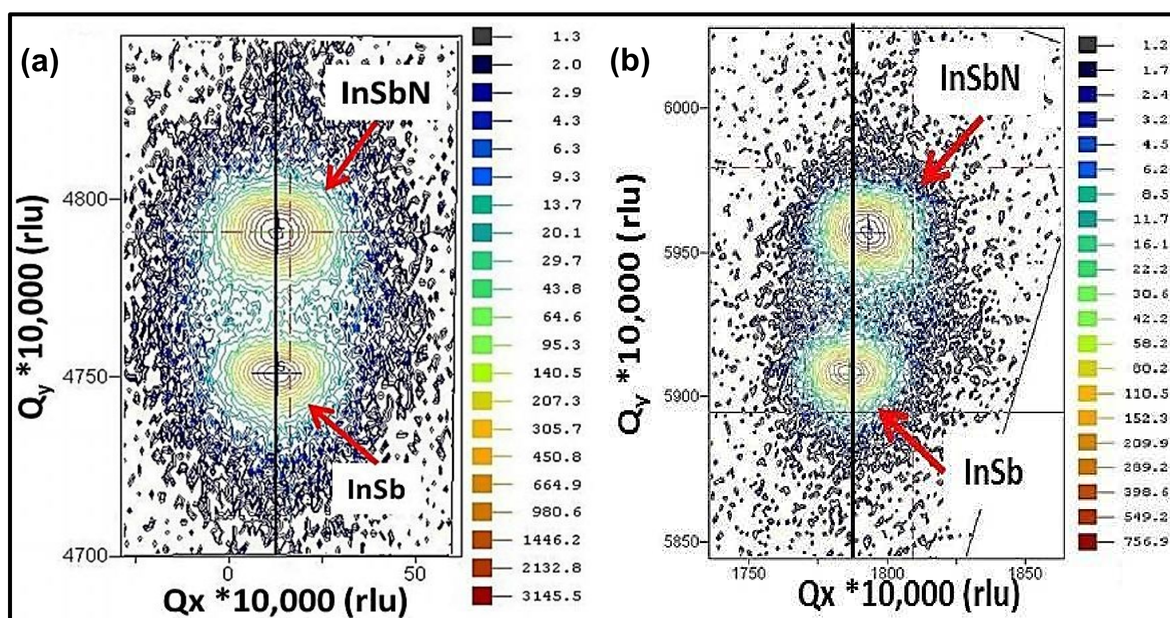

Figure 8.6. (a) (004) and (b) (115) reciprocal space maps of the heterostructure S3.

Figure 8.7 shows the (a) (004) and (b) (115) RSM plot for S4 heterostructure. As the InSb buffer layer is very thin, a low intense and broad InSb RLP was observed both in symmetric and asymmetric RSM plots. The InSbN RLP was observed to be relatively broad as compared to all other heterostructures with a unique triangle like broadening feature. The vertex of the triangle in Figure 8.7 (a) and (b), connecting three distant points on a contour line has been marked for a guide to the eye. This asymmetric spread along the surface normal with a relax-mosaic triangle (RMT) feature was observed to be similar to the RMT feature reported in the literature for ZnSe on GaAs.[142] This indicates the InSbN layer to be 100 % relaxed with a relatively high mosaic spread. The lattice constants for the InSb and InSbN epilayer in this heterostructure S4 were estimated to be 6.487 and 6.451 Å, respectively.

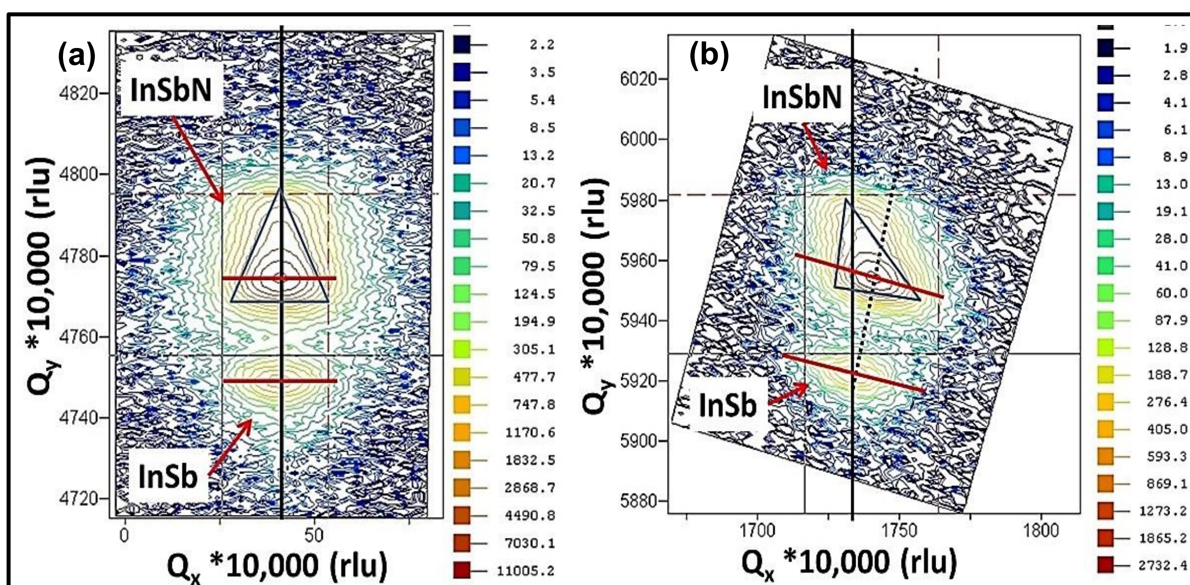

Figure 8.7. (a) (004) and (b) (115) reciprocal space maps of the heterostructure S4.

Figure 8.8 shows the contour plot of (115) RSM of the heterostructure S2 after *ex-situ* annealing at 450 °C for 45 secs. The individual peaks are labeled inside the plot. The GaAs RLP can easily be identified with its high intensity and sharp peak. The lattice constant estimated to be 5.655 Å which matches with the GaAs bulk lattice constant. The broad RLP has been

identified to be a combination of InSb and InSbN with an estimated lattice constant of 6.486 Å. The perpendicular and parallel mismatch was estimated to be 14.4 and 14.7 %, respectively w.r.t. the GaAs substrate.

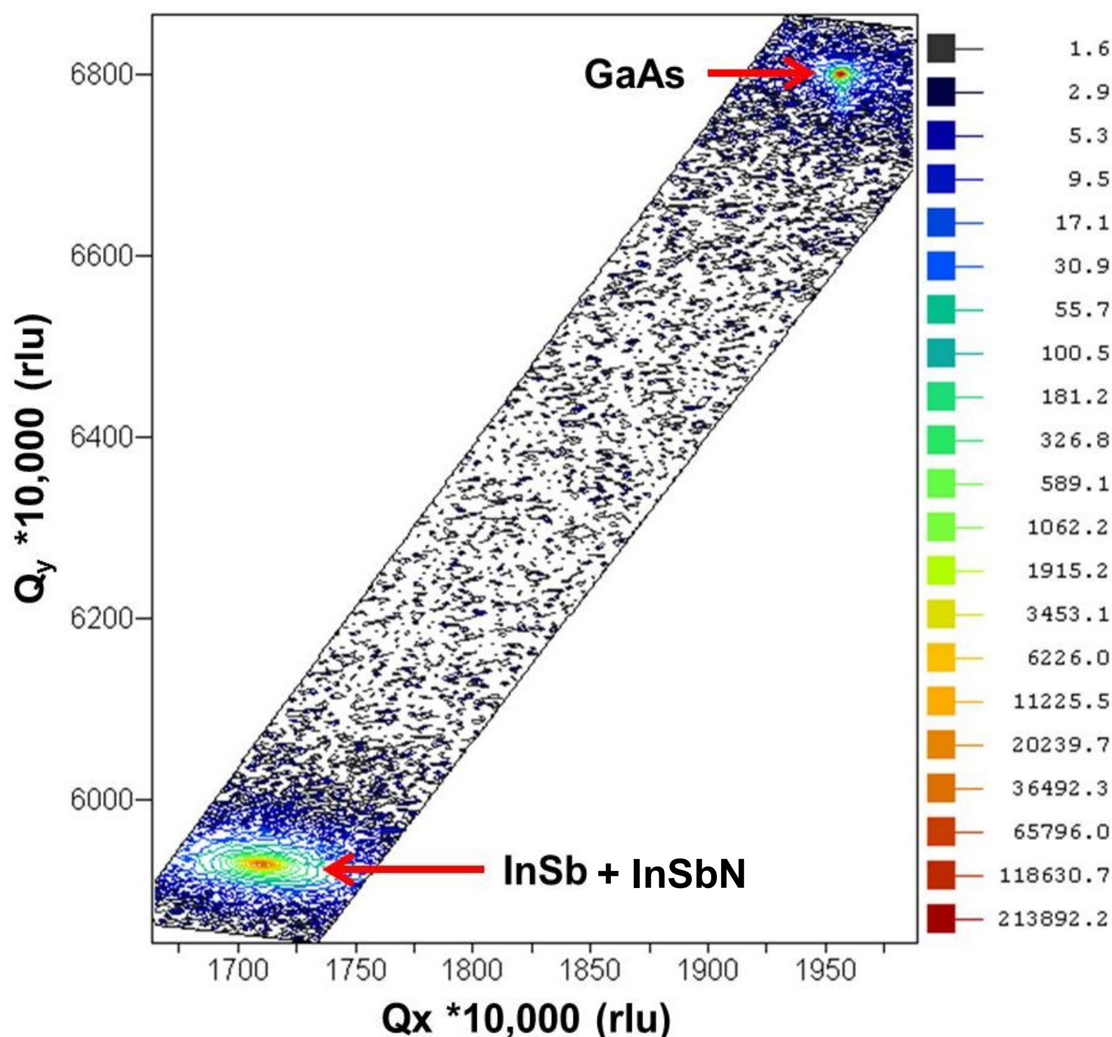

Figure 8.8. (115) reciprocal space map of the heterostructure S2 after *ex-situ* anneal at 450 °C.

Figure 8.9 shows the (a) (004) and (b) (115) RSM contour plots of the heterostructure S4 after *in-situ* annealing at 430 ºC for 1200 sec. Figure 8.10 shows the (004) RSM contour of the heterostructure S4 after *ex-situ* annealing at 430 ºC for 180 sec. The peaks are identified to be InSbN RLPs. A spread along Q_X and Q_Y observed in the InSbN RLPs similar to the spread observed in the InSbN RLP in *as-grown* S4 (Figure 8.7).

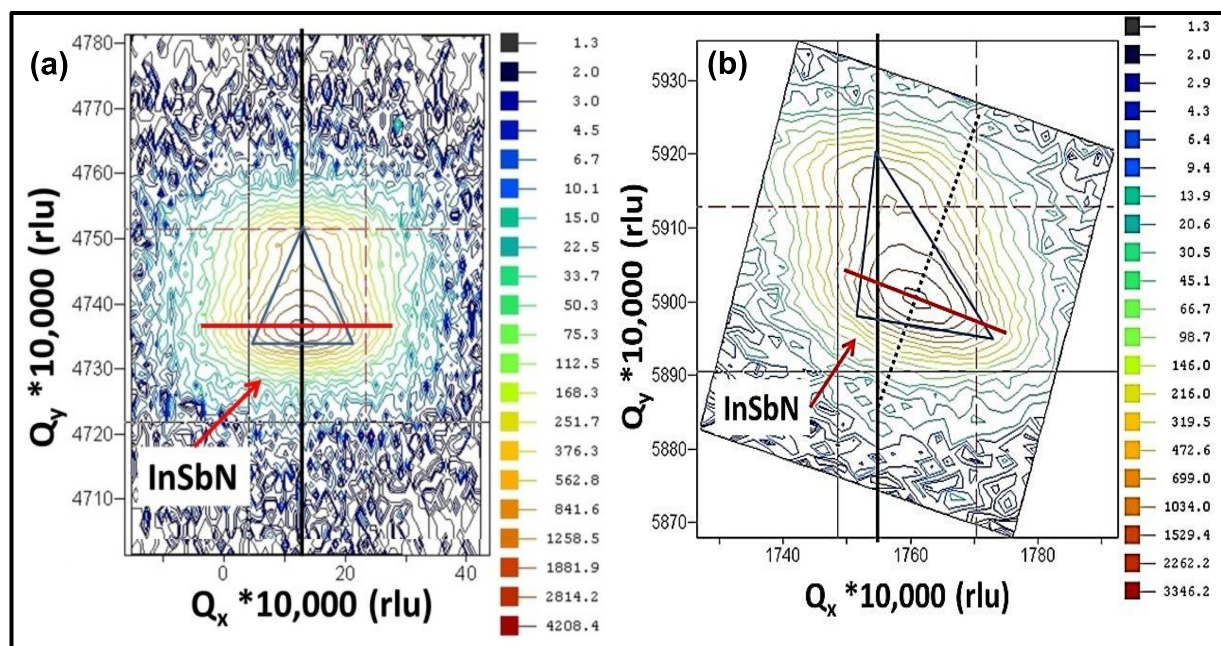

Figure 8.9. (a) (004) and (b) (115) reciprocal space maps of the heterostructure S4 after *in-situ* anneal at 430 ºC.

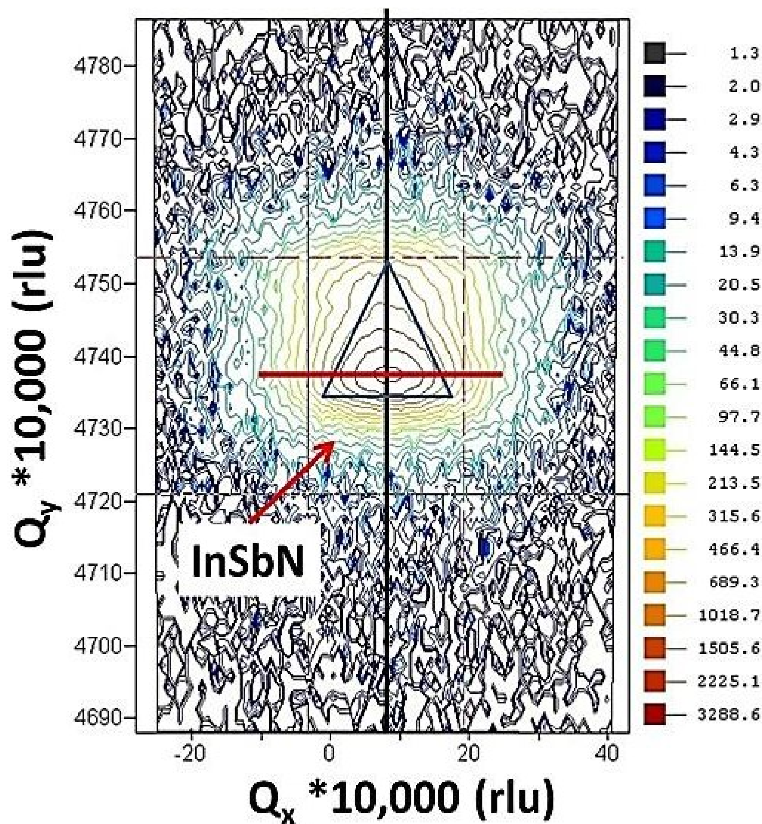

Figure 8.10. (004) reciprocal space map of the heterostructure S4 after *ex-situ* anneal at 430 ºC.

In order to study the variation in electrical property of different heterostructures, RT Hall measurements were carried out both at high magnetic field (5.8 kG) and low magnetic field (0.5 kG). Figure 8.11compares the RT n and μ of all the four heterostructures. The lines used to connect the data points are just a guide to the eye. Almost no change in n observed for S1 and S2, whereas a linear increase in n was observed for S3 and S4. In case of S1 and S2 a great reduction in the RT μ observed with increase in applied magnetic field whereas the RT μ was observed to be almost invariant with change in magnetic field for S3 and S4. However, an overall reduction in RT μ with a corresponding increase in RT n was observed for both S3 and S4 as compared to S1 and S2. The InSbN heterostructure S4 was observed to exhibit the highest n and least μ as compared to all the heterostructures.

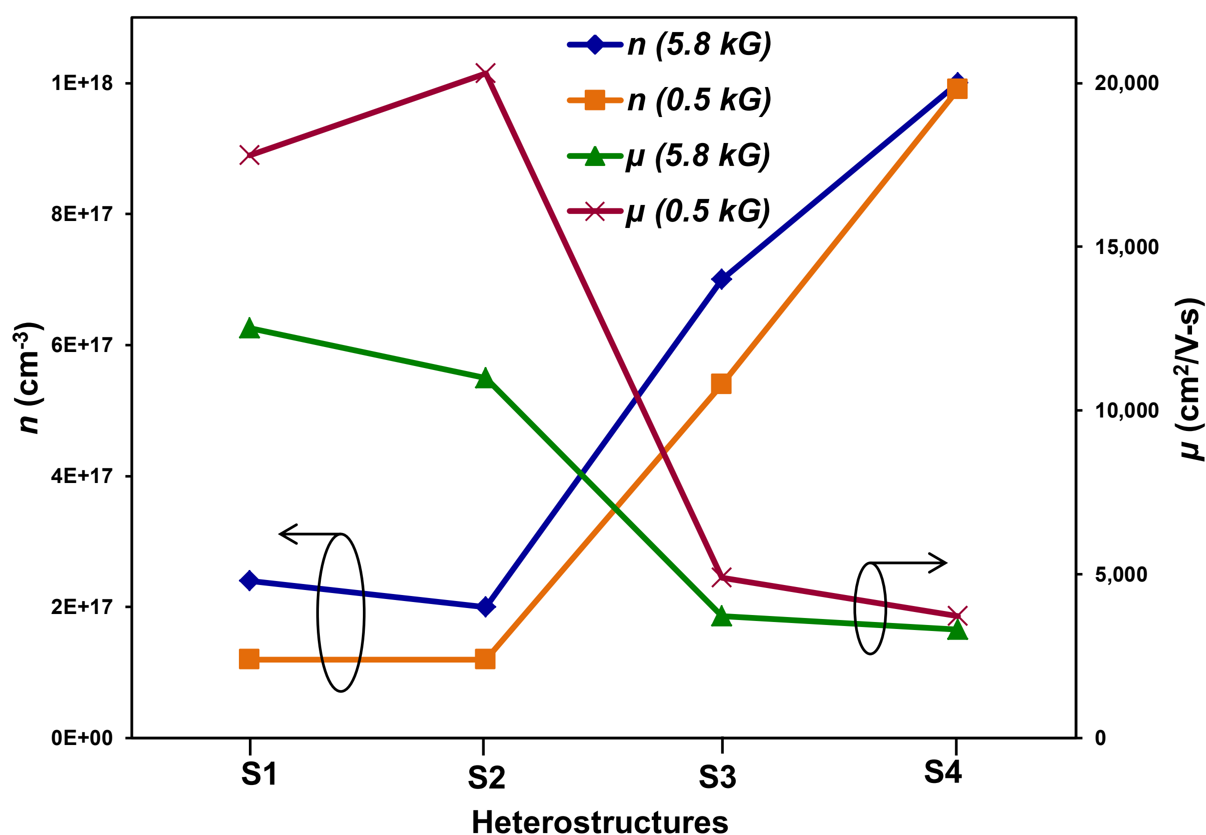

Figure 8.11. The comparison of RT n and μ for different InSbN heterostructures measured at low and high magnetic fields.

8.4 Discussion

A nearly point like highly intense RLP corresponding to GaAs substrate in the (115) RSM contour plot of heterostructure S1 (Figure 8.3) indicated a very high crystalline nature of the chosen substrate. Nearly 14.6 % parallel mismatch observed for the InSb buffer layer w.r.t. GaAs indicate 100 % relaxed and bulk nature of InSb buffer. However, a slight increase in the perpendicular mismatch is believed to be due to N diffusion into the InSb buffer layer. Whereas, the InSbN epilayer was observed to exhibit a low parallel mismatch and high perpendicular mismatch w.r.t. InSb buffer layer indicating a strained epilayer. Two relatively broad RLP profiles for both InSb buffer and InSbN epilayer observed in S1 as compared to the GaAs substrate indicates the broadening to be due to presence of large number of dislocations.[143]

Assuming the 60° nature of the threading dislocations (TD) in (001) zinc blende type semiconductors, these TDs are believed to affect crystal lattice in two unique characteristics. They are, (i) rotational dislocations (RD) sensitive to symmetric HRXRD (004 scans) peak broadening, and (ii) strain field due to TD a primary factor for asymmetric HRXRD (115 scans) peak broadening.[139] Since, presence of these specific dislocations in the epilayers/ heterostructures directly gets reflected on the corresponding HRXRD peak broadening (Equation 3.1); the associated FWHM values will be used for all discussion purpose for both qualitative and quantitative comparison. The intensity of the individual peaks can easily be correlated to the corresponding layer thickness values. Higher the intensity of the HRXRD peaks, thicker the epilayer. The RLP broadening in the (Q_X, Q_Y) plane is representative of the twist in the lattice while the broadening in the Q_Z axis (not evaluated in our case) is commonly correlated to the tilt-related broadening of the mosaic structure.[143] Hence, a relatively high RLP broadening observed in case of S4 indicates poor structural quality as compared to the other heterostructures.

InSbN heterostructures (S1 and S2) with thick InSb buffer layer observed to exhibit relatively lower FWHM for InSb, both in (004) and (115) scans as compared to the heterostructures (S3 and S4) with relatively thin buffer layer. As this is the case with most mismatched/ heteroepitaxial alloys the dislocations due to heteroepitaxy reduce as we go away from the heterojunction interface/defect origin. Due to the thin InSb buffer in S3 and S4 type heterostructures both (004) and (115) profile were observed to be broadened by large number of TDs. Further, the corresponding RLP broadening in S3 and S4 (Figure 8.6 and Figure 8.7) along Q_X and Q_Y, attest to the observed broad HRXRD profile confirming the presence of large number of TDs.[143]

In case of heterostructures, S1 and S2 since the InSb buffer thickness is same, the effect of InSbN epilayer thickness on the quality of the epilayer can be compared. The parallel and perpendicular mismatch values (Table 8.1) indicate a partial relaxation of InSbN epilayer in case of S1 whereas the nitride epilayer in S2 was observed to be completely strained. A small increase in the HRXRD FWHM in case of S1 as compared to S2 indicates the increase in the overall crystal defect due to thicker N-incorporated layer, as the defects due to TDs remain unaltered. This is consistent with our Raman results (Figure 6.3 (a) and (b)) indicating increase in crystal disorder due to N-incorporation at lower growth temperatures. In addition, these N-related defects were observed to affect the overall carrier transport property of the heterostructures. Due to a relatively thick InSb buffer the effect of magneto resistance was clearly observed in case of S2 with a great variation in the μ values measured at 0.5 and 5.8 kG. Hence, for comparison purpose only μ and n measured at 0.5 kG has been considered. Although, a relatively similar n has been observed both for S1 and S2, the S2 type heterostructures are characterized by high RT μ due to less alloy scattering.

RSM performed on the S3 type heterostructure indicate a partially relaxed InSbN epilayer on a 100 % relaxed InSb buffer. Whereas, in case of S4 type heterostructure the asymmetric spread along the surface normal observed in the InSbN RLP has been correlated with a relax-mosaic triangle (RMT) feature.[142] This indicates presence of both relaxation and mosaic spread in the nitride epilayer for S4 type heterostructures. Although presence of nitrogen compositional gradient believed to result in the broadening of reciprocal lattice point (RLP), but the mosaic spread affects the broadening more than the N gradient. Also there is a mosaic twist observed both in the InSb buffer and InSbN peak in the (115) RSM plot (Figure 8.7 (b)). Although a similar mosaic twist and RMT feature observed after *in-situ* annealing, there was no distinct peak for InSb and InSbN RLP both in (004) and (115) RSM scans. Past studies indicate annealing at 430 ºC results in annihilation of N−N interstitials.[93] Further, presence of N−N interstitial and N_{Sb} reported to results in negative mismatch of the nitride HRXRD peak with respect to InSb HRXRD peak.[81, 144] Hence reduction in N−N interstitials and N_{Sb} believed to be the primary reason for the overlap of InSbN RLP and InSb RLP after annealing. This makes it very difficult for estimation of N % from the HRXRD peak simulation. A similar behavior was observed for the *ex-situ* annealed InSbN epilayer (Figure 8.10) annealed at 430 ºC by RTA. The corresponding SIMS depth profile (Figure 7.7) confirmed the presence of N after annealing. Whereas, in case of S2 after *ex-situ* annealing no RMT feature observed for the resultant RLP indicating the nitride layer not relaxed even after annealing. However, the nitride epilayer was observed to be lattice matched with the InSb buffer layer just like other annealed InSbN epilayers.

Figure 8.11 compares the RT n and μ measured at high (5.8 kG) and low (0.5 kG) magnetic field for InSbN heterostructures S1, S2, S3 and S4. The RT n values were not affected

with variation in applied magnetic field. S1 and S2 were observed to exhibit similar n whereas, S3 observed to exhibit very high n. In case of S2 a reduction in RT μ was observed with increase in applied magnetic field can easily be explained due to relatively thick InSb buffer. The effect of magnetic field on the μ values was observed to reduce in S1 as the InSbN epilayer thickness is comparable to the InSb buffer. However, the effect of magneto-resistance was still observed. In case of S3, the RT μ values were observed to be almost the same for both magnetic field values. As the InSbN epilayer thickness is much larger than InSb buffer layer it can be concluded that the observed behavior is the characteristic of InSbN layer. This indicates that InSbN does not exhibit magneto-resistance like InSb. The reduction in the μ values for S3 as compared to S1 and S2 is due to presence of large number of dislocations as discussed earlier in this chapter and Chapter 7.

8.5 Conclusion

The quality of InSb buffer was observed to affect the InSbN epilayer to a great extent. The heteroepitaxial defects were reported to have a greater impact on the overall structural quality of InSbN epilayers as compared to the contribution of defects due to N incorporation. With increase in InSb buffer thickness both the rotational and threading dislocations observed to propagate less into the InSbN epilayer and hence improve the quality of the *as-grown* epilayer. Further, increase in InSbN epilayer thickness on a relatively thin InSb buffer reported to propagate large number of dislocations in the layer in order to attain a 100 % relaxation. Presence of large number of dislocations observed to reduce the RT μ in the InSbN epilayer. Hence one has to grow relatively thick InSb buffer (1.4 µm) and thin InSbN epilayer (0.4~1.2 µm) in order to obtain a good quality InSbN epilayer with less defects and high RT mobility.

CHAPTER 9

Conclusion

Highly crystalline InSb epilayers were grown on GaAs substrate. The method of growth temperature calibration at a specific Sb/In BEP ratio for growth of 2D InSb layers using RHEED has been discussed extensively. A highly smooth surface with R_{rms} of 0.28 nm with was found to be the best for 0.6 μm InSb epilayer grown on GaAs using the above method. Hence, this growth method was used for the growth of InSb buffer layer in InSbN heterostructures for further study. The best RT $n \sim 10^{16}$ cm^{-2} and $\mu \sim 45{,}000$ cm^2/Vs has been reported for 1.4 μm thick InSb epilayer on GaAs. The RT optical absorption for the InSb heterostructure was reported to match its RT fundamental band gap at 0.17 eV.

A systematic study of growth and characterizations was carried out for InSbN heterostructures grown on GaAs substrate under various growth conditions. Increase in N BEP and reduction in growth temperatures at a given Sb/In BEP ratio were found to increase N incorporation in the InSbN epilayers. However, only a small window of N BEP observed to favor the growth of 2D InSbN epilayers. Hence, the variation of N BEP was found to provide a limited window to increase N incorporation as compared to the variation of growth temperature.

With a variation in growth temperatures of InSbN, from 290 ºC to 380 ºC, lower temperature (290-330 ºC) growths observed to contain maximum percentage of substitutional N in the form of In−N bonding. However, the *as-grown* RT Hall measurements indicated a high background carrier concentration in the range of $\sim 10^{18}$ cm^{-3} and lower mobility in ~1,000 cm^2/V-s range due to presence of N interstitials and their related crystal defects. *As-grown* InSbN epitaxial layers grown at 290 ºC exhibited high N incorporation (~2.6 %), mostly in the substitutional sites, with N induced defects and localized states, as evidenced from high

resolution x-ray diffraction, secondary ion mass spectroscopy and RT micro-Raman studies. The RBS study indicated at least 85 % of substitutional N in the *as-grown* InSbN epilayer. A negative band gap of -0.004 eV was estimated corresponding to a high N incorporation of 2.6 %, observed to blue shift due to the high background carrier concentration resulting from the Moss-Burstein effect. Hence, the best *as-grown* RT optical absorption cut-off was observed at ~9.4 µm, corresponding to a band gap of 0.132 eV.

Various annealing techniques were performed to reduce the carrier concentration to device level and thus extend the optical absorption cutoff further into LWIR range for detector applications. InSbN heterostructures were annealed *ex-situ* by RTA and *in-situ* after the growth in the MBE chamber. Along with the annealing temperature the duration of annealing was observed to affect the electrical property of the epilayers. Annealing performed at temperatures ranging from 370 ºC to 450 ºC for various InSbN heterostructures grown at 290 ºC, indicated best results for *ex-situ* and *in-situ* annealing at 430 ºC. The annealing led to the loss of N and improved InSb crystalline quality, attributed to annihilation of N related defects. The increase in I_{LO}/I_{TO} observed in the corresponding micro-Raman spectra along with an appearance of InSb 2LO mode clearly indicate the improvement in the crystalline quality of the heterostructures after annealing. The first derivative of RT absorption spectra indicated a red shifted absorption edge to ~10 µm, reduced the background carrier concentration to ~10^{16} cm^{-3} and enhanced mobility in 10,000 cm^2/V-s range after annealing. A reduction in InSb Urbach tail width in the absorption spectra of *in-situ* annealed InSbN has been correlated to enhanced InSb crystalline quality and reduction in dislocation density due to annealing. The best absorption cutoff ~11.6 µm was observed for InSbN heterostructure annealed at 450 °C with n ~5x10^{16} cm^{-3} and μ ~42,300 cm^2/V-s.

A comparative study of dislocation density reflected from the FWHM of the HRXRD rocking curves, with variation in both InSb buffer and InSbN epilayer thickness for various heterostructures has been carried out and an optimized InSbN heterostructure for the device application has been determined. A systematic reciprocal space map study of various InSbN heterostructures indicated an improvement in the layer epitaxy with increase in the thickness of InSb buffer. Additionally, the heterostructures with thicknesses 0.4 µm InSbN/1.4 µm InSb/GaAs were observed to be strained, whereas the heterostructure 2 µm InSbN/0.2 µm InSb/GaAs was 100 % relaxed. The process of relaxation was reported to propagate tilt and large number dislocations in the layer in order to minimize all the strain energy. Presence of large number of dislocations observed to reduce the RT μ in the InSbN epilayer. Hence one has to grow relatively thick InSb buffer layer in order to obtain a good quality InSbN epilayer for detector applications. The InSbN heterostructure with relatively thick InSb buffer (1.6 µm) and relatively thin InSbN epilayer (0.4~0.6 µm) observed to be strained and exhibit less defects attesting to the high RT mobility.

With all the above results it can clearly be seen that the InSbN heterostructures grown on GaAs substrates can be a promising material system for dual color (MWIR and LWIR) infrared photo detection. A thin InSbN layer epitaxially grown at 290 °C and *ex-situ* annealed at 450 °C on a thick InSb buffer grown at 380 °C on a GaAs substrate reported to be optimized with fewer dislocations and more N incorporation. In this type of dilute nitride heterostructure the InSbN epilayer can be used act as an active detector material for LWIR range where the InSb buffer will detect photons in the MWIR range. Hence, determination of carrier lifetime and doping studies of InSbN are important for the successful implementation of this material system for next generation LWIR detectors. After successful doping of the individual layers, heterostructure as

shown in Figure 9.1 can be grown in order to fabricate a simple mesa structure for device characterization.

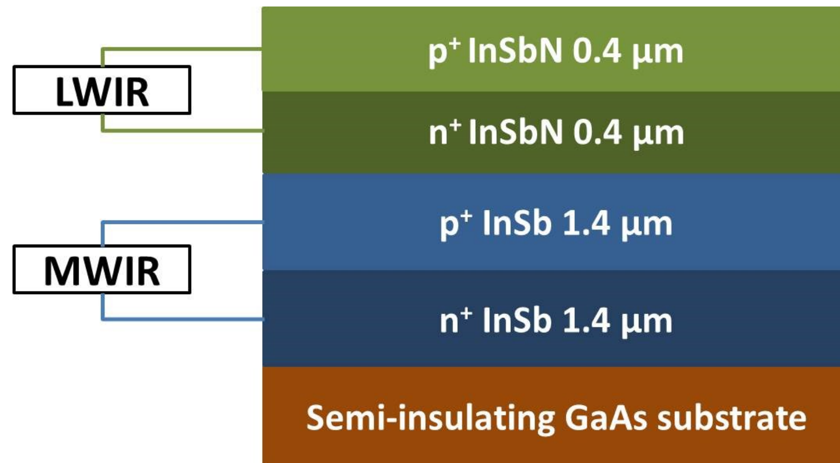

Figure 9.1. InSbN heterostructure for dual color (MWIR and LWIR) applications.

A step-wise device fabrication process along with a method of photo current spectral analysis suggested by our research group in past, has been outlined in the master thesis of Jonathan Poe.[145] Further, study need to be carried to optimize the device structure as reported by Kimukin et al,[33] Rogalski et al,[10] Cohen et al,[146] Barve et al[23] for dual color applications. Hence, the $InSb_{1-x}N_x$ and a combination of InSb and $InSb_{1-x}N_x$ can definitely be the next prospective material system for single band (LWIR) and dual band (MWIR and LWIR) infrared photo detection, respectively.

References

1. http://isc.astro.cornell.edu/~spoon/crashcourse.html

2. Razeghi, M., "Current status and future trend of infrared detectors," *Opto-Electronics Review,* 6, 155-194, 1998.

3. Herschel, W., "Experiments on the refrangibility of the invisible rays of the run," *Philosophical Transactions of the Royal Society of London,* 90, 284-292, 1800.

4. Rogalski, A., "History of infrared detectors," *Opto-Electronics Review,* 20, 279-308, 2012.

5. Rogalski, A., "Infrared detectors: an overview," *Infrared Physics & Technology,* 43, 187-210, 2002.

6. Rogalski, A., *Handbook of Infra-red Technologies*: Elsevier, 2002.

7. Rogalski, A., "Competition of infrared detector technologies," in *Sixth International Conference on Material Science and Material Properties for Infrared Optoelectronics, May 22, 2002 - May 24, 2002*, Kiev, Ukraine, 2003, pp. 23-38.

8. Rogalski, A., "New material systems for third generation infrared photodetectors," *Opto-Electronics Review,* 16, 458-482, 2008.

9. Rogalski, A., "Infrared detectors for the future," *Acta Physica Polonica A,* 116, 389-406, 2009.

10. Rogalski, A., "New material systems for third generation infrared detectors," in *9th International Conference on Correlation Optics, September 20, 2009 - September 24, 2009*, Chernivtsi, Ukraine, 2009, p. Optical Society of America (OSA); European Physical Society (EPS); EuropeanInternational Commission for Optics (ICO); European Optical Society (EOS).

11. Razeghi, M., Kim, J. D., Jelen, C., Slivken, S., Michel, E., Mohseini, H., Lee, J. J., Wojkowski, J., Kim, K. S., Jeon, H. I., & Xu, J., "Infrared imaging arrays using advanced III-V materials and technology," in *Frontiers in Electronics, 1997. WOFE '97. Proceedings., 1997 Advanced Workshop on*, 1997, pp. 57-64.

12. Lopes, V. C., & Et Al., "Minority carrier lifetime in mercury cadmium telluride," *Semiconductor Science and Technology,* 8, 824, 1993.

13. Chen, H. C., Rane, A. B., Zhang, D. X., Murry, S. J., Pei, S. S., Tao, Y. K., Pearah, P. J., & Cheng, K. Y., "Molecular-beam epitaxy growth and characterization of high quality GaAsSb," Urbana, Illinois (USA), 1995, pp. 706-708.

14. Lin, Y.-T., Ma, T.-C., Lin, H.-H., Wu, J.-D., & Huang, Y.-S., "Effect of thermal annealing on the blueshift of energy gap and nitrogen rearrangement in GaAsSbN," *Applied Physics Letters,* 96, 2010.

15. Wang, D., Svensson, S. P., Shterengas, L., Belenky, G., Kim, C. S., Vurgaftman, I., & Meyer, J. R., *Band edge optical transitions in dilute-nitride GaNSb* vol. 105: AIP, 2009.

16. Charache, G. W., Baldasaro, P. F., Danielson, L. R., Depoy, D. M., Freeman, M. J., Wang, C. A., Choi, H. K., Garbuzov, D. Z., Martinelli, R. U., Khalfin, V., Saroop, S., Borrego, J. M., & Gutmann, R. J., "InGaAsSb thermophotovoltaic diode: Physics evaluation," *Journal of Applied Physics,* 85, 2247-2252, 1999.

17. Iyer, S., Hegde, S., Bajaj, K. K., Abul-Fadl, A., & Mitchel, W., "Photoluminescence study of liquid phase electroepitaxially grown GaInAsSb on (100)GaSb," *Journal of Applied Physics,* 73, 3958-3961, 1993.

18. Li, W., Heroux, J. B., & Wang, W. I., "InGaAsSbN: A dilute nitride compound for midinfrared optoelectronic devices," *Journal of Applied Physics,* 94, 4248-4250, 2003.

19. Bethea, C. G., Levine, B. F., Yen, M. Y., & Cho, A. Y., "Photoconductance measurements on $InAs_{0.22}Sb_{0.78}$/GaAs grown using molecular beam epitaxy," *Applied Physics Letters,* 53, 291-292, 1988.

20. Kim, S. M., Yuen, H. B., Hatami, F., Chin, A., & Harris, J. S., "Optical properties of dilute nitride InN(As)Sb quantum wells and quantum dots grown by molecular beam epitaxy," *Journal of Electronic Materials,* 37, 1774-1779, 2008.

21. Ashley, T., Burke, T. M., Pryce, G. J., Adams, A. R., Andreev, A., Murdin, B. N., O'reilly, E. P., & Pidgeon, C. R., "InSb1-xNx growth and devices," *Solid-State Electronics,* 47, 387-394, 2003.

22. Aina, L., Hier, H., Fathimulla, A., Lecates, M., Kolodzey, J., Goossen, K., Coppinger, M., & Bhargava, N., "High detectivity dilute nitride strained layer superlattice detectors for LWIR and VLWIR applications," *Infrared Physics & Technology,* 52, 310-316, 2009.

23. Barve, A. V., Lee, S. J., Noh, S. K., & Krishna, S., "Review of current progress in quantum dot infrared photodetectors," *Laser & Photonics Reviews,* 4, 738-750, 2010.

24. Sarath, D. G., Sumith, V. B., Cory, J. H., David, Z. T., John, K. L., Sir, B. R., Edward, R. B., Jason, M. M., Sam, A. K., Sanjay, K., Chang, Y. C., & Craig, A. S., "640x512 pixels long-wavelength infrared (LWIR) quantum-dot infrared photodetector (QDIP) imaging focal plane array," *Quantum Electronics, IEEE Journal of,* 43, 230-237, 2007.

25. Gunapala, S. D., Ting, D. Z., Hill, C. J., Soibel, A., Liu, J., Liu, J. K., Mumolo, J. M., Keo, S. A., Nguyen, J., Bandara, S. V., & Tidrow, M. Z., "III-V infrared research at the Jet Propulsion Laboratory," 2009, p. 74670R.

26. Kim, J. D., Wu, D., Wojkowski, J., Piotrowski, J., Xu, J., & Razeghi, M., "Long-wavelength InAsSb photoconductors operated at near room temperatures (200-300 K)," *Applied Physics Letters,* 68, 99-101, 1996.

27. Kim, J. D., Michel, E., Park, S., Xu, J., Javadpour, S., & Razeghi, M., "Room-temperature operation of InTlSb infrared photodetectors on GaAs," *Applied Physics Letters,* 69, 343-344, 1996.

28. Lim, K. P., Pham, H. T., Yoon, S. F., Tan, K. H., & Ngo, C. Y., "$InSb_{1-x}N_x$/InSb/GaAs alloys by thermal annealing for midinfrared photodetection," *Applied Physics Letters,* 97, 221112-221113, 2010.

29. Rhiger, D., "Performance comparison of long-wavelength infrared type II superlattice devices with HgCdTe," *Journal of Electronic Materials,* 40, 1815-1822, 2011.

30. Patra, N. C., Bharatan, S., Li, J., Tilton, M., & Iyer, S., "Molecular beam epitaxial growth and characterization of $InSb_{1-x}N_x$ on GaAs for long wavelength infrared applications," *Journal of Applied Physics,* 111, 083104-083108, 2012.

31. Kane, E. O., "Band structure of Indium Antimonide," *Journal of Physics and Chemistry of Solids,* 1, 249-261, 1957.

32. Kimukin, I., Biyikli, N., & Ozbay, E., "InSb high-speed photodetectors grown on GaAs substrate," *Journal of Applied Physics,* 94, 5414-5416, 2003.

33. Kimukin, I., Biyikli, N., Kartaloglu, T., Aytur, O., & Ozbay, E., "High-speed InSb photodetectors on GaAs for mid-IR applications," *Selected Topics in Quantum Electronics, IEEE Journal of,* 10, 766-770, 2004.

34. Kuze, N., Camargo, E. G., Ueno, K., Morishita, T., Sato, M., Kurihara, M., Endo, H., & Ishibashi, K., "High performance miniaturized InSb photovoltaic infrared sensors operating at room temperature," *Journal of Crystal Growth,* 301-302, 997-1000, 2007.

35. Camargo, E. G., Ueno, K., Kawakami, Y., Moriyasu, Y., Nagase, K., Satou, M., Endo, H., Ishibashi, K., & Kuze, N., "Miniaturized InSb photovoltaic infrared sensor operating at room temperature," *Optical Engineering,* 47, 014402, 2008.

36. Shibasaki, I., & Kuze, N., "Chapter 31 - Mass production of sensors grown by MBE," in *Molecular Beam Epitaxy*, ed Oxford: Elsevier, 2013, pp. 697-720.

37. Ashley, T., Baker, I. M., Burke, T. M., Dutton, D. T., Haigh, J. A., Hipwood, L. G., Jefferies, R., Johnson, A. D., Knowles, P., & Little, J. C., "InSb focal plane array (FPAs) grown by molecular beam epitaxy (MBE)," 2000, pp. 398-403.

38. Hoffman, A., & Woolaway, J., "The future of large-format InSb arrays for astronomy," *Experimental Astronomy,* 3, 211-217, 1994.

39. Yano, M., Takase, T., & Kimata, M., "Heteroepitaxial InSb films grown by molecular beam epitaxy," *physica status solidi (a),* 54, 707-713, 1979.

40. Zhang, Y. H., Chen, P. P., Lin, T., Xia, H., & Li, T. X., "MBE growth and electrical properties of InSb film on GaAs substrate," 2010, p. 79952G.

41. Dixit, V. K., Rodrigues, B. V., Bhat, H. L., Venkataraghavan, R., Chandrasekaran, K. S., & Arora, B. M., "Growth of InSb epitaxial layers on GaAs (001) substrates by LPE and their characterizations," *Journal of Crystal Growth,* 235, 154-160, 2002.

42. Dixit, V. K., Bansal, B., Venkataraman, V., Bhat, H. L., Subbanna, G. N., Chandrasekharan, K. S., & Arora, B. M., "High-mobility InSb epitaxial films grown on a

GaAs (001) substrate using liquid-phase epitaxy," *Applied Physics Letters,* 80, 2102-2104, 2002.

43. Graham, R. M., Mason, N. J., Walker, P. J., Frigo, D. M., & Gedridge Jr, R. W., "MOVPE growth of InSb on GaAs substrates," *Journal of Crystal Growth,* 124, 363-370, 1992.

44. Thompson, P. E., Davis, J. L., Waterman, J., Wagner, R. J., Gammon, D., Gaskill, D. K., & Stahlbush, R., "Use of atomic layer epitaxy buffer for the growth of InSb on GaAs by molecular beam epitaxy," *Journal of Applied Physics,* 69, 7166-7172, 1991.

45. Kim, T. W., Bae, H. C., & Park, H. L., "Structural and optical properties of InSb epitaxial films grown on GaAs (100) substrates at low temperature," *Applied Physics Letters,* 74, 380-382, 1999.

46. Song, S. N., Ketterson, J. B., Choi, Y. H., Sudharsanan, R., & Razeghi, M., "Transport properties in n-type InSb films grown by metalorganic chemical vapor deposition," *Applied Physics Letters,* 63, 964-966, 1993.

47. Weng, X., Goldman, R. S., Partin, D. L., & Heremans, J. P., "Evolution of structural and electronic properties of highly mismatched InSb films," *Journal of Applied Physics,* 88, 6276-6286, 2000.

48. Rao, T. S., Halpin, C., Webb, J. B., Noad, J. P., & Rajan, K., "Characterization of heteroepitaxial InSb films on GaAs prepared by metalorganic magnetron sputtering," *Thin Solid Films,* 163, 399-404, 1988.

49. Feng, Z. C., Perkowitz, S., Rao, T. S., & Webb, J. B., "Resonance Raman scattering from epitaxial InSb films grown by metalorganic magnetron sputtering," *Journal of Applied Physics,* 68, 5363-5365, 1990.

50. Rousina, R., & Webb, J. B., "Magnetron sputter epitaxy (MSE) of InSb on (100) GaAs and (100, 111) InSb for infrared detector applications," *Semiconductor Science and Technology,* 6, C42, 1991.

51. Soderstrom, J. R., & Et Al., "Molecular beam epitaxy growth and characterization of InSb layers on GaAs substrates," *Semiconductor Science and Technology,* 7, 337, 1992.

52. Kanisawa, K., Yamaguchi, H., & Hirayama, Y., "Two-dimensional growth of InSb thin films on GaAs (111)A substrates," *Applied Physics Letters,* 76, 589-591, 2000.

53. Noreika, A. J., Francombe, M. H., & Wood, C. E. C., "Growth of Sb and InSb by molecular-beam epitaxy," *Journal of Applied Physics,* 52, 7416-7420, 1981.

54. Noreika, A. J., J. Greggi, J., Takei, W. J., & Francombe, M. H., "Properties of MBE grown InSb and $InSb_{1-x}Bi_x$," *Journal of Vacuum Science & Technology A: Vacuum, Surfaces, and Films,* 1, 558-561, 1983.

55. Davis, J. L., & Thompson, P. E., "Molecular beam epitaxy growth of InSb films on GaAs," *Applied Physics Letters,* 54, 2235-2237, 1989.

56. Mcconville, C. F., Whitehouse, C. R., Williams, G. M., Cullis, A. G., Ashley, T., Skolnick, M. S., Brown, G. T., & Courtney, S. J., "Interfacial studies and electrical characterisation of heteroepitaxial InSb on GaAs (100) grown by MBE," *Journal of Crystal Growth,* 95, 228-234, 1989.

57. Williams, G. M., Whitehouse, C. R., Mcconville, C. F., Cullis, A. G., Ashley, T., Courtney, S. J., & Elliott, C. T., "Heteroepitaxial growth of InSb on (100) GaAs using molecular beam epitaxy," *Applied Physics Letters,* 53, 1189-1191, 1988.

58. Zhang, X., Staton-Bevan, A. E., Pashley, D. W., Parker, S. D., Droopad, R., Williams, R. L., & Newman, R. C., "A transmission electron microscopy and reflection high-energy

electron diffraction study of the initial stages of the heteroepitaxial growth of InSb on GaAs (001) by molecular beam epitaxy," *Journal of Applied Physics,* 67, 800-806, 1990.

59. Li, L. K., Hsu, Y., & Wang, W. I., "Molecular-beam epitaxial growth of InSb on GaAs and Si for infrared detector applications," 1993, pp. 872-874.

60. Michel, E., Singh, G., Slivken, S., Besikci, C., Bove, P., Ferguson, I., & Razeghi, M., "Molecular beam epitaxial growth of high quality InSb," *Applied Physics Letters,* 65, 3338-3340, 1994.

61. Shan, W., Walukiewicz, W., Ager, J. W., Haller, E. E., Geisz, J. F., Friedman, D. J., Olson, J. M., & Kurtz, S. R., "Band anticrossing in GaInNAs alloys," *Physical Review Letters,* 82, 1221, 1999.

62. Shan, W., & Et Al., "Band anticrossing in dilute nitrides," *Journal of Physics: Condensed Matter,* 16, S3355, 2004.

63. Walukiewicz, W., "Narrow band gap group III-nitride alloys," *Physica E: Low-dimensional Systems and Nanostructures,* 20, 300-307, 2004.

64. Shan, W., Walukiewicz, W., Yu, K. M., Ager Iii, J. W., Haller, E. E., Geisz, J. F., Friedman, D. J., Olson, J. M., Kurtz, S. R., Xin, H. P., & Tu, C. W., "Band anticrossing in III–N–V Alloys," *physica status solidi (b),* 223, 75-85, 2001.

65. Wu, J., & Et Al., "Band anticrossing in highly mismatched III–V semiconductor alloys," *Semiconductor Science and Technology,* 17, 860, 2002.

66. Nunna, K., "Effects of N incorporation on the properties of GaAsSbN single quantum wells and light emitting devices in the 1.55 micron wavelength region," Electrical and Computer Engineering, North Carolina A&T State University, 2007.

67. Wu, L., PhD, Electrical and Computer Engineering, North Carolina A&T State University, 2005.

68. Bharatan, S., "MBE growth of lattice-matched GaAsSbN/GaAs and InGaAsSbN/GaSb quantum wells for optoelectronic devices," Electrical and Computer Engineering, North Carolina A&T State University, 2009.

69. Yuen, H. B., "Growth and characterization of dilute nitride antimonides for long-wavelength optoelectronics," Material Science and Engineering, Stanford University, 2006.

70. Murdin, B. N., Adams, A. R., Murzyn, P., Pidgeon, C. R., Bradley, I. V., Wells, J. P. R., Matsuda, Y. H., Miura, N., Burke, T., & Johnson, A. D., "Band anticrossing in dilute InN_xSb_{1-x}," *Applied Physics Letters,* 81, 256-258, 2002.

71. O'reilly, E. P., & Lindsay, A., "k · P model of ordered $GaN_xAs_{1—x}$," *physica status solidi (b),* 216, 131-134, 1999.

72. Lindsay, A., Andreev, A. D., O’reilly, E. P., & Ashley, T., "Band structure of InSbN and GaSbN," ed, 2008, pp. 45-47.

73. Lindsay, A., O'reilly, E. P., Andreev, A. D., & Ashley, T., "Theory of conduction band structure of In N_x Sb_{1-x} and Ga N_x Sb_{1-x} dilute nitride alloys," *Physical Review B,* 77, 165205, 2008.

74. Bhusal, L., & Freundlich, A., "Assessment of electronic properties of InNxSb1-x for long-wavelength infrared detector applications," *Applied Surface Science,* 255, 703-705, 2008.

75. Tomić, S., O’reilly, E. P., Klar, P. J., Grüning, H., Heimbrodt, W., Chen, W. M., & Buyanova, I. A., "Influence of conduction-band nonparabolicity on electron confinement

and effective mass in GaN_xAs_{1-x}/GaAs quantum wells," *Physical Review B,* 69, 245305, 2004.

76. Johnson, A. D., Bennett, R. H., Newey, J., Pryce, G. J., Williams, G. M., Burke, T. M., Jones, J. C., & Keir, A. M., "InNxSb1-x light emitting diodes grown by MBE," in *The 1999 MRS Fall Meeting - Symposium OO 'Infrared Applications of Semiconductors III', November 29, 1999 - December 2, 1999*, Boston, MA, USA, 2000, pp. 23-27.

77. Ishiguro, T., Kobori, Y., Nagawa, Y., Iwamura, Y., & Yamaguchi, S., "Crystal growth and electrical characterization of InSbN grown by metalorganic vapor phase epitaxy," in *Progress in Compound Semiconductor Materials III - Electronic and Opoelectronic Applications, December 1, 2003 - December 4, 2003*, Boston, MA, United states, 2003, pp. 45-49.

78. Jin, Y. J., Tang, X. H., Chen, X. Z., & Zhang, D. H., "Properties of InSb (N) epilayers grown by metal-organic chemical vapor deposition," in *Photonics Global Conference (PGC), 2010*, Orchard, Singapore, 2010, pp. 1-4.

79. Wang, Y., Zhang, D. H., Huang, Z. M., Liu, W., Li, J. H., Liu, C. J., & Wee, A. T. S., "Study of ion-implanted in $Sb_{1-x}N_x$ alloys using secondary ion mass spectroscopy," in *IEEE Conference on Electron Devices and Solid-State Circuits 2007, December 20 - 22, 2007*, Tainan, Taiwan, 2007, pp. 677-680.

80. Zhang, D. H., Liu, W., Wang, Y., Chen, X. Z., Li, J. H., Huang, Z. M., & Zhang, S. S. Y., "InSbN alloys prepared by two-step ion implantation for infrared photodetection," *Applied Physics Letters,* 93, 131107-131103, 2008.

81. Pham, H. T., Yoon, S. F., Tan, K. H., & Boning, D., "Effects of nitrogen incorporation in $InSb_{1-x}N_x$ grown using radio frequency plasma-assisted molecular beam epitaxy," *Applied Physics Letters,* 90, 092115-092113, 2007.

82. Lim, K. P., Yoon, S. F., & Pham, H. T., "Properties of InSbN grown on GaAs by radio frequency nitrogen plasma-assisted molecular beam epitaxy," *Journal of Physics D: Applied Physics,* 42, 135419, 2009.

83. Zhang, Y. H., Chen, P. P., Yin, H., Li, T. X., & Lu, W., "The effects of growth parameters on the RF-MBE growth of dilute InNSb films," *Journal of Physics D: Applied Physics,* 43, 305405 (305406 pp.), 2010.

84. Mahboob, I., Veal, T. D., & Mcconville, C. F., "Determination of the substitutional nitrogen content and the electron effective mass in InN_xSb_{1-x} (001) epitaxial layers," *Optoelectronics, IEE Proceedings -,* 150, 102-104, 2003.

85. Li, W., Pessa, M., & Likonen, J., "Lattice parameter in GaNAs epilayers on GaAs: deviation from Vegard's law," *Applied Physics Letters,* 78, 2864-2866, 2001.

86. Fan, W. J., Yoon, S. F., Ng, T. K., Wang, S. Z., Loke, W. K., Liu, R., & Wee, A., "Comparison of nitrogen compositions in the as-grown GaN_xAs_{1-x} on GaAs measured by high-resolution x-ray diffraction and secondary-ion mass spectroscopy," *Applied Physics Letters,* 80, 4136-4138, 2002.

87. Jefferson, P. H., Buckle, L., Walker, D., Veal, T. D., Coomber, S., Thomas, P. A., Ashley, T., & Mcconville, C. F., "Growth and characterisation of high quality MBE grown InN_xSb_{1-x}," *physica status solidi (RRL) – Rapid Research Letters,* 1, 104-106, 2007.

88. Lim, K. P., Yoon, S. F., Pham, H. T., & Tripathy, S., "Defect characterization of InSbN grown using radio frequency nitrogen plasma-assisted molecular beam epitaxy," *Journal of Physics D: Applied Physics,* 41, 165301, 2008.

89. Lim, K. P., Pham, H. T., Yoon, S. F., Markwitz, A., & Yakovlev, N., "Growth temperature and plasma power effects on N incorporation in InSbN grown by molecular beam epitaxy," *physica status solidi - Rapid Research Letters,* 3, 263-265, 2009.

90. Brewer, P. D., Chow, D. H., & Miles, R. H., "Atomic antimony for molecular beam epitaxy of high quality III--V semiconductor alloys," *Journal of Vacuum Science & Technology B,* 14, 2335-2338, 1996.

91. Veal, T. D., Mahboob, I., Mcconville, C. F., Burke, T. M., & Ashley, T., "Effect of hydrogen in dilute InN_xSb_{1-x} alloys grown by molecular beam epitaxy," *Applied Physics Letters,* 83, 1776-1778, 2003.

92. Buckle, L., Coomber, S. D., Ashley, T., Jefferson, P. H., Walker, D., Veal, T. D., Mcconville, C. F., & Thomas, P. A., "Growth and characterisation of dilute antimonide nitride materials for long-wavelength applications," *Microelectronics Journal,* 40, 399-402, 2009.

93. Lim, K. P., Pham, H. T., Yoon, S. F., Ngo, C. Y., & Tripathy, S., "Effect of thermal annealing on properties of InSbN grown by molecular beam epitaxy," *Applied Physics Letters,* 96, 2010.

94. Chen, X. Z., Zhang, D. H., Wang, Y., Jin, Y. J., Li, J. H., Deng, F. X., & Zhang, S., "Study of annealing condition of InSbN alloys fabricated by ion implantation," in *17th International Symposium on the Physical and Failure Analysis of Integrated Circuits, IPFA 2010, July 5, 2010 - July 9, 2010*, Singapore, Singapore, 2010.

95. Wang, Y., Zhang, D. H., Chen, X. Z., Jin, Y. J., Li, J. H., Liu, C. J., Wee, A. T. S., Zhang, S., & Ramam, A., "Bonding and diffusion of nitrogen in the InSbN alloys fabricated by two-step ion implantation," *Applied Physics Letters,* 101, 021905-021904, 2012.

96. Hosea, T. J. C., Merrick, M., & Murdin, B. N., "A new Fourier transform photo-modulation spectroscopic technique for narrow band-gap materials in the mid- to far-infra-red," in *International Workshop on Modulation Spectroscopy of Semiconductor Structures (MS3), 1-3 July 2004*, Germany, 2005, pp. 1233-1243.

97. Merrick, M., Hosea, T. J. C., Murdin, B. N., Ashley, T., Buckle, L., & Burke, T., "Bandgap bowing in $InSb_{1-x}N_x$ investigated with a new fourier transform modulated spectroscopy technique for the mid-infrared," in *Physics of Semiconductors. 27th International Conference on the Physics of Semiconductors. ICPS-27, 26-30 July 2004*, USA, 2005, pp. 295-296.

98. Shih, D.-K., Lin, H.-H., Sung, L.-W., Chu, T.-Y., & Yang, T.-R., "Band gap reduction in InAsN alloys," *Japanese Journal of Applied Physics,* 42, 375-383, 2002.

99. Moss, T. S., "The interpretation of the properties of Indium Antimonide," *Proceedings of the Physical Society. Section B,* 67, 775, 1954.

100. Burstein, E., "Anomalous optical absorption limit in InSb," *Physical Review,* 93, 632-633, 1954.

101. Chen, X. Z., Zhang, D. H., Jin, Y. J., & Zhang, S., "Electrical optical properties of Mg-doped narrow band-gap InSbN p-n junction," in *2010 Photonics Global Conference, PGC 2010, December 14, 2010 - December 16, 2010*, Orchard, Singapore, 2010.

102. Lim, K. P., Pham, H. T., Yoon, S. F., & Tan, K. H., "Effect of N incorporation on the characteristics of InSbN P–N diodes," *Thin Solid Films,* 520, 2269–2271, 2012.

103. Das Sarma, S., "Numerical studies of epitaxial kinetics: What can computer simulation tell us about nonequilibrium crystal growth?," *Journal of Vacuum Science & Technology A: Vacuum, Surfaces, and Films,* 8, 2714-2726, 1990.

104. Arthur, J. R., "Molecular beam epitaxy," *Surface Science,* 500, 189-217, 2002.

105. Maksym, P. A., & Beeby, J. L., "A theory of RHEED," *Surface Science,* 110, 423-438, 1981.

106. Braun, W. (1999). *Applied RHEED:reflection high-energy electron diffraction during crystal growth. 154.*

107. Egelhoff, W. F., Jr., & Jacob, I., "Reflection high-energy electron diffraction (RHEED) oscillations at 77 K," *Physical Review Letters,* 62, 921-924, 1989.

108. Neave, J. H., Joyce, B. A., & Dobson, P. J., "Dynamic RHEED observations of the MBE growth of GaAs," *Applied Physics A,* 34, 179-184, 1984.

109. Armstrong, S. R., Hoare, R. D., Pemble, M. E., Povey, I. M., Stafford, A., Taylor, A. G., Joyce, B. A., Neave, J. H., Klug, D. R., & Zhang, J., "A RHEED and reflectance anisotropy study of the mbe growth of GaAs, AlAs and InAs on GaAs (001)," *Surface Science,* 274, 263-269, 1992.

110. Debnath, M. C., Mishima, T. D., Santos, M. B., Hossain, K., & Holland, O. W., "Growth of InSb epilayers and quantum wells on Ge (001) substrates by molecular beam epitaxy," *Journal of Vacuum Science & Technology B: Microelectronics and Nanometer Structures,* 27, 2453-2456, 2009.

111. Shiba, Y., Asai, K., Kamei, K., & Katahama, H., "Threading dislocation reduction in GaAs on Si with a single InGaAs intermediate layer," *Japanese Journal of Applied Physics,* 34, 1466-1471, 1995.

112. Moram, M. A., & Vickers, M. E., "X-ray diffraction of III-nitrides," *Reports on Progress in Physics,* 72, 036502, 2009.

113. Moazzami, K., Phillips, J., Lee, D., Edwall, D., Carmody, M., Piquette, E., Zandian, M., & Arias, J., "Optical-absorption model for molecular-beam epitaxy HgCdTe and application to infrared detector photoresponse," *Journal of Electronic Materials,* 33, 701-708, 2004.

114. Pino, R., Ko, Y., Dutta, P. S., Guha, S., & Gonzalez, L. P., "Burstein-Moss shift in impurity-compensated bulk $Ga_{1-x}In_xSb$ substrates," *Journal of Applied Physics,* 96, 5349-5352, 2004.

115. Jain, S. C., Mcgregor, J. M., & Roulston, D. J., *Band-gap narrowing in novel III-V semiconductors* vol. 68: AIP, 1990.

116. Haworth, L., Lu, J., Hill, P., Westwood, D. I., Macdonald, J. E., Hartmann, N., Schneider, A., & Zahn, D. R. T., "Formation of an Sb-N compound during nitridation of InSb (001) substrates using atomic nitrogen," *Journal of Vacuum Science and Technology B: Microelectronics and Nanometer Structures,* 16, 2254-2260, 1998.

117. Oe, K., "RHEED study of InSb Films grown by molecular beam epitaxy," *Japanese Journal of Applied Physics,* 19, L417-L420, 1980.

118. Rawdanowicz, T. A., Iyer, S., Mitchel, W. C., Saxler, A., & Elhamri, S., "Electronic properties of heteroepitaxial undoped and n-InSb epilayers using SnTe source by molecular beam epitaxy," *Journal of Applied Physics,* 92, 296-301, 2002.

119. Debnath, M. C., Zhang, T., Roberts, C., Cohen, L. F., & Stradling, R. A., "High-mobility InSb thin films on GaAs (001) substrate grown by the two-step growth process," *Journal of Crystal Growth,* 267, 17-21, 2004.

120. Zhang, T., Clowes, S. K., Debnath, M., Bennett, A., Roberts, C., Harris, J. J., Stradling, R. A., Cohen, L. F., Lyford, T., & Fewster, P. F., "High-mobility thin InSb films grown by molecular beam epitaxy," *Applied Physics Letters,* 84, 4463-4465, 2004.

121. Iyer, S., Wu, L., Li, J., Potoczny, S., Matney, K., & Kent, P. R. C., "Effects of N incorporation on the structural and photoluminescence characteristics of GaSbN/GaSb single quantum wells," *Journal of Applied Physics,* 101, 2007.

122. Buckle, L., Bennett, B. R., Jollands, S., Veal, T. D., Wilson, N. R., Murdin, B. N., Mcconville, C. F., & Ashley, T., "Growth of dilute GaNSb by plasma-assisted MBE," *Journal of Crystal Growth,* 278, 188-192, 2005.

123. Wu, S. D., Guo, L. W., Li, Z. H., Shang, X. Z., Wang, W. X., Huang, Q., & Zhou, J. M., "Effect of the low-temperature buffer thickness on quality of InSb grown on GaAs substrate by molecular beam epitaxy," *Journal of Crystal Growth,* 277, 21-25, 2005.

124. Hecht, J. D., Frost, F., Hirsch, D., Neumann, H., Schindler, A., Preobrajenski, A. B., & Chasse, T., "Interstitial nitrogen induced by low-energy ion beam nitridation of AIII-BV semiconductor surfaces," *Journal of Applied Physics,* 90, 6066-6069, 2001.

125. Hecht, J. D., Frost, F., Chassé, T., Hirsch, D., Neumann, H., Schindler, A., & Bigl, F., "In situ characterization of the nitridation of AIII-BV semiconductor surfaces by means of x-ray photoelectron spectroscopy," *Applied Surface Science,* 179, 196-202, 2001.

126. Veal, T. D., Mahboob, I., & Mcconville, C. F., "Negative band gaps in dilute InN_xSb_{1-x} alloys," *Physical Review Letters,* 92, 136801, 2004.

127. Groenen, J., Mlayah, A., Carles, R., Ponchet, A., Corre, A. L., & Salaün, S., *Strain in InAs islands grown on InP (001) analyzed by Raman spectroscopy* vol. 69: AIP, 1996.

128. Liu, H. F., Xiang, N., Tripathy, S., & Chua, S. J., "Raman scattering probe of anharmonic effects due to temperature and compositional disorder in GaN_xAs_{1-x}," *Journal of Applied Physics,* 99, 103503, 2006.

129. Ejeckam, F. E., Seaford, M. L., Lo, Y.-H., Hou, H. Q., & Hammons, B. E., "Dislocation-free InSb grown on GaAs compliant universal substrates," *Applied Physics Letters,* 71, 776-778, 1997.

130. Chandola, A., & Et Al., "Below bandgap optical absorption in tellurium-doped GaSb," *Semiconductor Science and Technology,* 20, 886, 2005.

131. Bharatan, S., Iyer, S., Nunna, K., Collis, W. J., Matney, K., Reppert, J., Rao, A. M., & Kent, P. R. C., "The effects of annealing on the structural, optical, and vibrational properties of lattice-matched GaAsSbN/GaAs grown by molecular beam epitaxy," *Journal of Applied Physics,* 102, 023503, 2007.

132. Li, J., Iyer, S., Bharatan, S., Wu, L., Nunna, K., Collis, W., Bajaj, K. K., & Matney, K., "Annealing effects on the temperature dependence of photoluminescence characteristics of GaAsSbN single-quantum wells," *Journal of Applied Physics,* 98, 013703-013706, 2005.

133. Gambin, V., Lordi, V., Ha, W., Wistey, M., Takizawa, T., Uno, K., Friedrich, S., & Harris, J., "Structural changes on annealing of MBE grown (Ga, In)(N, As) as measured by x-ray absorption fine structure," *Journal of Crystal Growth,* 251, 408-411, 2003.

134. Patra, N. C., Bharatan, S., Li, J., & Iyer, S., "Annealing studies of heteroepitaxial InSbN on GaAs grown by molecular beam epitaxy for long-wavelength infrared detectors," *Journal of Applied Physics,* 112, 083107-083105, 2012.

135. Chand, N., Allam, J., Gibson, J. M., Capasso, F., Beltram, F., Macrander, A. T., Hutchinson, A. L., Hopkins, L. C., Bethea, C. G., Levine, B. F., & Cho, Y., "GaAs avalanche photodiodes and the effect of rapid thermal annealing on crystalline quality of GaAs grown on Si by molecular-beam epitaxy," *Journal of Vacuum Science & Technology B: Microelectronics and Nanometer Structures,* 5, 822-826, 1987.

136. Ayers, J. E., Ghandhi, S. K., & Schowalter, L. J., "Threading dislocation densities in mismatched heteroepitaxial (001) semiconductors," in *Defects in Materials, Fall Meeting, 1990*, Boston, MA, United states, 1990, pp. 661-666.

137. Ayers, J. E., Schowalter, L. J., & Ghandhi, S. K., "Post-growth thermal annealing of GaAs on Si(001) grown by organometallic vapor phase epitaxy," *Journal of Crystal Growth,* 125, 329-335, 1992.

138. Zhang, X. G., Rodriguez, A., Li, P., Jain, F. C., & Ayers, J. E., "A novel approach for the complete removal of threading dislocations from mismatched heteroepitaxial layers," in *Infuences of Interface and Dislocation Behavior on Microstructure Evolution, November 27, 2000 - November 30, 2000*, Boston, MA, United states, 2001, pp. Y881-Y886.

139. Ayers, J. E., "The measurement of threading dislocation densities in semiconductor crystals by X-ray diffraction," *Journal of Crystal Growth,* 135, 71-77, 1994.

140. Dexter, D. L., & Seitz, F., "Effects of dislocations on mobilities in semiconductors," *Physical Review,* 86, 964-965, 1952.

141. Chen, X. Z., Zhang, D. H., Jin, Y. J., Li, J. H., Teng, J. H., & Yakovlev, N., "Effect of rapid thermal annealing on behavior of nitrogen in GaAsN alloys," *Journal of Crystal Growth,* 362, 197-201, 2013.

142. Heinke, H., Möller, M. O., Hommel, D., & Landwehr, G., "Relaxation and mosaicity profiles in epitaxial layers studied by high resolution X-ray diffraction," *Journal of Crystal Growth,* 135, 41-52, 1994.

143. Chierchia, R., Bottcher, T., Heinke, H., Einfeldt, S., Figge, S., & Hommel, D., "Microstructure of heteroepitaxial GaN revealed by x-ray diffraction," *Journal of Applied Physics,* 93, 8918-8925, 2003.

144. Geddo, M., Patrini, M., Guizzetti, G., Galli, M., Trotta, R., Polimeni, A., Capizzi, M., Martelli, F., & Rubini, S., *Optical study of hydrogen-irradiated GaAsN/GaAs heterostructures* vol. 109: AIP, 2011.

145. Poe, J., "Development of theoretical modeling and an optical characterization system for photodetectors in the 8-12 μm wavelength region," MS, Electrical and Computer Engineering, North Carolina A&T State University, 2011.

146. Cohen, N., Mizrahi, G., Sarusi, G., & Sa'ar, A., "Integrated HBT/QWIP structure for dual color imaging," *Infrared Physics & Technology,* 47, 43-52, 2005.

Appendix A

Publications and Conference Presentations During the Research Work

1. List of Publications:

1. Nimai C. Patra, Sudhakar Bharatan, Jia Li, Michael Tilton and Shanthi Iyer, "Molecular beam epitaxial growth and characterization of $InSb_{1-x}N_x$ on GaAs for long wavelength infrared applications," *Journal of Applied Physics,* vol. 111, pp. 083104-083108, 2012.

2. Nimai C. Patra, Sudhakar Bharatan, Jia Li and Shanthi Iyer, "Annealing studies of heteroepitaxial InSbN on GaAs grown by molecular beam epitaxy for long-wavelength infrared detectors," *Journal of Applied Physics,* vol. 112, pp. 083107-083105, 2012.

2. List of Conferences:

1. Nimai C. Patra, Sudhakar Bharatan, Jia Li, and Shanthi Iyer, "Growth, characterization and annealing studies of InSbN heterostructures grown by MBE for long-wavelength infrared detection", 29th North American Molecular Beam Epitaxy (NAMBE) conference, Stone Mountain, GA, October 14-17, 2012.

2. Nimai C. Patra, Shanthi Iyer, "A Study of MBE Grown $InSb_{1-x}N_x$ Epilayers for LWIR Applications", presented at 1st Annual COE Graduate Research Poster Competition at North Carolina A&T State University, Greensboro, NC, April 26, 2012.

3. Nimai C. Patra, Sudhakar Bharatan, Jia Li and Shanthi Iyer, "Nitrogen incorporation studies in InSbN MBE grown epilayers", Materials Research Society North Carolina Symposium, Raleigh, NC, November 18, 2011.

4. Nimai C. Patra, Sudhakar Bharatan, Jia Li, Michael L. Tilton and Shanthi Iyer, "Growth and Characterization of $InSb_{1-x}N_x$ on GaAs for LWIR Applications", 28th North American Molecular Beam Epitaxy (NAMBE) conference, San Diego, CA, August 14-17, 2011.

5. Nimai C. Patra, Sudhakar Bharatan, Jia Li and Shanthi Iyer, "A study of MBE grown $InSb_{1-x}N_x$ on GaAs for Long-Wavelength IR Applications", 53rd Electronic Materials Conference (EMC) and Exhibition, Santa Barbara, CA, June 22-24, 2011.

6. Sudhakar Bharatan, Nimai C. Patra, Jia Li and Shanthi Iyer, "A Study of MBE Grown $InSb_{1-x}N_x$ Epilayers", Presented at 27th North American Molecular Beam Epitaxy (NAMBE) Conference, Colorado, 2010.